Laser–Microwave Synchronisation for Ultrafast Electron Diffraction

Matthew Walbran

SIGILL. UNIVERSITAT. LUDOVIC. MAXIM.

München 2015

Laser–Microwave Synchronisation for Ultrafast Electron Diffraction

Matthew Walbran

Dissertation
an der Physik
der Ludwig–Maximilians–Universität
München

vorgelegt von
Matthew Walbran
aus Auckland, New Zealand

München, den 29.07.2015

Erstgutachter: Prof. Dr. Ferenc Krausz
Zweitgutachter: Prof. Dr. Jom Luiten
Tag der mündlichen Prüfung: 25.09.2015

Zusammenfassung

Ultraschnelle Elektronbeugung ist eine pump–probe Technik, durch die sich Molekulardynamiken mit atomarer Auflösung visualisieren lassen. Allerdings können die schnellsten elektronischen und atomaren Licht-Materie Wechselwirkungen mit dieser Technik noch nicht gemessen werden. Der Grund dafür ist, dass die zeitliche Auflösung durch die praktische Realisierung extrem kurzer Elektronenpulse, bedingt durch Coulomb-Abstoßung und Vakuum-Dispersion aufgrund der Ruhemasse, limitiert ist. Die Raumladung und endliche Energiebandbreite führen beide zu einer zeitlichen Verlängerung der Elektronenpulsdauer. Zwar können solche Pulse mit Mikrowellenfeldern zeitlich komprimiert werden, aber diese Methode ist fundamental durch die möglich zeitliche Synchronisation der Mikrowelle mit den erzeugenden Laserpulsen limitiert.

In dieser Arbeit soll diese Limitierung überwunden werden, um die zeitliche Auflösung von ultraschneller Elektronenbeugung zu verbessern und ultimativ in das Regime jeglicher realistischer Licht-Materie-Wechselwirkung vorzudringen. Zunächst wird ein hochauflösendes mikrowellen-optisches Phasenspektrometer basierend auf optischer Interferometrie entwickelt, welches bei der 800 nm Ti:Sapphir-Wellenlänge arbeitet, die am besten zur Probenanregung geeignet ist. Dieser Phasendetektor bietet eine Auflösung von 3 fs und ist in der Lage, als wesentliches Bestandteil einer Phasenregelschleife zur rauscharmen Synchronisierung eines dielektrischen Resonator-Oszillators mit dem Ti:Sapphir-Laser. Darüberhinaus zeigen wir eine neuartige passive Synchronisierungstechnik durch direkte Extraktion einer Mikrowellenfrequenz aus einer Harmonischen der Laser-Repetitionsrate mittels Photodetektion.

Es werden Rekordwerte im Phasenrauschen über neun Frequenz-Dekaden (mHz–MHz) durch den Einsatz eines optischen Modenfilters gezeigt. Dieser unterdrückt thermisches Rauschen und arbeitet bei niedrigen Pulsenergien, um Amplitude-zu-Phase-Konversion bei der Photodetektion zu reduzieren. In einer Verstärkerkette wird dieses Mikrowellensignal verstärkt, um die zur Elektronenpulskompression nötige Leistung zu erreichen. Durch rigorose Out-of-loop-Charakterisierung der Synchronisation mittels des mikrowellen-optischen Phasendetektors wird eine

Standardabweichung der zeitlichen Stabilität von 4.8 fs gezeigt. Diese überlegene Synchronisation erlaubte die Erzeugung von 12 fs (Standardabweichung) Elektronenpulsen, welche nach unserem Wissen die kürzesten sind.

Zuletzt wird die Stabilität der Laser-Elektronen-Synchronisation über mehrere Stunden gezeigt, welche durch Ausregeln der Langzeitdrifts mittels einer in-situ Messung ermöglicht wird. Dadurch wird gezeigt, dass ultraschnelle Elektronenbeugung durch die Anwendung dieser Techniken für die Beobachtung der schnellsten reversiblen Licht-Materie-Wechselwirkungsdynamiken auf atomaren Skalen geeignet ist.

Abstract

Ultrafast electron diffraction is a pump–probe technique that allows the visualisation of molecular dynamics with atomic scale resolution. However, the fastest electronic and atomic dynamics in light-driven matter transformations are, as yet, unmeasureable with this technique. This is because the temporal resolution in ultrafast electron diffraction is limited by difficulties in producing the shortest electron pulses, caused by the electron charge, via Coulomb repulsion (space charge), and rest mass, via vacuum dispersion of the electron wavefunction. Space charge effects and a finite energy bandwidth both lead to temporal broadening of electron pulses. Methods to compress such pulses in microwave fields have been developed, but these are fundamentally limited by the achievable temporal synchronisation of the employed microwave with the excitation laser pulses.

This work is aimed at breaking this limitation and thereby advancing ultrafast electron diffraction towards the ultimate temporal resolution of any realistic light–matter interaction. Firstly, a high-resolution optical-microwave phase detector based on optical interferometry is designed for operation around the 800-nm wavelength of Ti:sapphire lasers best suited for sample excitation. The phase detector provides a resolution of 3 fs and the capability of functioning as an integral component in a phase-locked loop for synchronising a low-noise dielectric resonator oscillator with the Ti:sapphire laser.

Furthermore, we demonstrate a separate, novel, passive synchronisation technique through direct microwave extraction of a harmonic of the laser repetition rate by photodetection. A record-low residual phase noise over nine frequency decades (mHz–MHz) is achieved through implementation of an optical-mode filter which circumvents thermal noise problems at low pulses energies to simultaneously reduce detrimental amplitude-to-phase noise conversion in the photodetection process. An amplification chain is designed to achieve a microwave power suitable for electron compression while preserving this excellent phase noise. Rigorous out-of-loop characterisation of the synchronisation with the optical-microwave phase detector shows a root-mean-square (rms) timing stability of 4.8 fs. This superior synchronisation has allowed the generation of 12 fs (rms) electron pulses, the shortest to our knowledge.

Lastly, stability of the laser–electron synchronisation over many hours is also demonstrated on a sub-five-femtosecond scale through in-situ measurement and subsequent compensation for the entire range of possible long-term drifts. This shows that incorporating these techniques can allow ultrafast electron diffraction experiments to observe the fastest reversible atomic-scale light–matter interaction dynamics.

Contents

List of Figures

List of abbreviations

DLL	Delay-locked loop
DC	Direct current
DBM	Double balanced mixer
DRO	Dieletric resonator oscillator
FEL	Free-electron laser
FLOM-PD	Fiber-loop optical-microwave phase detector
FWHM	Full width at half maximum
MCP	Micro-channel plate
PLL	Phase-locked loop
PSD	Power spectral density
RIN	Relative intensity noise
rms	Root mean square
SSB	Single-sideband
ToF	Time-of-flight
UED	Ultrafast electron diffraction
VOA	Variable optical attenuator
VCO	Voltage controlled oscillator

Chapter 1.

Atomic and electronic motion on ultrashort timescales

1.1. Ultrafast electron diffraction

Fundamental physical, chemical and biological processes resolve on ultrashort timescales at the sub-molecular level. Gaining access to the evolution of such processes requires techniques with femtosecond and picometer resolutions [1–6]. These techniques are typically pump–probe methods, whereby a process is initiated by an ultrashort optical pulse and subsequently examined (probed) with a second ultrashort pulse at varying, controlled delay times. Reconstructing the structural information obtained from each delay step leads to a visualisation of the dynamics as they play out, similar to time-lapse photography, but on much shorter, atomic-level time scales. One established technique for probing molecular dynamics in space and time is that of ultrafast electron diffraction (UED) [7, 8], which utilises optical pulses for exciting dynamics, and ultrashort electron pulses as the probe. Employing electrons accelerated to keV energies, i.e. picometer de Broglie wavelengths, achieves the subatomic resolution required to obtain direct structural information [6,8]. UED has allowed scientists to study a plethora of ultrafast processes on the molecular scale, including melting and heating processes [9–12], structural phase transformations in condensed matter [13–16] and isolated chemical reactions [17–19].

The concept of a UED experiment is depicted in Fig 1.1. A femtosecond laser is split into two arms; one arm is used for electron generation via the photoelectric effect, while the other arm is used for sample excitation. After being emitted from a photocathode at high voltage, the electrons are accelerated in a DC field up to the energy required for diffraction, typically 30–300 keV [21].

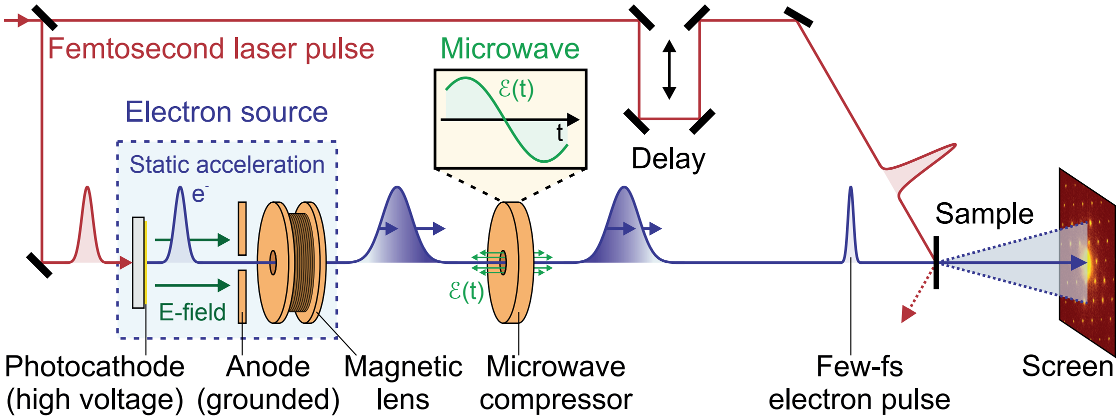

Figure 1.1.: Ultrafast electron diffraction concept, figure from [20]. A laser illuminates a photocathode charged to a high voltage, generating electrons via the photoelectric effect. The electrons are accelerated towards a grounded anode to an energy suitable for diffraction (typically 30–300 keV). The electrons are transversely collimated with a magnetic lens and longitudinally focused with a microwave cavity before being incident on the diffraction target. The sample dynamics is initiated by the laser pulses, with the laser–electron delay controlled by a delay stage inserted into the pump beam arm. The diffracted electrons are collected by a camera.

The initial transverse and longitudinal velocity spread of the electrons upon generation leads to divergence and temporal broadening. Divergence can be compensated for with static fields in magnetic lenses. Temporal broadening can be compensated for with time-dependent fields in microwave cavities [22–28], however this is generally limited by the achievable synchronisation between the driving microwave and the laser, and is often a limiting factor in UED experiments [28–30]. Without precise synchronisation, efforts to compress the electron pulses can in fact have a detrimental effect [25]. This issue is described in detail in chapter 2 and its resolution is the central theme of this thesis (chapters 3–7).

After the transverse and longitudinal compensation elements, the electrons are diffracted from the sample, with the laser–electron delay controlled by a delay stage inserted into the pump beam arm. Finally, the diffracted electrons are collected by a camera, providing time-resolved structural changes of molecular systems. Diffraction setups may be designed with a transmission geometry (as depicted), or reflection geometry. Transmission experiments require sample thicknesses on the order of 10–50 nm to maintain a high enough electron throughput, due to the electron inelastic mean free path [31]. However, reflection geometries require phase matching between the pump pulses and the electron probe in collinear setups [32], which is not required in transmission.

The biggest challenge for achieving the best temporal resolution in a UED experiment is the ability to produce ultrashort electron pulses [33, 34], which is difficult due to the electron rest mass and charge [35]. Ideally, bright pulses are required in order to study any processes, especially irreversible ones [9]. However, Coulomb repulsion in bright electron pulses severely limits the achievable pulse duration through an unavoidable, irreversible expansion of the Liouville phase space [35]. To access the fastest processes in condensed matter systems, a time resolution on the order of 10 fs full width at half maximum (FWHM) or 5 fs root-mean-square (rms) is required. Space charge effects do not allow for this and UED setups with bright electron pulses are currently limited to a resolution of about 100 fs [28–30]. This, and the pump–probe jitter problem mentioned above, currently prevents UED from being applied to many classes of fundamental questions in physics and chemistry.

1.2. Single-electron pulses

Space charge effects can be somewhat mitigated by using relativistic electrons which experience minimal coulomb repulsion [36–38], however this leads to a decrease in the scattering angle, due to the too short de Broglie wavelengths, and difficulties in beam line design. Producing only one electron per laser pulse, on the other hand, completely eliminates space charge effects [39]. With no other electrons, the single electron cannot experience any internal repulsive forces and hence maintains its phase space volume through the entire beam line. While a single-electron duration may be described in terms of its coherence length, this is not a fair representation of the electron pulse duration, as a single-electron diffraction experiment requires the repetition of many pump–probe events, $\sim 10^7$–10^9 [40]. It is more realistic to think in terms of the arrival times of all electrons in an integrated diffraction image, with respect to the exciting laser pulses. The pulse duration can then be defined as the full width at half maximum of the envelope of the statistical distribution of the total electrons integrated over a certain number of single electrons [41], and is so used in the remainder of this thesis, unless specifically stated otherwise.

An additional advantage of moving to the single-electron regime is the possibility for improved transverse coherence. Transverse coherence is a measure of the ability of spatially separated electron wavepackets to interfere with themselves, and hence defines the physical size of the atomic-scale system which can be studied. In typical UED setups with space charge, at electron de Broglie wavelengths in the region 0.02 – 0.07 Å (for 30 – 300 keV electrons), the transverse coherence is on the order of 2–3 nm [41, 42], which allows investigations of many condensed matter systems but does not provide access to biomolecular systems with few-nanometer sizes. With single-electron pulses, exhibiting no Coulomb repulsion, the divergence is reduced and therefore allows the possibility of a higher coherence; a coherence of up to 20 nm for single-electron sources has been demonstrated [43]. Together with the in principle infinitesimally short pulse duration, single-electron pulses therefore offer a valuable perspective for studying ultrafast physical and chemical processes on fundamental length and time scales, provided they can be repeatedly studied.

1.3. Requirements for the laser system

Performing a complete time-resolved ("4D") diffraction experiment with single-electron pulses, while having the potential for ultimate temporal resolution and spatial coherence, sets some important limits on the possible samples to study. To build up a useful diffraction image requires upwards of 10^7 electrons [40] and the dynamics under investigation must therefore be highly reversible. Furthermore, to reduce total acquisition time, the repetition rate of the laser must be as high as possible. Going to higher repetition rates, however, involves depositing more energy in the sample, eventually destroying it, and the time between pump pulses must be long enough to let the sample completely relax from one excitation to the next. Therefore, the ideal laser repetition rate is in the 100 kHz – few MHz range [40].

The properties of the laser pulses incident on the photocathode for electron generation are critical to produce electron pulses with suitable phase-space characteristics for diffraction. Excitation of an electron occurs through photon absorption and may happen at any point during irradiation within the laser pulse width. For a flat metal cathode, surface imperfections result in not only a longitudinal velocity spread, but also a transverse spread [41]. Therefore, the initial energy bandwidth of the electrons should be minimised for both favourable compression characteristics (described in section 2.1) and for maximising transverse coherence [43]. Because the energy transfer in the emission process is indirect [44], the electron energy spread is reduced by minimising the difference between the cathode work function and the photon energy [45]. Also, the uncertainty relation causes a trade off between the laser pulse duration and bandwidth to optimise the electron properties [41].

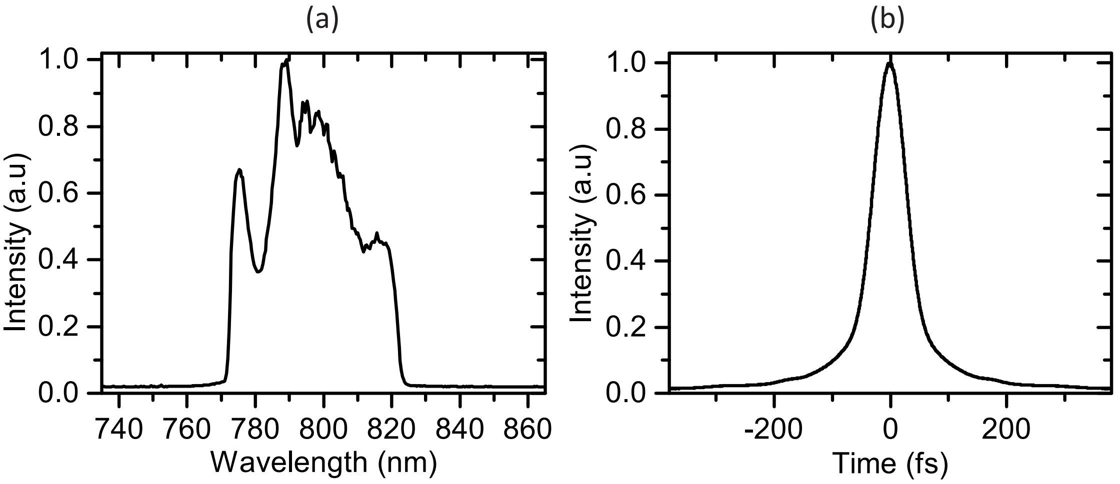

Figure 1.2.: Spectral and temporal characteristics of the Ti:Sapphire laser used in this work, from [20]. (a) The spectrum spans approximately 50 nm from 770 nm to 820 nm and yields a compressed pulse duration (b) of 50 fs.

Here we use a 50-fs Fourier limited Ti:sapphire oscillator, with a spectrum spanning from 770 to 820 nm, as shown in Fig 1.2. Generation of electrons from a gold photocathode, with a work function of ~4.2 eV [46], is achieved by frequency tripling the 800 nm light to 266 nm, corresponding to a photon energy of ~4.66 eV. This provides for the generation of electrons with an initial energy spread of ~0.2 eV [41]. The Ti:sapphire oscillator has a 5 MHz repetition rate to provide for reduced acquisition times. In the case that a diffraction sample cannot sustain laser pump pulses at 5 MHz, the repetition rate is controllable with a pulse picker, which allows for dividing the repetition rate by an integer. When implementing electron beam optics such as the microwave cavity (see in section 2.1), however, it is advantageous to use the full repetition rate for the best synchronisation (see section 5.1).

Achieving the optimum temporal resolution for UED experiments is the central theme of this thesis, to advance the resolution to a point allowing the direct probing of the fastest realistically possible structural dynamics in condensed matter and molecules. This thesis is structured as follows: Chapter 2 discusses single-electron compression in microwave fields, leading to the key issue of laser–microwave synchronisation. This is followed by a review of existing synchronisation techniques, along with their intended (or implemented) applications, introducing the current state of the art. Chapter 3 presents a fiber-loop optical–microwave phase detector [47], based on optical interferometry, and designed for applications with Ti:sapphire laser systems. The demonstrated parameters of the device allow for a phase detection sensitivity of less than 3 fs on a few-minute timescale up to the Nyquist frequency. Chapter 4 presents a first implementation of the phase detector via a phase-locked loop for synchronising a dielectric resonator oscillator with the Ti:sapphire oscillator. This implementation results in a 50-fs synchronisation stability, measured out-of-loop by a direct measurement of the laser–electron delay with a time-of-flight spectrometer [48]. Chapter 5 introduces an alternative synchronisation scheme without any active feedback. This scheme is accurately characterised with the fiber-loop phase detector and shows a short term stability (2 mHz – 2.5 MHz) within 5 fs (rms). This results in the synchronisation no longer being a dominant factor with regards to the achievable electron pulse duration, and hence UED temporal resolution. Chapter 6 discusses the requirements for achieving a long term stable synchronisation with the scheme described in chapter 5 and shows that, through compensation of the drift arising via laser–electron streaking [49], stability over the many hours required to acquire a complete 4D single-electron diffraction experiment is also achievable on a 5-fs (rms) level. Chapter 7 provides an outlook towards realisation of this novel synchronisation scheme in our UED beam line and the possibilities for investigation of fundamental dynamics in space and time.

Chapter 2.

Temporal resolution limitations in single-electron UED

In chapter 1, the concept of single-electron UED was introduced as a means of circumventing the space charge effects in multi-electron pulses which leads to broadening of electron pulses after propagation over any significant distance, thus limiting the achievable temporal resolution. While single-electron pulses completely eliminates the space charge effect, there remain other factors which need to be accounted for if resolution on a few-femtosecond scale is to be achieved [35]. There are two essential effects. First, the electron pulse duration upon generation, as discussed in section 1.3, is limited by the laser pulse duration. Second, due to the finite bandwidth of the electrons and the dispersive nature of electrons in vacuum, electrons of higher energy travel faster than those of lower energy. After propagation over a certain distance, this ultimately leads to a temporal broadening of the pulse. Even with single-electron pulses, we require a means of recompression of the pulse, such as the microwave cavity in Fig 1.1, ideally to durations shorter than their initial duration at photoemission.

2.1. Electron pulse compression in microwave fields

Compression of single-electron wave packets in the time domain relies on manipulation of the electron phase space. After propagation-induced dispersion, the electron phase space tends toward a linear distribution. By spatial separation of the electrons based on energy (or velocity) through the use of static electric fields, and propagating the higher energy electrons over a longer distance before recombining the pulse, it is possible to invert the phase space, after which the pulse self compresses.

This has, for example, been implemented through chicanes [36] and electrostatic reflectrons [50, 51]. In the absence of space charge, the initial energy bandwidth of the electron pulses is generally maintained throughout a beam line containing any static electric and magnetic fields. This therefore does not allow for the possibility of compression below the initial pulse duration due to the conservation of the electron phase space, as described by Louville's theorem.

However, shorter pulse durations can be achieved by propagation of the pulse through a time-dependent electric field. This can not only invert the linear phase space, but also stretch it along the energy axis, providing the means for compression beyond any initial limitations.

Methods for such compression have been conceived theoretically using microwave cavities [22, 23], or ponderomotive forces [52–54]. In [54], temporal compression is combined with transverse compression which has the potential to avoid temporal distortions introduced by magnetic lenses [55]. The concept of such energy modulation, depicted in Fig 2.1, is described as follows. When electrons are generated from a laser via the photoelectric effect, they have a pulse duration and energy spread determined by the laser pulse and spectral widths (see section 1.2), respectively, and an uncorrelated phase space distribution (point (1) in Fig 2.1). Dispersion from the initial pulse duration τ_{initial} occurs during propagation as a result of vacuum dispersion which leads to a broadened pulse duration τ_{disp} at (2). Next, propagation in a longitudinal time-dependent electric field with the field phase nulled at the arrival of the center of the pulse modulates the electron energy such that the leading electrons are decelerated and the trailing electrons are accelerated, inverting the phase space, as depicted by (3). Essential to the concept of compression is the overcompensation of the phase space affected through the time-dependent field, producing new energy components. Note that the phase space volume is conserved in the absence of space charge and remains approximately linear as long as the dispersed pulse duration τ_{disp} is much shorter than the period of the microwave $T_{\text{microwave}}$, or $\tau_{\text{disp}}/T_{\text{microwave}} \ll 1$. Over the length of time during which the electrons experience this energy modulation, the pulse duration remains approximately τ_{disp}, but the energy bandwidth increases and the chirp is reversed. Further propagation leads to self compression as the trailing, higher energy electrons catch up to the leading, lower energy electrons. Finally, the pulse becomes maximally compressed at (4), the location of the diffraction sample.

The achievable electron pulse duration τ_{final} is approximately given by [25]

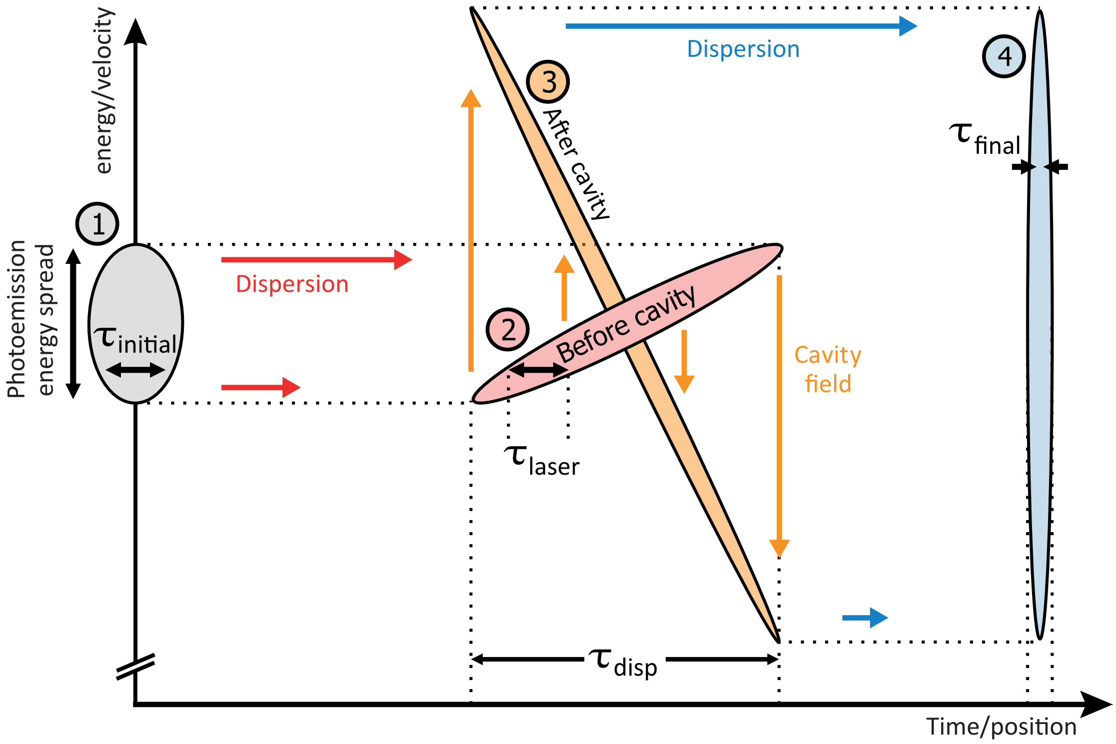

Figure 2.1.: Electron compression with microwave fields, figure taken from [25]. (1) The electron pulse is generated with an initial energy spread and temporal spread τ_{initial} determined by the laser. The pulse has dispersed on arrival at the microwave cavity (2) to a duration of τ_{disp} and exhibits a linear chirp, with the higher energy electrons leading the lower energy electrons. The microwave phase is arranged in such a way that the leading, higher energy electrons are decelerated and the lagging, lower energy electrons are accelerated, inverting the chirp and increasing the energy bandwidth (3). During propagation after the phase space inversion, the electron pulse self compresses until reaching (4) where the faster trailing electrons catch the slower leading electrons and the pulse is maximally compressed. The pulse compresses maximally at a single point in space (4), at a duration significantly shorter than upon generation

$$\tau_{\text{final}} = \tau_{\text{initial}} \frac{\triangle v_{\text{initial}}}{\triangle v_{\text{final}}} \approx \tau_{\text{initial}} \frac{\triangle E_{\text{initial}}}{\triangle E_{\text{final}}}, \tag{2.1}$$

where $\triangle v_{\text{initial}}$, $\triangle v_{\text{final}}$, $\triangle E_{\text{initial}}$ and $\triangle E_{\text{final}}$ are the initial velocity spread, final velocity spread, initial energy spread and final energy spread, respectively. This shows that by having $\triangle E_{\text{final}} > \triangle E_{\text{initial}}$, compression of electron pulses to shorter than the initial duration is possible. Note that this approximation holds only for small changes in the electron energy with respect to its central energy.

As noted above, this minimum pulse duration is localised in space and therefore the propagation distance required to reach the temporal focus is of importance. The location of the temporal focus f after propagation through the time dependent field is given by [23]

$$f = \sqrt{\frac{8E_0^3}{m_e}} \frac{\tau_{\text{disp}}}{\triangle E_{\text{final}}} = \sqrt{\frac{8E_0^3}{m_e}} \frac{1}{g_{\text{E}}}, \tag{2.2}$$

where E_0 is the central energy of the electron pulse, m_e the electron mass and $g_{\text{E}} = \triangle E_{\text{final}}/\tau_{\text{disp}}$ is the time dependent energy gain coefficient describing the energy transferred from the field to the electrons, characterising the compression strength, and is proportional to the frequency and amplitude of the employed field. The temporal focus, which should be tuned to coincide with the diffraction sample position, can then be controlled by the electric field characteristics of the microwave. In order to reduce power requirements, it is helpful to use higher driving frequencies [25].

In a microwave cavity, the resonance frequency is governed by the physical dimensions of the cavity and must be limited such that the period remains considerably larger than the electron pulse duration inside the cavity ($T_{\text{microwave}} \gg \tau_{\text{disp}}$) to maintain a linear manipulation of the electron phase space. As long as this caveat is adhered to, a high frequency also serves to relax the synchronisation requirements to achieve the same time-domain jitter (defined in section 2.2 below) as a lower-frequency source.

In this work we employed a microwave cavity operating in the TM_{010} mode, designed for operation around 6.2 GHz [25]. The resonance was tuneable through thermal expansion at a rate of approximately -100 kHz/K for matching to the driving microwave source. At 6.2 GHz, the period is $T_{\text{microwave}} \approx 160\,\text{ps}$, much longer than the electron pulse duration upon arrival at the cavity of $\tau_{\text{disp}} = 300\,\text{fs}$ [49], ensuring a linear transformation of the electron phase space. With this frequency, a realistic temporal focus of ~20 cm is easily achievable with a few hundred milliwatts of microwave power, at a central electron energy of $E_0 = 25\,\text{keV}$.

The actual achievable compressed electron pulse duration is limited by Eq 2.1 and two other factors in the experiment. One is imperfections in the electron beam line leading to a slightly curved phase space, discussed further in section 5.4. Second is the quality of the synchronisation between the microwave driving the cavity, and the femtosecond laser pulses providing excitation of the diffraction sample. Maintaining precise synchronisation between the phase of the microwave inside the cavity with respect to the pump laser is critical to achieving a high temporal resolution in pump probe experiments.

2.2. Phase noise and jitter

In section 2.1, jitter in terms of the quality of a synchronisation scheme was introduced. This quantifies the timing error of a particular signal with respect to a reference, in this case the microwave with respect to the laser pulse train, and is a commonly used term in synchronisation schemes. The jitter of a particular signal is given for a particular frequency within a specified bandwidth, typically as an rms value, as detailed in the following.

An ideal sinusoidal signal of amplitude A_0 and frequency f_0 has the form

$$y\left(t\right) = A_0 \sin\left(2\pi f_0 t\right), \tag{2.3}$$

however in reality, all waveforms have associated noise which can be in the form of an amplitude noise or a phase noise. Assuming random phase variations $\phi\left(t\right)$, and random amplitude fluctuations $\varepsilon\left(t\right)$, Eq 2.3 becomes

$$y\left(t\right) \;=\; \left[A_0 + \varepsilon\left(t\right)\right] \sin\left(2\pi f_0 t + \phi\left(t\right)\right). \tag{2.4}$$

Amplitude noise introduces fluctuations in the power of the waveform while phase noise is a measure of the deviations in the instantaneous frequency from the carrier frequency. Although it is possible for power fluctuations to play a part in contributing to timing error, as seen in sections 3.4 and 5.1 below, this typically only occurs through transformation into a phase noise. Therefore, in the following, the term $\varepsilon\left(t\right)$ is ignored, letting Eq 2.4 be rewritten as

$$y\left(t\right) = A_0 \sin\left(2\pi f_0 \left\{t + \frac{\phi\left(t\right)}{2\pi f_0}\right\}\right). \tag{2.5}$$

The term $\frac{\phi(t)}{2\pi f_0}$ in Eq 2.5 is essentially the time-domain variations of the signal due to phase fluctuations, defined as jitter. As this is a relation between two random quantities, it is not particularly useful, however it shows that timing jitter is related to phase fluctuations by the factor $1/2\pi f_0$. These random phase fluctuations are easier understood as a collection of noise components of varying strength in the frequency domain. The phase-noise power spectral density (PSD) may be stated as either a two sided PSD $S_\phi(f)$, or a one sided PSD $\mathcal{L}_\phi(f)$, and are related by [56]

$$\mathcal{L}_\phi(f) = \frac{1}{2} S_\phi(f) \tag{2.6}$$

with units of rad^2/Hz. Note that most instruments for measuring phase noise specify the one sided PSD $\mathcal{L}_{\phi,dB}(f)$ expressed in decibels relative to the carrier (dBc/Hz), where

$$\mathcal{L}_{\phi,dB}(f) = 10 \log\left[\mathcal{L}_\phi(f)\right]. \tag{2.7}$$

Similar to above, the phase-noise PSD is related to the jitter density, in units of s^2/Hz, by

$$J_{PSD} = \frac{1}{(2\pi f_0)^2} S_\phi(f). \tag{2.8}$$

The rms jitter J_{rms} within a certain bandwidth $\triangle f$ can then be calculated as the square root of the integral of the jitter density [57]

$$\begin{aligned} J_{rms} &= \sqrt{\int_{\triangle f} J_{PSD} df} \\ &= \frac{1}{2\pi f_0} \sqrt{\int_{\triangle f} S_\phi(f) df}. \end{aligned} \tag{2.9}$$

In the following chapters, unless explicitly stated as otherwise, phase noise is specified as the one sided PSD $\mathcal{L}_{\phi,dB}(f)$ and jitter values are specified as the rms value J_{rms}, and specified to a frequency bandwidth. For a sine wave, the relation between peak-to-peak fluctuations σ_{pp} and rms fluctuations σ_{rms} is given by $\sigma_{pp} = 2\sqrt{2}\sigma_{rms}$. Note that phase noise can be defined in two different ways, as either absolute or residual phase noise. Residual phase noise is the noise added by a particular device to a system, while absolute phase noise is the total noise at the output of a system, including the noise of the reference or generating oscillator. For microwave compression, where a microwave source is synchronised to a laser oscillator, it is the residual phase noise which contributes to the jitter which is relevant in the experiment.

2.3. Laser–microwave synchronisation concepts

In the following, different concepts for laser–microwave synchronisation techniques are reviewed, and the key aspects of such synchronisation schemes are described. A common technique for synchronisation between two sources involves the use of a phase-locked loop (PLL), a method for the precise synchronisation of a voltage-controlled oscillator (VCO) to a reference signal. Fig 2.2 shows the block diagram of a PLL. The principle works as follows: A reference signal of phase φ_r is compared with the output phase from a VCO φ_o in a phase detector (PD). The output from the phase detector is proportional, by the sensitivity factor K_d of the phase detector, to the phase difference between the two signals $(\varphi_r - \varphi_o)$. This is referred to as the *error signal* and is passed to a loop filter (LF) with a transfer function $F(s)$, generally a low-pass filter, which determines the signal to be applied as a control voltage to the VCO. The VCO has a response K_o/s which effects the resonance frequency as a function of the control voltage. Note that the transfer functions $F(s)$ and K_d/s are the Laplace transforms of the time domain transfer functions. The frequency of the VCO is adjusted to maintain the error signal, and hence the phase difference between the VCO output and the reference signal, at

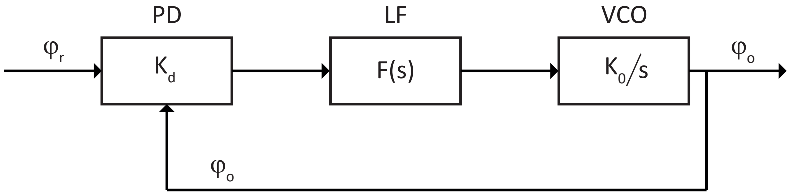

Figure 2.2.: Phase-locked loop block diagram. The phase or frequency difference between the output from a voltage-controlled oscillator (VCO) and a reference signal is measured with a phase detector (PD). The output of the phase detector, the error signal, is proportional to the measured phase difference $(\varphi_r - \varphi_o)$ and is passed to a loop filter which filters the input for application to the VCO. The control voltage dependent resonance frequency of the VCO then approaches the reference frequency until a lock is found by maintaining the error signal at zero.

zero. The output phase of the VCO φ_o can be described in terms of the phase-locked loop components by

$$\begin{aligned}\varphi_o &= (\varphi_r - \varphi_o)\, K_d F(s)\, \frac{K_o}{s} \\ &= (\varphi_r - \varphi_o)\, \frac{K F(s)}{s}, \qquad (2.10)\end{aligned}$$

where $K = K_d K_o$ is defined as the forward loop gain. Rearranging Eq 2.10 for the transfer function $H(s) \equiv \varphi_o/\varphi_r$ gives

$$H(s) = \frac{K F(s)}{s + K F(s)}. \qquad (2.11)$$

When schemes involving a PLL are in a locked state, the error signal no longer provides an accurate representation of the synchronisation quality. In order to make a proper out-of-loop characterisation, a second phase detector not being used for feedback is required.

Good quality synchronisation between microwave sources and lasers has been important in accelerator facilities [58] and UED likewise, and is also a critical aspect for free-electron laser (FEL) systems [59,60]. 20-fs synchronisation, for both long-term and short-term (0.05 Hz to 100 kHz) has been demonstrated with a PLL between a 3 GHz microwave oscillator and a 75 MHz repetition rate Ti:sapphire laser [61]. This was achieved by phase detection between the 5th harmonic of the laser repetition rate at 375 MHz and the output of a 3 GHz oscillator, frequency divided by eight, in a double balanced mixer (DBM). The synchronisation was limited by the achievable bandwidth of the loop filter with most jitter arising at high frequencies. This synchronisation method has been employed for driving a microwave cavity in UED systems [26, 28, 29]. The Instrument Response Function (IRF), that is, a convolution between the synchronisation jitter, laser pulse, and electron pulse duration, has been measured for these systems with ponderomotive scattering at 150–200 fs (rms) for bright electron pulses with 0.1–0.6 pC [26,28]. The synchronisation technique was claimed to be the dominant contributor to the IRF measurement in these cases. A separate characterisation method based on direct measurement of the microwave phase inside the cavity by electro-optic sampling has been demonstrated in [29]. This technique had a resolution of 30 fs (rms) and demonstrated an rms jitter of 100 fs. Measurements of the synchronisation with a streak camera in [30] has demonstrated an effective 30 fs rms jitter after post correction of the data.

There is also currently a great interest in the generation of ultra-low-noise microwave signals derived from femtosecond mode-locked lasers for applications such as in radar systems for higher precision detection [62, 63]. Division from optical to microwave frequencies by photodetection of the frequency comb of a mode-locked laser locked to an ultra-stable continuous-wave laser [64] produces a microwave signal with the precision of the optical frequency standard. Recently, the generation of a 10 GHz microwave signal with an absolute timing jitter of less than 1 fs from a 1 GHz repetition rate Ti:sapphire oscillator [65] and an 11.55 GHz microwave with a timing stability of less than 100 as from a 250 MHz oscillator [66] have been demonstrated. The limiting factors to these systems is excess noise introduced in the photodetection process [67], discussed in detail in chapter 5.

Methods for the synchronisation of optical and microwave sources over long distances is another field of strong interest [68–70]. One such method is based on imparting the relevant synchronisation information in the optical domain, rather than the electronic domain, through balanced intensity detection [71] and balanced phase detection [47]. The signal derived from such detection serves as a phase detector (Fig 2.2) for the purpose of locking to a VCO in a PLL. This avoids the need for compensation of noise added in the photodetection process. The extreme sensitivity of optical interferometry produces superior resolution of the laser–microwave delay; down to attosecond precision between mode-locked lasers and VCOs has been demonstrated with low-noise fiber oscillators at telecommunication wavelengths [72–74] over distances spanning from 2.3 km up to 120 km.

In this work, a few GHz microwave source (as per section 2.1) for driving the microwave cavity is synchronised to our 5 MHz Ti:sapphire laser system in order to yield the minimum possible electron pulse duration for application in ultrafast electron diffraction experiments. Towards this end, a fiber-loop optical–microwave phase detector (FLOM-PD) optimised for operation around the Ti:sapphire spectral range is developed for providing feedback to a dielectric resonator oscillator (DRO) locked to a harmonic of the repetition rate of the laser repetition rate. An alternative approach for synchronisation, based on direct extraction of a microwave signal through filtering and amplification of a photodetected current pulse train from the laser is demonstrated (see chapter 5). In this case, the FLOM-PD provides the capability for out-of-loop characterisation of the performance. A jitter of less than 5 fs and a long term stability on the same scale is achieved (see chapter 6).

2.4. Fundamental noise limitations

Whatever the synchronisation technique is, there are fundamental noise limitations which cannot be avoided. There are two noise aspects which can limit the performance of microwave signals. These are shot noise [75] and thermal noise [76, 77]. Shot noise arises from fluctuations in the level of an optical or electrical signal due to the discrete nature of photons and electrons, and can be modelled as a Poisson process. For an average number particles N, the standard deviation is $\sqrt{N}$ and the signal-to-noise ratio (SNR) is then

$$SNR = \frac{N}{\sqrt{N}} = \sqrt{N}, \tag{2.12}$$

hence the larger the signal, the larger the absolute noise, but the better the SNR. The PSD of the shot noise in a photodetected signal can be given in terms of the average current I_{avg} [78]

$$S_{\mathrm{shot}}\left(\omega\right) = 2eI_{\mathrm{avg}}, \tag{2.13}$$

where e is the electronic charge. This PSD is a white noise and contributes a constant background to the phase noise of the signal which is difficult to suppress and can be a limiting factor in the achievable phase noise at significantly large photocurrents [79].

Thermal noise on the other hand arises as a result of the thermal agitation of charge carriers in a conductor at non-zero temperature. A resistive element produces a thermal noise voltage within a bandwidth $\triangle f$ of

$$\upsilon = \sqrt{k_B T R \triangle f}, \tag{2.14}$$

where k_B is Boltzmann's constant and R and T the resistance and temperature (in Kelvin) of the element, respectively. This is also a white noise, with a PSD of

$$S_{\mathrm{thermal}} = k_B T. \tag{2.15}$$

At room temperature, this amounts to a PSD of $S_{\mathrm{thermal}} = -174\,\mathrm{dBm/Hz}$. While this is a very small quantity, it is important to note that the noise power is independent of the applied power, and the SNR scales linearly with the signal power. Therefore, while shot noise may dominate the phase noise of a signal at higher power (or current), at very low signal powers the thermal noise will dominate the phase noise.

Chapter 3.

A few-femtosecond laser–microwave phase detector at 800 nm

As seen in section 2.3, locking a microwave source to a laser pulse train on a few femtosecond scale generally requires a high-precision phase detector. The period of the 6.2 GHz microwave frequency used for electron compression has a period of approximately 160 ps. In order to achieve a synchronisation on the order of a femtosecond therefore requires a precision to within 1×10^{-5} of the microwave period. In the following, a fiber-loop optical–microwave phase detector (FLOM-PD), previously demonstrated in the telecommunications band with Erbium-based fiber lasers at 1530–1550 nm [74,80,81], is adapted for operation around the 800 nm spectral range for use with Ti:sapphire systems. This provides the capability for laser–microwave synchronisation with a PLL towards electron compression down to a few-femtosecond duration. Alternatively, it allows characterisation of other, independent synchronisation schemes with few-femtosecond resolution.

3.1. The fiber-loop optical–microwave phase detector

The FLOM-PD, introduced above in section 2.3, is a phase detector which achieves superior resolution by imparting the relative laser–microwave timing information in the optical domain [80]. By measuring the synchronisation in the optical domain via interference, effects such as amplitude-to-phase conversion arising in photodiodes can be avoided [82–84]. The concept of the FLOM-PD is shown in Fig 3.1. An optical pulse train (in red), with repetition rate f_{rep}, is coupled into polarisation-

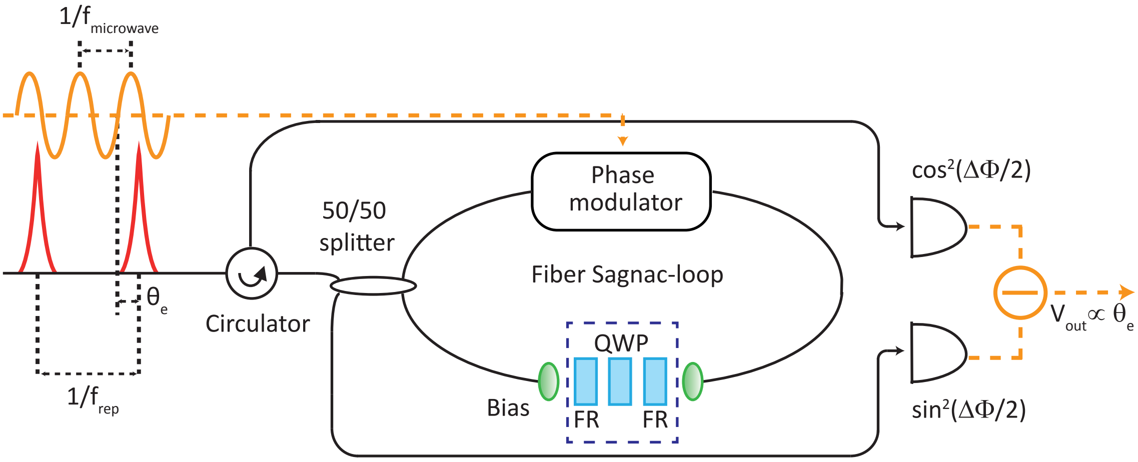

Figure 3.1.: Schematic of the FLOM-PD. A laser pulse train (red) is fiber coupled and split via a 50/50 coupler into a Sagnac loop. A phase modulator applies a phase shift, in proportion to the laser–microwave phase difference θ_e, to one of the pulse trains. After propagation through the loop, the pulse trains interfere, and the outputs from each port of the 50/50 coupler are detected with signal strength proportional to $\sin^2(\triangle\phi/2)$ and $\cos^2(\triangle\phi/2)$ with $\triangle\phi$ the phase difference between the counter-propagating pulses. Balanced detection of the two signals results in a voltage proportional to the phase error θ_e.

maintaining fiber and propagates through a circulator. The pulse train is then split via a 50/50 coupler and the two resulting pulse trains traverse a Sagnac fiber loop in opposite directions and interfere upon arrival back at the coupler. The intensities leaving each of the two coupler ports, assuming a perfect 50/50 splitting ratio in the coupler, are governed by $P_1 = P_{in}(1-L)\cos^2(\triangle\phi/2)$ and $P_2 = P_{in}(1-L)\sin^2(\triangle\phi/2)$, where P_{in} and L are the input optical power into the loop and the total loss of the loop, respectively, and $\triangle\phi$ the relative phase difference upon interference in the coupler of the two pulses [85]. A microwave (in orange) of frequency $f_{\mathrm{microwave}} = nf_{\mathrm{rep}}$, where n is a multiple of the pulse train repetition rate, co-propagates with the clockwise optical pulses in a travelling-wave phase modulator, influencing the optical interference as a function of the instantaneous microwave field strength. This results in either a retardation or advancement of one of the pulse trains. The phase difference between counter-propagating pulses θ_e is encoded in the relative phase difference $\triangle\phi$, and is measured with a balanced detector, providing the change in intensities between the output ports of the coupler. A bias unit provides a phase shift between the clockwise and the

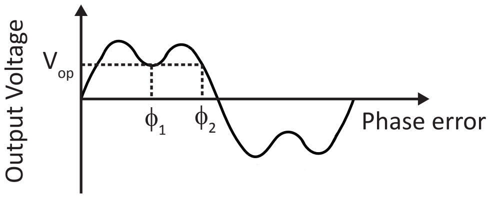

Figure 3.2.: Over-modulation of the FLOM-PD. Increasing the microwave drive voltage such that $V_0 > V_\pi$ results in a distorted output voltage as a function of the phase delay. This results in possible ambiguities such that operation at a particular point V_{op} could mean a relative laser–microwave phase at two different points ϕ_1 and ϕ_2, allowing the possibility of a loop not finding a lock.

counter-clockwise pulses to maximise the detection sensitivity while minimising the amplitude-to-phase conversion.

Realisation of a FLOM-PD for the 800 nm wavelength of Ti:sapphire lasers requires nonstandard components, or in cases where this is not available, standard components not ideal for the required spectral range of ~770–830 nm, which were characterised before implementation. These aspects were considered and are discussed in the following.

3.2. Phase modulation at microwave frequencies

The phase modulator is a lithium niobate based, 10 Gb/s, broadband traveling-wave Mach-Zehnder interferometric modulator (PM-0K5-10-PFA-PFA-800, EO Space) centered at 800 nm. The unidirectional nature of the modulator is achieved as the applied light copropagates with the applied microwave in one direction, building up over the entire medium. The other optical path in the Sagnac loop counter-propagates and the total modulation averages to zero. The modulation depth of the unit is described by

$$\Phi_0 = \frac{\pi}{V_\pi} V_0, \tag{3.1}$$

where V_π is the voltage required to induce an optical π phase shift and V_0 the peak value of the driving microwave voltage. As increasing V_0 results in a linear increase in the sensitivity (as seen below in Eq 3.11), it is desirable to apply the maximum possible microwave strength. However, when $V_0 > V_\pi$, higher-order modulations occur, as depicted in Fig 3.2. This will result in ambiguities in the relative laser–

microwave phase, where a particular operation point V_{op} could be either ϕ_1 or ϕ_2. This may lead to the inability of a loop to find a lock. Using an incorrect sensitivity, defined by the slope of the output voltage with respect to phase (see section 3.3), can also lead to incorrectly interpreted synchronisation measurements. In order to circumvent any ambiguities, the maximum applied voltage was always kept below $V_\pi \approx 2.3\,\mathrm{V}$. As the microwave is more commonly described in terms of the applied rms power $P_{0,rms}$, for a $50\,\Omega$ system, where $P_{0,rms} = V_{0,rms}^2/R$, Eq 3.1 can be rewritten and is more useful in the form

$$\begin{aligned}\Phi_0 &= \frac{\pi}{V_\pi}\sqrt{2}\sqrt{50P_{0,rms}} \\ &= \frac{\pi}{V_\pi}10\sqrt{P_{0,rms}}. \qquad (3.2)\end{aligned}$$

In cases where there was an excess of available microwave power, the input microwave power was limited to $P_{0,rms} = 16\,\mathrm{dBm}$ (~40 mW), resulting in a modulation depth of 0.87π (see Eq 3.2).

3.3. Balanced detection

After propagating through the Sagnac loop, the optical intensities at the two output ports as a result of interference are given by

$$P_1 = P_{in}\left(1 - L\right)\cos^2\left(\frac{\triangle\phi}{2}\right) \qquad (3.3)$$

and

$$P_2 = P_{in}\left(1 - L\right)\sin^2\left(\frac{\triangle\phi}{2}\right), \qquad (3.4)$$

where P_{in} and $\triangle\phi$ are the input optical power into the loop and the relative phase difference upon arrival at the coupler of the two pulses, respectively, and L is the total loss in the Sagnac loop. The phase difference arising as a result of microwave modulation with a frequency $f_{\mathrm{microwave}}$ is given by

$$\triangle\phi\left(t\right) = \Phi_0\sin\left(2\pi f_{\mathrm{microwave}}t + \theta_e\right), \qquad (3.5)$$

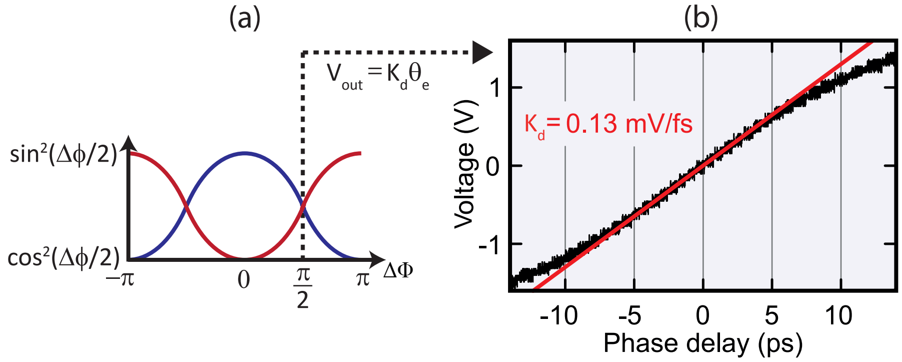

Figure 3.3.: FLOM-PD biasing and sensitivity. (a) The detected signal at the two output ports as a function of the phase difference between counter-propagating pulses. With a phase bias of $\pi/2$ the outputs are equal which results in a balanced signal of maximum sensitivity K_d linear with the phase error θ_e. (b) An example measurement of the sensitivity K_d calibrated by applying a microwave signal of the same input power as used for experiments at a slightly offset frequency from $f_{\text{microwave}}$, and measuring the output on an oscilloscope. The sensitivity is then the slope about the microwave zero-crossing phase. For small phase deviations of ± 5 ps, the balanced voltage is linear and yields a sensitivity of $K_d = 0.13\,\text{mV/fs}$.

where Φ_0 is the modulation depth of the phase modulator, and θ_e the phase error between the driving microwave and the optical pulse train. When the frequency $f_{\text{microwave}}$ applied to the phase modulator is an exact multiple of the repetition rate f_{rep}, by substituting Eq 3.5 into Eqs 3.3 and 3.4 gives a generated average current at the two ports of the balanced detector of [71]

$$\langle I_1 \rangle = RP_{avg} \sin^2\left(\frac{\Phi_0 \sin\theta_e + \pi/2}{2}\right) \tag{3.6}$$

$$\langle I_2 \rangle = RP_{avg} \cos^2\left(\frac{\Phi_0 \sin\theta_e + \pi/2}{2}\right), \tag{3.7}$$

where R is the responsivity of the photodiode in units of A/W, and $P_{avg} = P_{in}(1-L)$ is the average optical power after accounting for all losses in the loop. Note that in the above equations we assume a $\pi/2$ bias provided by the bias unit to achieve the maximum sensitivity, as shown in Fig 3.3a. The output voltage from the balanced detector is given by

$$\langle V_{bal} \rangle \quad = \quad G\left\{\langle I_2 \rangle - \langle I_1 \rangle\right\}, \tag{3.8}$$

where G is the transimpedance gain of the balanced photodetector. From Eqs 3.6 and 3.7, Eq 3.8 yields

$$\begin{aligned}\langle V_{bal}\rangle &= G\left\{RP_{avg}\cos\left(\Phi_0\sin\theta_e+\pi/2\right)\right\}\\ &= GRP_{avg}\sin\left(\Phi_0\sin\theta_e\right).\end{aligned} \tag{3.9}$$

For phase error deviations $\theta_e \ll 1$ the small-angle approximation $\sin\theta_e \approx \theta_e$ is valid and Eq 3.9 reduces to

$$\langle V_{bal}\rangle \approx GRP_{avg}\Phi_0\theta_e. \tag{3.10}$$

This yields a detection sensitivity K_d (as per section 2.3), in units of V/rad, of

$$K_d = GRP_{avg}\Phi_0. \tag{3.11}$$

In the experiment, the sensitivity is calibrated by applying an unlocked microwave source, of equal power to that being used for synchronisation, with a frequency offset $\Delta f \approx 100\,\text{kHz}$ from $f_{\text{microwave}}$. Measured on an oscilloscope, the error signal then traces the output voltage as a function of the phase error, an example of which is shown in Fig 3.3b. The x-axis is achieved by adjusting the measured time delay by the factor $\Delta f/f_{\text{microwave}}$. Note that a time delay is related to a phase shift (in radians) via the factor $2\pi f_{\text{microwave}}$. For a microwave power of 16 dBm, and an input optical power of 28 mW, this results in a sensitivity of $K_d = 0.13\,\text{mV/fs}$, or 3.25 V/rad. That is, assuming that 0.1 mV can be measured reliably, this corresponds to a precision of approximately 1 fs.

3.4. Biasing

In the absence of any microwave modulation the relative phase difference between counter-propagating pulses at interference $\triangle\phi = 0$ is zero. Thus, all power exits through the circulator, as $\cos^2 0 = 1$ and $\sin^2 0 = 0$, to be detected at the upper diode in Fig 3.1. For the derivation of the sensitivity K_d, an external phase shift of $\pi/2$ was assumed as this maximises the slope of the detected signal, and hence the sensitivity. The phase difference arising as a result of microwave modulation,

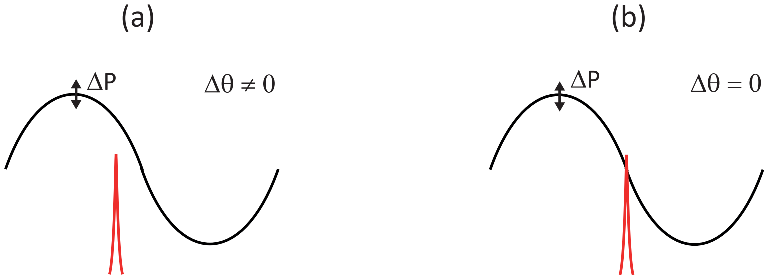

Figure 3.4.: FLOM-PD microwave amplitude-to-phase conversion susceptibility for two different microwave phase offsets. (a) The nominal phase $\Delta\theta \neq 0$ results in a DC modulation proportional to $\sqrt{P}\sin(\Delta\theta)$. Fluctuations in the microwave power ΔP result in fluctuations in the DC phase modulation and are incorrectly interpreted as fluctuations in the error signal θ_e. (b) The nominal phase is nulled with respect to the pulse train. Here amplitude-to-phase fluctuations are avoided as $\sin(\Delta\theta) = 0$.

assuming $f_{\mathrm{microwave}} = nf_{\mathrm{rep}}$, can be rewritten as

$$\Delta\phi_{\mathrm{mod}}(t) = \Phi_0 \sin[\theta_e(t) + \Delta\theta], \tag{3.12}$$

where $\Delta\theta$ is the nominal phase offset of the microwave. Assuming the modulation depth Φ_0 is large enough (as defined by Eq 3.2), a $\pi/2$ phase difference can be achieved when $\Delta\phi = \Delta\phi_{\mathrm{mod}} = \Phi_0 \sin[\theta_e(t) + \Delta\theta]$ for some nonzero $\Delta\theta$. However this has two detrimental consequences. Firstly, with a nonzero $\Delta\theta$ the small angle approximation made in Eq 3.10 is no longer valid and the sensitivity K_d suffers as a result. This increases both the shot and thermal noise, as discussed below in section 3.5. Secondly, and more important, is the effect of microwave AM-to-PM, shown in Fig 3.4. A nonzero phase offset $\Delta\theta \neq 0$, as in Fig 3.4a, results in a DC modulation proportional to $\sqrt{P}\sin(\Delta\theta)$. Fluctuations in the microwave power ΔP will result in fluctuations in the DC phase modulation, and hence the output of the balanced detector, which are then incorrectly interpreted as fluctuations in the error signal θ_e. In the case where the nominal phase is nulled with respect to the pulse train (Fig 3.4b), amplitude-to-phase fluctuations are avoided as $\sin(\Delta\theta) = 0$. This implies that to reduce noise in the system, we require the $\pi/2$ phase shift to be applied external of the phase modulator. This is achieved with the use of an optical bias unit within the Sagnac loop. It consists of a quarter wave plate inserted between two Faraday rotators with 45° rotation, oriented in opposite directions. Between the two Faraday rotators, the two counter-propagating pulses will have polarisation 90° with respect to each other. Aligning the slow axis of the quarter

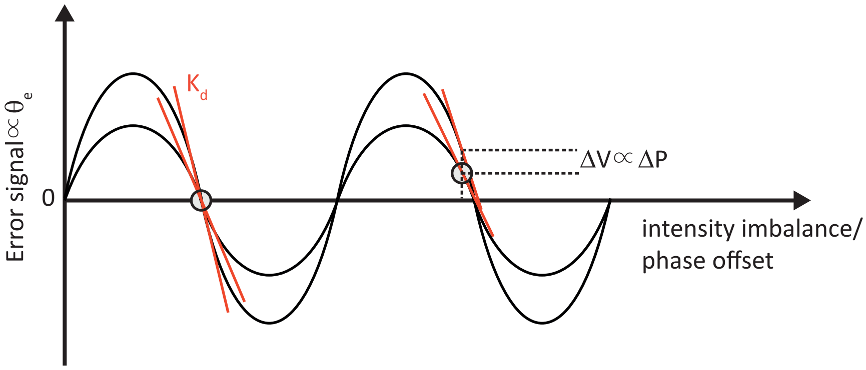

Figure 3.5.: FLOM-PD amplitude-to-phase conversion susceptibility for two different bias points (circles). With intensity-balanced detectors (left circle), fluctuations in the optical power result in a shift in the sensitivity K_d but have little effect on the error signal. For an intensity imbalance, and a nonzero DC error signal (right circle), power fluctuations not only change K_d, but also result in a shift in the error signal, and are measured as spurious fluctuations in the phase error θ_e.

wave plate with one of the pulse trains, and therefore the fast axis with the other pulse train, ensures a quarter wave, or $\pi/2$, bias between the opposite directions. After propagating through the second Faraday rotator, both pulse trains are left with their original polarisation.

After applying a $\pi/2$ phase shift, there still remains one avenue through which AM-to-PM may manifest. This is an intensity mismatch between the two detectors. In the 800 nm system, this arises principally due to the circulator insertion loss. After interference, one arm of the signal exits the 50/50 coupler and is directly detected by one of the photodiodes. The other arm, however, must propagate an additional time through the circulator before being photodetected, introducing a 25% imbalance between the two arms through the 1.3 dB insertion loss. In a noiseless system this would be no problem and would simply result in a locking point at a nonzero microwave phase. With amplitude noise, however, this is not so simple and power fluctuations in the optical pulse trains lead to spurious phase fluctuations in the error signal, as explained in Fig 3.5. This shows the output from the balanced detector for two different bias points, one with equal intensities on the two detectors (left) and an imbalanced case (right). The two sine waves represent different output voltage amplitudes as a result of optical amplitude fluctuations. In the first case (intensity balanced) fluctuations in the optical power result in a shift in the sensitivity K_d, but have little effect on the error signal. For an intensity imbalance, and a nonzero DC error signal (right circle), power fluctuations not only change K_d, but also result in a shift in the error signal, and are measured as spurious fluctuations in the phase error θ_e.

We account for such types of imbalances in the FLOM-PD with the use of a fiber-based variable optical attenuator (VOA), placed after the 50/50 coupler in that signal arm experiencing no loss due to the circulator. This will lead to some overall decrease in the sensitivity of the system, however, this is an acceptable trade off as the shot and thermal noise, as determined by the sensitivity, are orders of magnitude below the AM-to-PM limited floor. We achieve a best-possible-intensity matching of the two signals by measuring the DC level of the balanced signal with a high-resolution voltmeter and using the VOA to minimise the DC level.

The input optical power into the FLOM-PD is limited by nonlinear phase shifts in the fiber induced by high peak intensities in the fiber [86]. Effects such as self-phase modulation, leading to the generation of new frequencies, followed by dispersion, lead to imperfect interference of the counter-propagating pulse trains upon returning to the coupler. Note that in the case where the counter-propagating pulses are of the same intensity throughout the entire loop, they experience identical phase shifts and normal operation is maintained [87]. However, this breaks down in the FLOM-PD due to two factors. The coupler used in this work (FUSED-22-800-5/125-50/50-3A3A3A3A-1-1-PM, OZ Optics) had a design value of the coupling ratio of 50/50, but was measured at 47/53. While this only results in a ~12% difference in intensity between the pulse trains, the effect can become significant as it builds up over the entire loop. Furthermore, as the path lengths of the two pulse trains propagating to and from the phase modulator are different, the insertion loss of 4.5 dB of the phase modulator, equating to an attenuation of 65%, results in one direction accumulating more nonlinear effects than the other. In order to reduce imbalanced nonlinear effects, the input optical power is limited to $P_{in} = 28\,\mathrm{mW}$. After the circulator insertion loss of 1.3 dB (75% transmission) the initial average power of each pulse train is approximately 10 mW. Assuming negligible broadening of the 100 fs input pulse duration, which would only lead to a decrease in peak intensity, before being split by the coupler the pulses have a peak intensity, in the single mode fiber with mode field diameter $5\,\mu\mathrm{m}$, of 2.5×10^{10} W/cm^2. With this intensity, nonlinear effects are reduced and have a minimal contribution to the detected phase $\Delta\phi$.

3.5. Characterisation

The above sections have described the design factors which were required for construction of a FLOM-PD for operation at 800 nm. Here the fundamental limits to the performance of the FLOM-PD are derived in detail. These include the fundamental noise floor resulting from shot noise and thermal noise (as per section 2.4) as well as amplitude-to-phase conversion, detection sensitivity, and detection resolution.

Shot noise

The shot noise current density for a generated current I_0 (A^2/Hz) is given by

$$I_{\text{shot}} = 2eI_0, \tag{3.13}$$

where e is the electronic charge. This gives a shot noise after detection in the case of the FLOM-PD of

$$I_{\text{shot}} = 2eRP_{avg}, \tag{3.14}$$

where R and P_{avg} are the photodiode responsivity and the average incident optical power respectively, as above. The single-sideband phase-noise PSD as a result of shot noise fluctuations is then

$$\begin{aligned} \mathcal{L}_{\text{shot}} &= \frac{1}{2}\frac{I_{\text{shot}}G^2}{K_d^2} \\ &= \frac{e}{RP_{avg}\Phi_0^2}. \end{aligned} \tag{3.15}$$

As the applied microwave power is proportional to the square of the modulation depth, $P_0 \propto \Phi_0^2$, Eq 3.15 shows that the phase noise is inversely proportional to the input optical power and the applied microwave power. Hence the optical and microwave power should be maximised to minimise shot noise.

With a total loss in the loop (see section 3.4) of 85% ($L = 0.85$), due largely to the 4.5 dB insertion loss of the phase modulator, with further losses introduced through the circulator insertion loss (2×1.3 dB), $P_{\text{avg}} = P_{in}\,(1 - L) = 4\,\text{mW}$. The maximum microwave power is limited to $P_0 \approx 16\,\text{dBm}$ (~40 mW) to avoid multiple zero crossings over one period, as discussed in section 3.2. Under these conditions, we achieve a SSB phase noise PSD, by Eqs 3.2 and 3.15, of

$$\mathcal{L}_{\mathrm{shot}} = 1.06 \times 10^{-17}\,\mathrm{rad}^2/\mathrm{Hz} \; = -170\,\mathrm{dBc/Hz}.$$

Integration of the shot noise floor from DC up to 5 MHz, the oscillator repetition rate, shows a shot noise limited floor as low as 0.2 fs, as given by Eq 2.9.

Thermal noise

Next, the thermal noise contribution to the FLOM-PD noise floor is developed. As discussed in section 2.4, thermal noise arises from the agitation of charge carriers of nonzero temperature. From Eq 2.15, this amounts to a power spectral density at room temperature ($T = 293\,\mathrm{K}$) of $S_T = k_B T = 4.14 \times 10^{-18}\,\mathrm{W/Hz}$ (-174 dBm/Hz). The noise voltage density (V^2/Hz) at the output of the transimpedance amplifier as a result of such thermal noise is

$$v_n^2 = S_T G \tag{3.16}$$

and the SSB phase noise PSD is then given by

$$\mathcal{L}_{\mathrm{thermal}} = \frac{1}{2}\frac{v_n^2}{K_d^2}. \tag{3.17}$$

With the sensitivity in Fig 3.3a of $K_d = 0.13\,\mathrm{mV/fs}$ (3.25 V/rad), achieved at an input optical power of 28 mW and a microwave power applied to the phase modulator of 16 dBm, by Eq 3.17, the SSB phase noise as a result of thermal noise is

$$\mathcal{L}_{\mathrm{thermal}} = 6.22 \times 10^{-18}\,\mathrm{rad}^2/\mathrm{Hz} \; = -172\,\mathrm{dBc/Hz}.$$

Interestingly, under these conditions, the thermal noise floor is within a factor of two of the shot noise limited floor. As with the shot noise, the thermal noise is inversely proportional to the applied microwave power, however it is inversely proportional to the square of the incident optical power. Hence reducing the input optical power leads to a thermal noise dominated floor, while increasing the input optical power leads to a shot noise limited noise floor.

The actual noise floor of the FLOM-PD was measured by applying optical power (28 mW) without any microwave phase modulation. The measured voltage from the balanced detector in a perfect detector would then be nulled and any measured voltage is purely a result of noise, which limits the detection capability and the

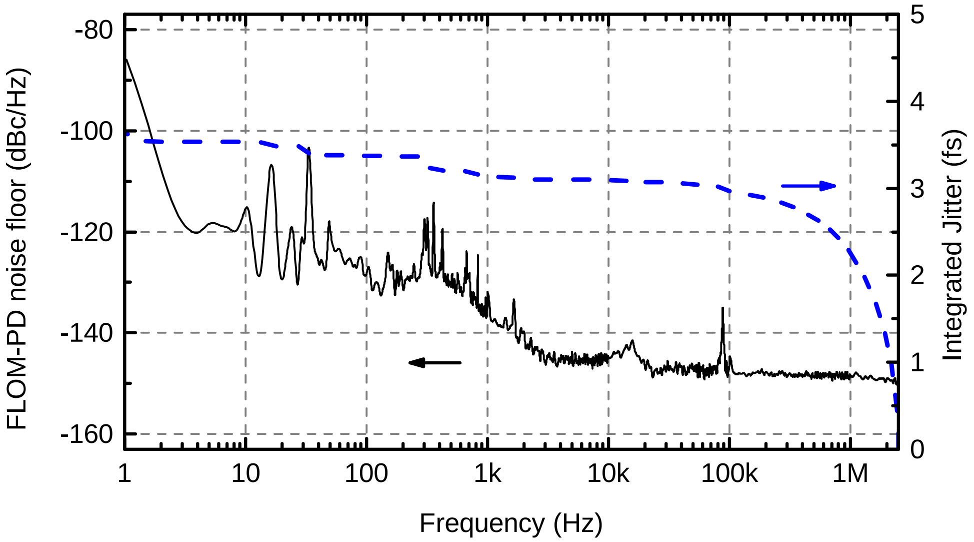

Figure 3.6.: Noise floor of the FLOM-PD, measured from 1 Hz to 2.5 MHz. The measurement was performed by measuring the error signal from the FLOM-PD with no microwave signal applied. The measured voltage is converted to a phase noise floor by assuming a sensitivity of $K_d = 3.25\,\mathrm{V/rad}$, simulating conditions with an ideal microwave. The noise floor of -148 dBc/Hz is well above the thermal and shot noise limits, and is likely a result of amplitude-to-phase conversion. Integration of the noise floor over the measured spectrum shows a lower limit of detection of the FLOM-PD of 3.5 fs.

achievable synchronisation when employing the FLOM-PD in a PLL. To convert the noise voltage into a phase noise a sensitivity of $K_d = 3.25\,\mathrm{V/rad}$ was used, despite the fact that no microwave power was applied. This effectively simulates the noise of the system with the maximum realistic applied microwave power, but does not take into account further contributions to the noise floor from the modulation process such as microwave-amplitude-to-phase couplings. With the incorporation of the VOA into the system, a nulled signal at the balanced detector occurs when the microwave phase is nulled with respect to the optical pulses and minimal microwave-amplitude-to-phase noise is expected (see section 3.3).

The results are shown in Fig 3.6, with a noise floor of -120 dBc/Hz (-148 dBc/Hz) at 10 Hz (1 MHz) offset from the carrier frequency $f_{\text{microwave}} = 6.237\,\mathrm{GHz}$. This is well above the thermal and shot noise floors of approximately -170 dBc/Hz, indicating a noise floor dominated by AM-to-PM conversion, as discussed in section

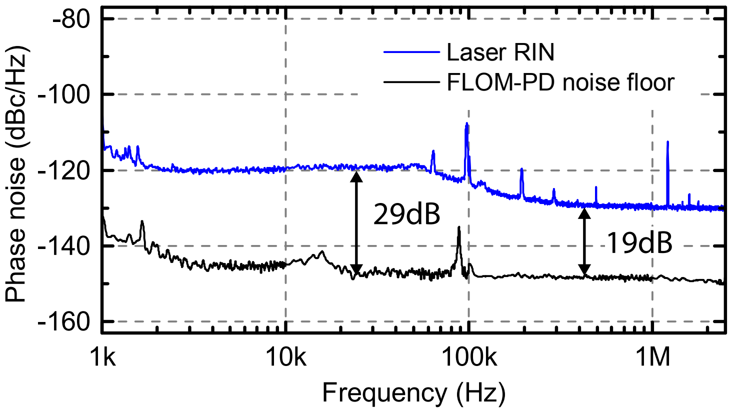

Figure 3.7.: FLOM-PD amplitude-to-phase coefficient estimation, assuming the noise floor (black, from Fig 3.6) is dominated by AM-to-PM conversion. In this case, the difference between the noise floor and the laser RIN (blue) provides an effective upper limit. The measured difference ranges between 19–29 dB, equating to an AM-to-PM coefficient of $\alpha = 0.05$–0.14 rad.

3.4. While not being able to make an out-of-loop measurement of the AM-to-PM coefficient α, which would require a second FLOM-PD, we were able to make an estimation with the assumption that the noise floor is limited by AM-to-PM conversion. With the shot and thermal noise limits decades below at -170 and -172 dBc, respectively, this was deemed a fair assumption, and the noise floor is then related to the laser RIN [67] by

$$\mathcal{L}_{\mathrm{FLOM-PD}} = \mathrm{RIN} + 20\log(\alpha) - 3. \tag{3.18}$$

This allows the calculation of α by comparison of the noise floor with the RIN. Such a comparison was made and is shown in Fig 3.7. The figure shows the laser RIN and the FLOM-PD noise floor between 1 kHz and 2.5 MHz where the plots are relatively flat. A maximum and minimum difference of 29 dB and 19 dB, respectively, is evident. By equation 3.18, this yields an AM-to-PM coefficient in the range $\alpha = 0.05$–$0.14\,\mathrm{rad}/(\Delta P/P_0)$, which agrees well with the reported values for 1530 nm FLOM-PDs in [85] of $0.06 - 0.3\,\mathrm{rad}/(\Delta P/P_0)$. Integration of the noise floor from 2.5 MHz down to 1 Hz leads to a phase detection resolution of 3.5 fs. This is 3–4 times worse than FLOM-PDs in the telecommunications band, shown to achieve attosecond locks [81,85]. Suppression of the noise floor could be feasible through either active stabilisation of the oscillator output amplitude [88], reducing the RIN, or through further suppression of the FLOM-PD AM-to-PM conversion. By compensation of unwanted offsets in the loop-filter electronics, an AM-to-PM coefficient as low as $\alpha = 0.001\,\mathrm{rad}/\left(\Delta P/P_0\right)$ has been demonstrated in [89]. Nevertheless, achieving a synchronisation, and ultimately an electron pulse duration, dictated by the FLOM-PD noise floor on a <5 fs scale would be a factor of ~20 improvement over existing UED experiments [28–30], and open the potential to study ultimately the fastest atomic and electron dynamics. The following chapters describe the application of the FLOM-PD as a high-resolution phase detector forming, first, an integral component of a PLL, and second, an out-of-loop characterisation method for a different, passive synchronisation scheme.

Chapter 4.

Active laser–microwave synchronisation with the FLOM-PD

As a first application of the FLOM-PD, laser–microwave synchronisation has been achieved by driving a voltage-controlled oscillator (VCO) via a phase-locked loop (PLL). Here, a dielectric resonator oscillator (DRO) with a carrier frequency of 6.237 GHz, to match the resonance of the microwave cavity, and an output power of 15 dBm was used. The error signal provided by the FLOM-PD drives the tuning input of the DRO and the output of the DRO is fed back to the FLOM-PD to close the PLL. Out-of-loop characterisation at low frequencies was possible with a home-built time-of-flight (ToF) spectrometer [20], and showed a jitter (integrated from 2 mHz to 5 Hz) in the synchronisation of ~50 fs. The technique, results, consequences and limitations of this approach are described in the following.

4.1. DRO characteristics

The VCO used in this work was a specially designed DRO manufactured by INWAVE AG. The oscillator had a sensitivity of 100 kHz/V and a tuning range of 0–10 V, providing an electrical tuning bandwidth of 1 MHz. Mechanical tuning of the resonance frequency by up to 50 MHz was possible around the design frequency of 6.238 GHz, to match the resonance with the desired harmonic of the Ti:sapphire oscillator. The absolute phase noise of two slightly different DROs is shown in Fig 4.1. The DRO with lower phase noise (black) had no post amplification and provided an output power of 5 dBm (DRO-6.238GHz V.2). With incorporated post amplification (HMC441, Hitite), the second DRO (DRO-6.238GHz V.3) produced

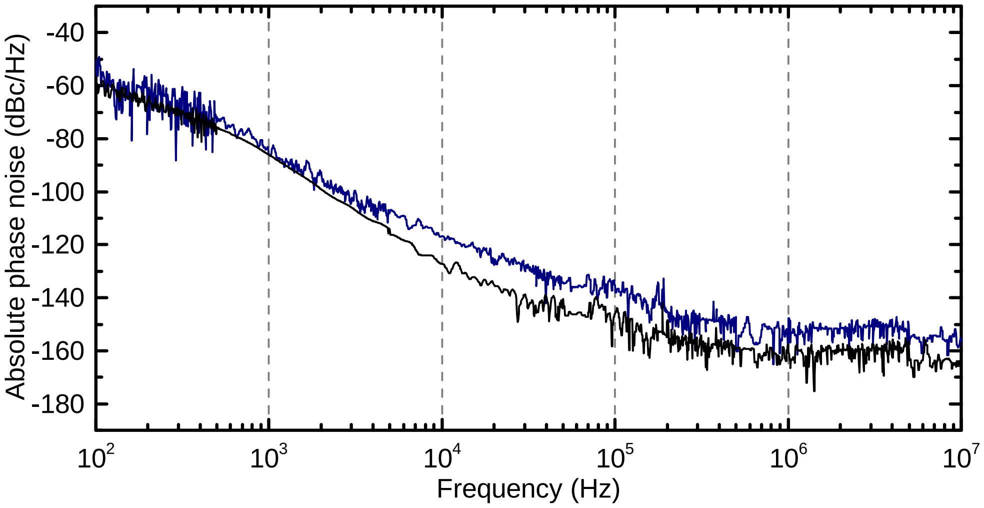

Figure 4.1.: The absolute phase noise for the INWAVE AG dielectric resonator oscillator. With no post amplification, the DRO has an output power of 5 dBm and a high-frequency phase noise of -160 dBc/Hz at an offset of 1 MHz. This was insufficient to drive the phase modulator of the FLOM-PD and further amplification was required. With post amplification provided by the HMC441 (in blue), the output is at a power of 15 dBm, at a cost of raising the noise floor to -152 dBc/Hz at 1 MHz offset.

an output power up to 15 dBm at a cost of raising the noise floor at 1MHz offset to -152 dBc/Hz.

In order to achieve the best lock, the loop filter frequency (see section 2.3) should be lower than the frequency above which the DRO phase noise is lower than the noise floor of the FLOM-PD. With slightly less microwave power available from the DRO V.3 (see section 4.3) than the calibration power used for calculation of the noise floor in Fig 3.6, a slightly higher noise floor is expected, and the afore mentioned optimum frequency was estimated at about $f_{\text{cutoff}} = 100\,\text{kHz}$.

4.2. Synchronisation measurement with ToF detection

To evaluate the performance of synchronising the DRO to the Ti:sapphire oscillator using the FLOM-PD in a PLL, we required an out-of-loop characterisation method. While the FLOM-PD provides an excellent method for characterising timing jitter, by incorporating it into the synchronisation scheme it can only provide a very limited in-loop evidence of the performance. The in-loop signal (the FLOM-PD error signal) is always close to zero within the locking bandwidth and cannot, by definition, provide the actual performance.

Therefore, we measured here the synchronisation performance through direct observation of the laser–electron delay induced as a result of the energy modulation imparted during propagation of the electrons through the microwave cavity. As discussed in section 2.1, electrons propagating through the microwave cavity experience a loss or gain in energy dependent on the microwave phase at the time of electron arrival. Electrons arriving near the microwave zero phase gain (or lose) energy almost linearly as a function of their arrival time. The arrival time of the electrons with respect to the microwave phase is dominated by two factors: the pulse duration at arrival to the cavity, and the laser–microwave jitter. Therefore, the energy distribution of the electrons after propagation through the cavity is a cross-correlation between the electron pulse duration and the laser–microwave jitter. This distribution has previously been measured by deflection of electrons in a Wien filter [25] or by the employment of a microwave cavity operating in the TEM_{110} mode [24] to characterise the jitter in UED experiments. Here the cross-correlation distribution is measured through energy analysis in the time domain with a home-built, high-resolution ToF detector developed in [48]. Details of the ToF detector can also be found in Appendix B.

With a good synchronisation scheme, the laser–microwave jitter will be much shorter than the dispersed electron pulse duration upon arrival at the microwave cavity (see section 2.1) and the cross-correlation will reflect only the duration of the electron pulses at the cavity. However as the electron pulse duration has no effect on the average energy of the streaked pulses, any shift in the central energy of the electron pulses is entirely due to the laser–microwave jitter. By analysis of the central energy of successive electron pulses, as shown in Fig 4.2a, the jitter can be extracted, albeit limited in frequency up to the rate at which such spectra can be acquired. The ToF spectrometer is capable of single-shot detection, with a quantum efficiency of approximately 50%, and is therefore ideal for this purpose.

In order to convert a measured energy shift into a phase or delay, the time dependent energy gain coefficient, g_{E} (introduced in section 2.1 and given by the microwave amplitude and frequency), in this case functioning as a linear phase-to-energy coefficient, was determined by scanning the microwave phase over a short range around a zero crossing. Fig 4.2b shows a representative measurement of g_E using the ToF spectrometer with the phase scanned by a calibrated manual phase shifter. Synchronisation measurements in this work have been performed at

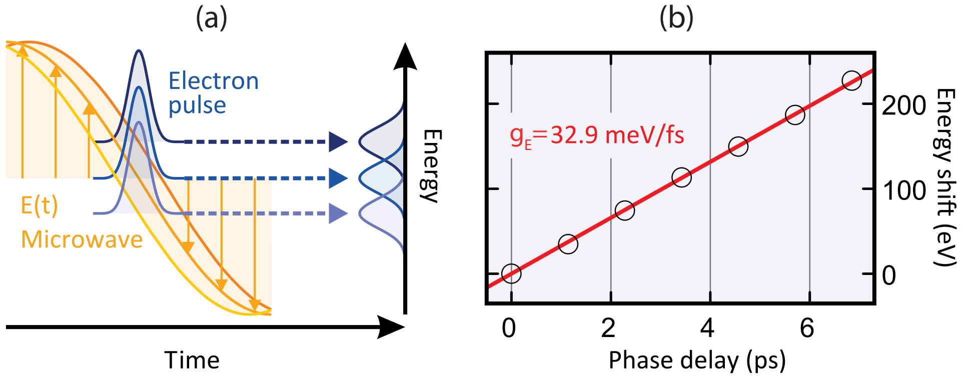

Figure 4.2.: Concept of microwave streaking of electrons propagating through the microwave cavity [90]. (a) A drift in the synchronisation causes the electrons inside the microwave cavity to experience a different phase of the oscillating electric field, leading to a shift in the central energy of the electron pulse. As long as the synchronisation drift is small with respect to the microwave period, the shift in central energy is linear with the drift. The imparted energy modulation, through time-of-flight detection, can be converted into a phase delay, or timing drift, shown in (b). A typical value for the achievable phase-to-energy coefficient with the ToF spectrometer described above is on the order of 32.9 meV/fs.

electron count rates of typically 4–5×10^5 counts per second, ensuring the single-electron-pulse regime at a laser repetition rate of 5.1 MHz. The single-shot capability of the ToF spectrometer allows for arbitrary sampling intervals, implying a trade off between a high effective sampling rate (short sampling intervals) and good statistics (long sampling intervals). We chose a sampling interval of 2 s for Fourier frequencies below ~0.1 Hz and 100 ms above ~0.1 Hz. Note that a 100 ms sampling interval corresponds to an effective Nyquist frequency of 5 Hz. The ToF spectra within each sampling interval are then fitted by a Gaussian in order to obtain their central energy, which is converted to timing drift using $g_E \approx 33\,\mathrm{eV/ps}$. The accuracy, given by a 95% confidence level of the Gaussian fits, was determined as 2 fs (2 s intervals) and 4.6 fs (100 ms intervals), respectively [90].

4.3. PLL implementation

The setup for the synchronisation measurement with the DRO-6.238GHz V.3, chosen for its higher output power to sufficiently drive the FLOM-PD phase modulator, is shown in Fig 4.3. The Ti:sapphire output is split to apply power to both the FLOM-PD and for electron generation via the photoelectric effect. The error

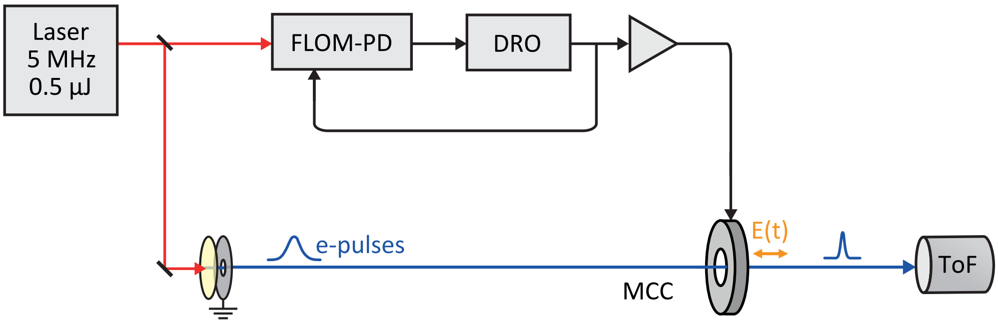

Figure 4.3.: Setup for synchronisation measurement with the DRO-6.238GHz V.3. The Ti:sapphire output is split to apply power to the FLOM-PD and for electron generation. The error signal from the FLOM-PD drives the tuning input of the DRO and the output of the DRO is fed back to the FLOM-PD to close the PLL and lock the DRO to the 1216th harmonic of the repetition rate. With a 3 dB splitter, the available power from the DRO to both the FLOM-PD and the microwave cavity is 12 dBm (as per section 4.1). To achieve a strong enough phase-to-energy coefficient (section 4.2) further amplification of the DRO output before application to the microwave cavity yielded $g_E = 14.8\,\text{eV/ps}$. The energy modulation of the electrons due to the cavity was detected as a function of arrival time by the ToF spectrometer.

signal from the FLOM-PD drives the tuning input of the DRO and the output of the DRO is fed back to the FLOM-PD to close the PLL and lock the DRO to the 1216th harmonic of the Ti:sapphire repetition rate. With a 3 dB splitter, the available power from the DRO to both the FLOM-PD and the microwave cavity is 12 dBm (as per section 4.1). In order to achieve a high enough phase-to-energy coefficient for better accuracy of the ToF detector (see section 4.2) further amplification of the DRO output was required. We used the AM53-6.2S-25-37 (Microwave Amps) before application to the microwave cavity which yielded a phase-to-energy coefficient of $g_E = 14.8\,\text{eV/ps}$, somewhat smaller than the example above, but still adequate for the synchronisation measurement. The energy modulation of the electrons due to the longitudinal electric field in the microwave cavity was then detected as a function of arrival time by the ToF spectrometer. For the two measurement modes, described in section 4.2, we acquired 500 samples each, allowing an overlapping measurement of the phase noise down to mHz frequencies. The in-loop error signal was minimised through appropriate selection of the loop filter filter frequency and gain. This resulted in a frequency of 20 kHz, somewhat lower

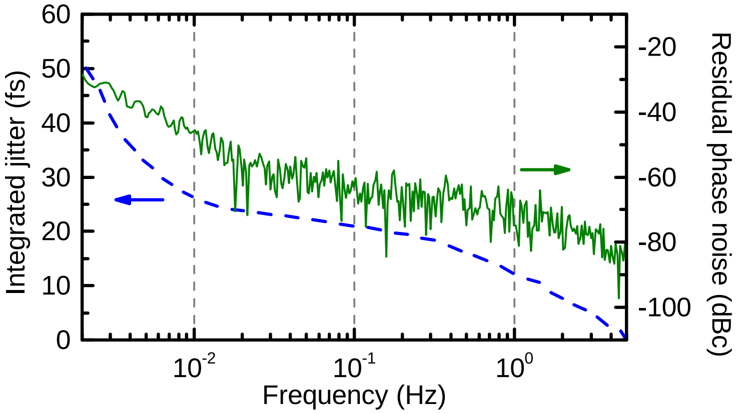

Figure 4.4.: Out-of-loop residual phase noise measurement of the DRO. The residual phase noise (in green) was measured by the ToF phase detector from 2 mHz up to 5 Hz. There are no noticeable spikes in the phase noise, however an overall high level results in an integrated jitter (in blue) of 50 fs.

than the 100 kHz mentioned in section 4.1, but allowing greater drift suppression at lower offset frequencies.

The measured out-of-loop residual phase noise is shown in Fig 4.4. The phase noise (in green) presents no noticeable spikes within the measured range. However, the relatively high phase noise in this region contributes a low-frequency jitter, integrated from 2 mHz to 5Hz (in blue) of slightly less than 50 fs. While this is within the range of the synchronisation in previously demonstrated results [29,30], it does not provide the ability to compress electrons to the few-femtosecond regime. In addition, it is possible that the high-frequency jitter could contribute substantially to the overall performance, further limiting the achievable synchronisation.

Without a second FLOM-PD available, we could not make an out-of-loop measurement in the high frequency range. However, it is possible to derive an estimation from the measurements. Outside the PLL locking bandwidth of 20 kHz the phase noise will follow the DRO phase noise. By integrating the phase noise curve in Fig 4.1 between 20 kHz and 2.5 MHz provides a jitter of <8 fs within this range, assuming no additional noise sources between the DRO output and the cavity itself. Below 20 kHz but above the ToF phase detector limit of 5 Hz, the jitter is given by the noise floor of the FLOM-PD. Integration of the FLOM-PD noise floor within this range amounts to <2 fs of jitter. With this knowledge it is fair to assume the overall quality of the synchronisation is dominated by the measurable low frequency jitter at <5Hz (~50fs), as addition of the jitter from the other regions (in quadrature) amounts to <1 fs.

While this calculation provides an estimation of the jitter outside of the range for which out-of-loop characterisation was possible, it may not prove realistic if, for example, the locking conditions were somehow unfavourable and the actual noise was higher than the FLOM-PD noise floor. However, as discussed in section 4.2, the width of the retrieved electron spectra from the ToF detector is a cross-correlation between the dispersed pulse duration at arrival to the microwave cavity τ_{disp} (see Fig 2.1), hence in principle revealing the laser–microwave jitter τ_{jitter} arising over the duration of the measurement. If enough signal-to-noise is available, it is then possible to measure the total jitter through analysis of the width of the ToF spectra [25]. The temporal width of the retrieved ToF spectra τ_{e} is given by:

$$\tau_e = \frac{\Delta E}{g_E}, \tag{4.1}$$

where ΔE is the measured energy width. The jitter is related to the calculated temporal width by [25]:

$$\tau_{\mathrm{jitter}}^2 = \tau_{\mathrm{e}}^2 - \tau_{\mathrm{disp}}^2. \tag{4.2}$$

For the beam line used in the above experiment, characterisation of the uncompressed (dispersed) electron pulse duration by optical field streaking has been previously demonstrated with a duration of (153 ± 9) fs, rms [49]. Taking the average of all the spectra acquired at 2 s sampling intervals, resulted in a statistical distribution of the standard deviation of the energy width of $\Delta E = (2.45 \pm 0.02)\,\mathrm{eV}$. With the measured phase-to-energy coefficient of $g_E = 14.8\,\mathrm{eV/ps}$, Eq 4.1 gives an rms cross-correlation duration of $\tau_{\mathrm{e}} = (165 \pm 1)\,\mathrm{fs}$. The fact that τ_{e} and τ_{disp} are very similar means that with such a large error in the measurement of τ_{disp}, we can only provide an upper limit for the jitter. By Eq 4.2, the calculated upper limit for the jitter is $\tau_{\mathrm{jitter}} = 79\,\mathrm{fs}$. This agrees well with the directly measured jitter in the region from 2 mHz to 5 Hz of 50 fs, confirming the dominant contributions arise in this range.

In summary, the best estimation of laser–microwave jitter employing an active lock with the FLOM-PD and the DRO is 50–79 fs. While this demonstrates the capability of the FLOM-PD to function very well in a PLL, the final performance is only on par with previously demonstrated results [30]. This appears to be predominantly due to the noise floor of the FLOM-PD at low frequencies. This is attributed to amplitude-to-phase couplings in the FLOM-PD (discussed in chapter 3) and arises as a result of the relative intensity noise of the laser pulses propagating in the Sagnac loop. In order to reduce the synchronisation jitter and hence the electron pulse duration down to the few-femtosecond regime, significant suppression of the FLOM-PD noise floor would be required, or alternatively, another, more stable laser system.

Chapter 5.

Laser–microwave synchronisation with direct extraction

Here, an alternative to the FLOM-PD + DRO synchronisation scheme is presented which does not require any feedback or lock [91]. In short, a mode-locked laser system operating with a repetition rate of f_{rep} being detected by a photodiode generates a current pulse train with a frequency spectrum containing components at every harmonic of the fundamental repetition rate up to the photodiode cut-off frequency [92, 93]. Filtering and amplifying one such harmonic at the desired microwave frequency $f_{\mathrm{microwave}}$ results in a microwave signal with inherent synchronisation to the laser. The synchronisation is defined only by the microwave generation scheme, arising primarily through noise introduced during the photodetection process [67]. The overall performance of the synchronisation is then limited only by the residual phase noise arising in the components used in the extraction and amplification process. The method with which this was performed, along with the considerations required to achieve the best synchronisation, is detailed below.

5.1. Microwave generation

This method for synchronisation is based on extraction of the microwave signal from a harmonic of the repetition rate after photodetection of the laser. Discussed in section 2.4, photodetection brings both shot noise and thermal noise into play, particularly when detecting low average optical power. It has recently been shown by Quinlan et al [94] that by exploiting spectral correlations in the shot noise when detecting ultrashort pulses, an orders of magnitude improvement in the shot noise floor, and consequently the timing of the generated pulse train, can be seen by the factor

$$1 - C\left(\tau\right) = 1 - \exp^{-\left(2\pi f_{\mathrm{microwave}}\tau\right)^2}, \tag{5.1}$$

where τ is the pulse width and $C\left(\tau\right)$ is the optical-pulse-width-dependent correlation factor. Note that the right-hand side of the equality in Eq 5.1 holds only for a Gaussian pulse. As the pulse length of the Ti:sapphire oscillator is optimised at the photocathode for electron generation, the pulses are considerably larger at the photodetector (as outlined below) however, the pulse duration is still subpicosecond on detection and, by Eq 5.1, we can achieve 10^{-3}or 30 dB suppression of the shot noise and the resulting shot noise is far below the thermal noise limit, as seen in the following.

The thermal noise has a constant PSD of $S_{\mathrm{thermal}} = -174\,\mathrm{dBm/Hz}$ (Eq 2.15) at room temperature. Thermal noise therefore imposes a fundamental limit on the achievable phase noise when detecting very low signal powers. Hence it is advantageous to yield the maximum possible power at $f_{\mathrm{microwave}}$ upon photodetection. However, this power is inhibited by saturation effects in photodetectors due to the high peak power of pulsed laser sources [95–97]. Space charge resulting from the generation of a high number of carriers in the depletion region leads to the formation of an electric field opposing the photodiode bias and impedes the flow of charge carriers across the diode junction. This effectively reduces the bandwidth of the detector and ultimately limits the achievable power at $f_{\mathrm{microwave}}$. Unitravelling-carrier photodiodes [98] with incorporated cliff layers [99] and flip-chip bonding [100] have been designed to circumvent this limit.

To enable generation out to the 1216th harmonic of the repetition rate of our 5.128 MHz Ti:sapphire oscillator (corresponding to a microwave frequency of $f_{\mathrm{microwave}} = 6.237\,\mathrm{GHz}$), a photodiode with a 10 GHz bandwidth (EOT, ET4000) was used. The ET4000 has a far lower linear power handling capability compared with the photodiodes presented in [99] and [100], however it is evident below that the maximum available power for photodetection in this work was still below the onset of saturation.

A measurement of the dependence of the detected power at $f_{\mathrm{microwave}}$ on the average optical power incident on this diode is shown in Fig 5.1. The output power increases for low input powers, however the onset of saturation is evident well below 1 mW, with the detected power at 6.237 GHz reaching a maximum of -47 dBm. At this power, the thermal-noise-limited noise floor of the photodetected microwave signal amounts to -127 dBc/Hz. Amplification of the signal only further degrades the signal-to-noise (SNR) ratio. To suppress the contribution of thermal

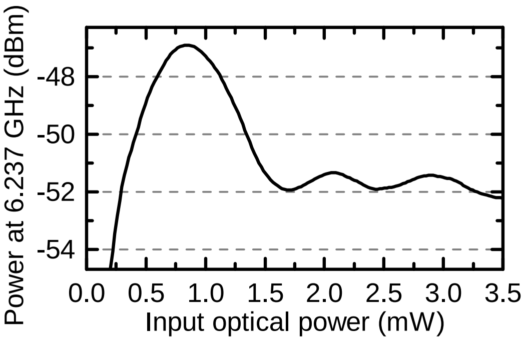

Figure 5.1.: Output power dependence of the power in the 1216th harmonic of the laser repetition rate as a function of the incident optical power on the photodiode; figure taken from [91]. Saturation due to the high pulse energy sets in below 1 mW, with the generated microwave power reaching a maximum of -47 dBm.

noise, we implemented a repetition-rate multiplication technique to enhance the microwave power prior to photodetection [91].

Microwave enhancement with an optical-mode filter

Repetition-rate multiplication is a concept for redistributing the optical power in a laser pulse train from the fundamental of the repetition rate to a harmonic thereof. This has been successfully demonstrated in the past with optical-mode filtering [96, 101, 102], and pulse interleaving with cascaded Mach-Zehnder interferometers [79, 103]. While the latter technique has the distinct advantage of a high throughput, the multiplication is governed by the factor 2^n, where n is the number of Mach-Zehnder stages. This becomes a problem at high multiplication factors as not only must one implement a large number of stages, but the possible operation frequencies become much more limited. With a 5 MHz oscillator, the only possible microwave frequencies are 5 GHz and 20 GHz (for $n = 10,11$, respectively), both of which fall well outside the resonance bandwidth of the microwave cavity.

Instead, we implement an optical-mode filter, using a Fabry-Perot cavity with a free spectral range matching the desired harmonic of the laser repetition rate. The mode filter consists of two mirrors mounted on a single steel block, separated by a distance L, and convert an incoming laser pulse train at f_{rep} to a series of decaying pulse trains at

$$f_{\mathrm{microwave}} = \frac{c}{2L}. \tag{5.2}$$

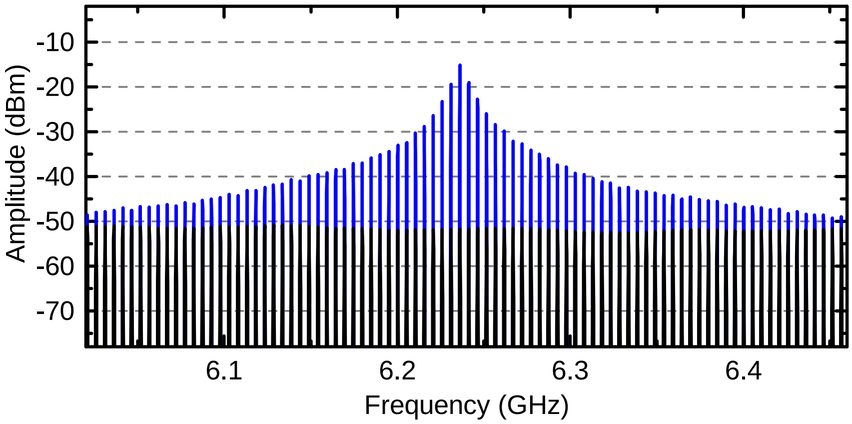

Figure 5.2.: Microwave enhancement with the optical-mode filter. In blue is the photodetected microwave power with 2.3 W average power available for optical-mode filtering, yielding ~2.5 mW incident on the photodiode. With optimised alignment, a power of -15 dBm was achievable at $f_{\text{microwave}} = 6.237$ GHz, providing an enhancement of ~35 dB over the unmode-filtered case (black) when illuminated with the same incident power. The neighbouring modes at $f_{\text{microwave}} \pm f_{\text{rep}}$ are suppressed by 4 dB.

Employment of the mode filter therefore serves to spectrally redistribute the optical power into multiples of $f_{\text{microwave}}$ and has two main consequences. Firstly, this results in an increase in the photodetected microwave power for the same incident optical power, compared to the unfiltered case. Second, with lower pulse energies, this increases the incident average optical power at which the onset of saturation occurs. The mode filter was designed so that the generated pulse train at $f_{\text{microwave}}$ decays almost completely before the next laser pulse arrives, to avoid optical interference and the need for active stabilisation of the optical path length. However, one pulse from the laser still circulates >1000 times, so suitable mode matching of the laser with the mode filter was required to maintain stability. Toward this end, both mirrors have a reflectivity of $R = 99.75 \pm 0.05\%$ and a radius of curvature of 200 mm, and are separated by $L = 24$ mm (defined by Eq 5.2). The enhancement of the microwave power as a result of the mode filter is shown in Fig 5.2. With 2.3 W of average power from the laser incident on the mode filter, yielding ~2.6 mW at the photodiode, this enables a photodetected microwave power of -15 dBm (blue trace). This is an enhancement factor of 35 dB, or ~4000, over the achievable power with direct detection (i.e no mode filter; black trace), under the same illumination power. This effectively suppresses the thermal noise to a level of -159 dBc/Hz, equating to a fundamental lower limit of the jitter, by Eq 2.9, of 0.45 fs in a 2.5 MHz bandwidth. This is greater than a factor of 50 than the achievable lower limit without the mode filter of 25 fs; the mode filter is essential to opening the possibility of a few-femtosecond synchronisation.

Note that with 2.6 mW of incident power, the photodetected microwave power is saturation limited (evident in Fig 5.1) under direct illumination. As mentioned above, saturation is a result of high peak powers degrading the photodiode bandwidth. Optical-mode filtering converts a pulse of energy E to a decaying pulse train of much lower energies. The energy E_n of the n^{th} pulse in the decaying pulse train can be written in terms of the energy E_1 of the strongest pulse (i.e the first pulse) as

$$E_n = E_1 R^{2(n-1)}. \tag{5.3}$$

The total energy E_{tot} in the pulse train is then

$$\begin{aligned} E_{tot} &= \sum_{n=1}^{\infty} E_n = E_1 \sum_{n=1}^{\infty} R^{2(n-1)} = E_1 \sum_{n=0}^{\infty} R^{2n} \\ &\approx E_1 \int_0^{\infty} R^{2n} dn. \end{aligned} \tag{5.4}$$

The energy of the first pulse, in terms of the total energy is then

$$E_1 \approx -2 \ln (R)\, E_{tot}. \tag{5.5}$$

The onset of saturation from Fig 5.1 is at an incident average power of ~0.75 mW with a pulse energy of ~150 pJ. At the maximum available power from the mode filter of ~2.6 mW, Eq 5.5 yields a maximum pulse energy of only 2.6 pJ, indicating a level well below saturation. This is important as saturation not only limits the achievable microwave power, but also contributes to amplitude-to-phase couplings in photodiodes [95, 104] and can severely degrade the achievable synchronisation.

Minimisation of photodiode amplitude-to-phase conversion

As mentioned above, the generation of a high number of carriers from intense illumination of a photodiode leads to a reduction in the response time of the photodiode, limiting the achievable microwave power causing amplitude-to-phase conversion. When illuminated by ultrashort laser pulses, the generated photocurrent from a diode is a pulse train of duration determined by the longer response time of the photodiode. With low power and linear operation, this response does not change significantly with increasing power. However, after the onset of satura-

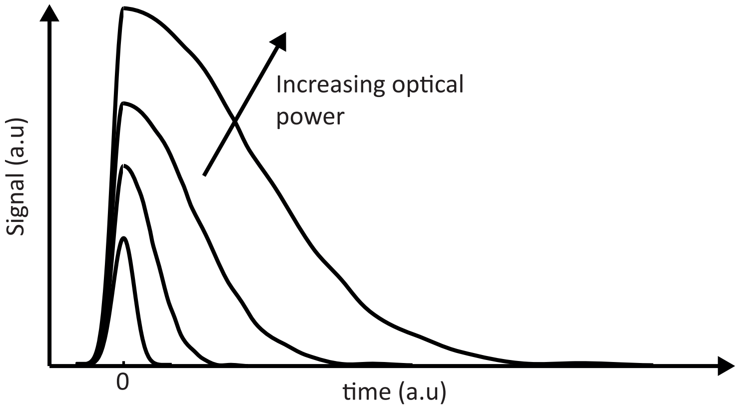

Figure 5.3.: Photodiode response for increasing incident optical power. For low incident powers, the peak response increases linearly and the generated current pulses are undistorted. At higher powers, saturation begins to limit the output level, and the reduced response time leads to a shift in the centre of mass of the generated pulses.

tion, the degradation of the response time leads to a slow decay of the pulse and a shift in the centre of mass of the generated pulse, as illustrated in Fig 5.3.

The rms phase drift arising from laser power fluctuations has been measured and characterised in [67, 105] with interesting results. Firstly, the amplitude-to-phase conversion coefficient α, measured in radians per fractional power fluctuation (rad/($\triangle P/P$)), is unique to each photodiode and dependent on the physical design. Distribution of the incident power uniformly over the depletion region reduces α compared to illumination at equal power with less ideal irradiation. Importantly, at certain powers above saturation α can be nulled. Critically, these “vanishing points” only exist within a very narrow incident power range and a small deviation in the incident power results in a substantial shift in α. However, by exploiting two detectors exhibiting a strong negative correlation in their noise characteristics, a reduction in α to below $0.06\,\mathrm{rad}/(\triangle P/P)$ for a range of incident pulse energies has been demonstrated [106].

A measurement of α for the ET4000 was performed by attenuating the beam after the optical-mode filter and measuring the resultant phase shift at $f_{\mathrm{microwave}}$. The setup is shown in Fig 5.4a. Amplification of the signal was required after photodetection in order to achieve enough power to drive the mixer, however, after thermalisation, the amplifier had no noticeable effect on the phase of the signal. The signal was mixed in a double balanced mixer with a reference signal with the output a voltage proportional to the phase difference (described in detail below in section 6.1). The result is shown in Fig 5.4b when using the maximum achievable

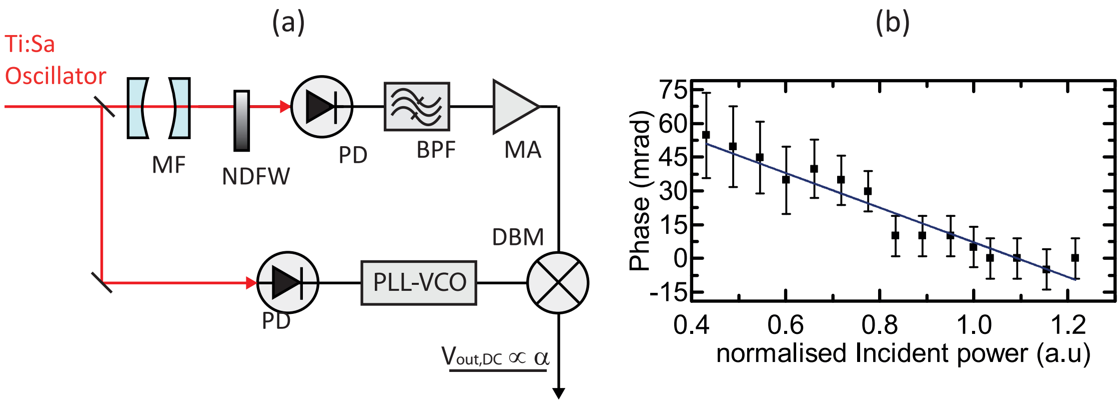

Figure 5.4.: (a) Setup for AM-to-PM coefficient α measurement. The beam after the mode filter (MF) is attenuated with a neutral density filter wheel (NDFW) before detection with the ET4000 photodiode (PD). The signal is then band-pass filtered (BPF) and amplified to a level sufficient for mixing in a double balanced mixer (DBM). The reference is a phase-locked VCO. This results in an output voltage proportional to the phase difference between the two arms. (b) The ET4000 exhibits a linear phase response as a function of incident power. The fitted slope yields $\alpha = 0.077 \pm 0.007\,\mathrm{rad}/(\triangle P/P)$.

power after the mode filter of ~2.6 mW. The phase response of the photodiode is linear with optical power, yielding $\alpha = 0.077 \pm 0.007\,\mathrm{rad}/(\triangle P/P)$. This value is yielded as we are well below the onset of saturation, and below any measureable vanishing point. This will result in a noise floor of the extracted microwave approximately 25 dB (Eq 3.18) below the RIN of the Ti:sapphire oscillator (blue curve in Fig 3.7), assuming α is relatively frequency independent. This would lead to an AM-to-PM phase-noise floor of -145 dBc/Hz (-155 dBc/Hz) at 10 kHz (1 MHz) from which we draw the conclusion that the residual phase noise of the extracted microwave is most likely dominated by AM-to-PM, due mostly to the thermal noise suppression achieved with the optical-mode filter.

Electrical amplification by 50 dB to 33 dBm (2 W)

Post mode filtering and photodetection, we had a current pulse train containing an impressive -15 dBm (~30 μW) at $f_{\mathrm{microwave}}$. However, electron pulse compression requires a power of approximately 33 dBm (2 W) in an ideally sinusoidal signal. This necessitated the design of an electrical amplification chain to boost the signal strength by 48 dB.

Electrical amplification degrades the synchronisation by adding to the phase noise of the signal and is characterised through the amplifier *noise factor* (F) (or *noise figure* — $NF = 10\log(F)$). The noise factor is defined as the input to output noise ratio, $F = SNR_{in}/SNR_{out}$. Intuitively, it would seem the smaller the total F from all amplifiers, the better the noise performance, however Friis [107] showed that the overall noise factor F_s of a system is

$$F_s = F_1 + \frac{F_2 - 1}{G_1} + \frac{F_3 - 1}{G_1 G_2} + \dots \frac{F_n - 1}{G_1 G_2 G_3 \dots G_{n-1}}, \tag{5.6}$$

where G_n is the gain of the n^{th} amplifier in the network. From the equation, it is evident that the noise added to the system for the n^{th} stage is reduced by a factor in proportion to the gain of all the previous stages combined; that is, the noise of successive amplifiers impacts the system less and less. With typical values $F_i = 3$ and $G_i = 10^3$, F_s increases only from 3 to 3.002 when going from a one to two amplifier system; F_s is dominated by F_1, the noise factor of the first stage. In systems where a substantial level of amplification is required, low-noise amplifiers [108] are typically used as the first amplifier. In cases where amplitude stability is of utmost importance, saturating amplifiers, which accept a range of input powers and amplify everything to a constant specified output power, can be used to suppress amplitude fluctuations of the microwave. This, however, comes at the expensive of phase stability, with the output phase typically varying a few degrees per dB of input power fluctuation. This is unacceptable for systems which require few-femtosecond synchronisation.

The final high-power microwave for electron-pulse compression was achieved with two microwave amplification stages. The first amplifier (CA67-451, Ciao Wireless) had a noise factor of $F \approx 2$ ($NF = 3\,\mathrm{dB}$) and amplified the signal directly after the photodiode from -15 dBm to 5 dBm, and the second amplifier (AMF-4B-05900640-50-36P, MITEQ) from 5 dBm to 33 dBm (2 W).

Time domain consequences of the neighbouring harmonics

Prior to each amplification stage the signal was band-pass filtered (PLC6237DB006-1, Proline) within a few MHz of bandwidth about $f_{\mathrm{microwave}}$ to further suppress the other harmonics of the repetition rate. This resulted in a suppression of the nearest neighbouring harmonics at $f_{\mathrm{microwave}} \pm f_{\mathrm{rep}}$ by about 15 dB. When this microwave is used for compression, the suppression increases to 30 dB inside the microwave cavity due to its narrow bandwidth (~2 MHz) [25].

Effectively, inside the microwave cavity the carrier frequency $f_{\text{microwave}}$ is 1000 times stronger stronger (30 dB) than the strongest neighbouring components, at $f_{\text{microwave}} \pm f_{\text{rep}}$. While this is a huge suppression of the sidebands, femtosecond synchronisation requires a high stability, and the effect of the sidebands on the few-femtosecond-level jitter needs to be estimated.

The microwave signal inside the cavity is a superposition of all the harmonics which exist after photodetection, filtering and amplification; the electric field $E_{\text{microwave}}(t)$ of this directly detected signal has the form

$$E_{\text{microwave}}(t) = \sum_{n=1}^{N} a_n \sin\left(2n\pi f_{\text{rep}} t + \phi_n\right), \tag{5.7}$$

where a_n and ϕ_n are the amplitude and relative phase of the n^{th} harmonic, and $N = f_{\text{cutoff}}/f_{\text{rep}}$ is given by the photodiode cutoff frequency f_{cutoff}. Treating only the nearest two sidebands gives

$$\begin{aligned} E_{\text{microwave}}(t) =& A(\sin\left(2\pi f_{\text{microwave}} t\right) \\ &+ \frac{1}{1000}\Big[\sin\left(2\pi\left\{f_{\text{microwave}} - f_{\text{rep}}\right\} t + \phi_l\right) \\ &+ \sin\left(2\pi\left\{f_{\text{microwave}} + f_{\text{rep}}\right\} t + \phi_u\right)\Big], \end{aligned} \tag{5.8}$$

where ϕ_l and ϕ_u are the relative phases of the lower and upper sidebands with respect to $f_{\text{microwave}}$, respectively. Assuming these phases are dominated by the phase response of the microwave cavity (shown in Fig 6.4) then $\phi_l = -\phi_u$ and Eq 5.8 in fact describes an amplitude modulation of the form

$$E_{\text{microwave}}(t) = A\left[1 + M\cos\left(2\pi f_m t + \phi\right)\right]\sin\left(2\pi f_c t\right), \tag{5.9}$$

with a modulation frequency $f_m = f_{\text{rep}}$, modulation depth $M = 1/500$, around a carrier frequency $f_c = f_{\text{microwave}}$. This will effect the microwave compression strength g_E (defined in section 2.1) through variations in the peak amplitude of the signal by a factor 10^{-3}. This has the consequence that changes in g_E will result in a change in the final electron pulse duration τ_{final} . This effect is linear, however, and will therefore only result in changes on the order of attoseconds (Eq 2.1). The modulation does not effect the frequency and therefore does not effect the linearity of the signal about the zero crossing. Hence, residual sidebands introduce no significant nonlinear distortions when manipulating the electron phase space for optimum compression. Having taken all of the above considerations into account, a synchronisation on the order of, or even better than, the DRO synchronisation scheme presented in chapter 4 was expected.

5.2. Experimental setup

Similar to the characterisation of the PLL performance described in chapter 4, we used the ToF phase detector to make an out-of-loop characterisation of the synchronisation of the directly extracted microwave with the Ti:sapphire oscillator at low frequencies. Furthermore, by combination of this measurement and implementation of the FLOM-PD as a high-frequency phase-detector, we performed a complete out-of-loop characterisation over nine frequency decades. The setup for the experimental implementation is shown in Fig 5.5. The full laser power was incident on the optical-mode filter for microwave extraction and subsequent amplification, as described in section 5.1. The reflected beam was separated from the input beam with a Faraday isolator (FI) and split into two arms to provide references for the two separate characterisation systems. One arm containing 40 mW, ensuring nonlinear effects in the fiber were kept minimal (see section 3.5), was coupled into the FLOM-PD for high frequency phase detection. 16 dBm (40 mW) of the extracted microwave was split from the available 33 dBm to drive the phase modulator in the FLOM-PD. The resulting spectrum of the error signal from the FLOM-PD was measured with a spectrum analyser (E4447A, Agilent) and converted to a phase noise through the calibrated sensitivity. Note that splitting the microwave prior to the cavity does not reflect the jitter as seen by the electrons. This is taken into account in section 5.3 below. The second arm from the laser was frequency tripled and used for generation of electrons for low frequency phase detection with the microwave cavity + ToF measurement technique. Enough laser power was used here to generate one-tenth of an electron on average per pulse, as discussed in section 4.2. The rest of the microwave power, 30 dBm, was applied to the microwave cavity.

5.3. Jitter characterisation

Under the above conditions, the phase error sensitivity from the FLOM-PD was measured at $K_d = 3.25\,\mathrm{V/rad}$, while the ToF had a phase-to-energy coefficient of $g_\mathrm{E} = 33\,\mathrm{eV/ps}$. The out-of-loop relative phase noise between the directly extracted

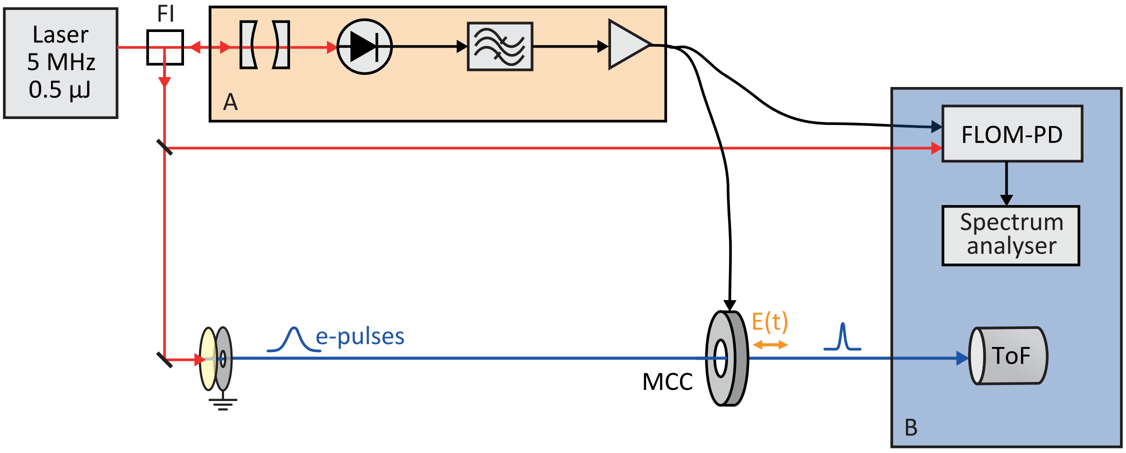

Figure 5.5.: Setup for the synchronisation measurement. The full laser power was incident on the optical-mode filter for microwave extraction. The reflected beam (99.75%) was split into two further beams after separation from the incoming beam with a Faraday isolator (FI). The remaining two beams were used for electron generation and coupling into the FLOM-PD. A: The direct extraction scheme described in section 5.1. Optical-mode filtering prior to photodetection followed by band-pass filtering and amplification provided a useable power of close to 33 dBm (or 2 W). B: The microwave was split, with 30 dBm being applied to the microwave cavity (MCC) for the low frequency phase noise measurement with the time-of-flight detector (ToF), as described in section 4.2, and 16 dBm applied to the phase modulator in the FLOM-PD for the high-frequency phase noise measurement.

microwave and the laser was measured from 2 mHz to 2.5 MHz and is shown in Fig 5.6. The measurement performed with the ToF spectrometer is shown in green, while the FLOM-PD measurement is in black. As the high frequency measurement was taken before being coupled into the microwave cavity (see Fig 5.5) the black curve is the result after multiplying the measured data (in grey) with the normalised transmission function of the cavity, as it is a more realistic representation of the synchronisation with regards to electron compression capability. This only has a noticeable effect at larger offset frequencies where the transmission drops significantly. At acoustic frequencies in the Hz–kHz range, there are some noticeable spikes in the phase noise originating from mechanical vibrations and acoustic noise in the laboratory, but the region of most prominent acoustic noise (between 280 Hz and 460 Hz) contributes only ~0.15 fs to the jitter as it is overshadowed

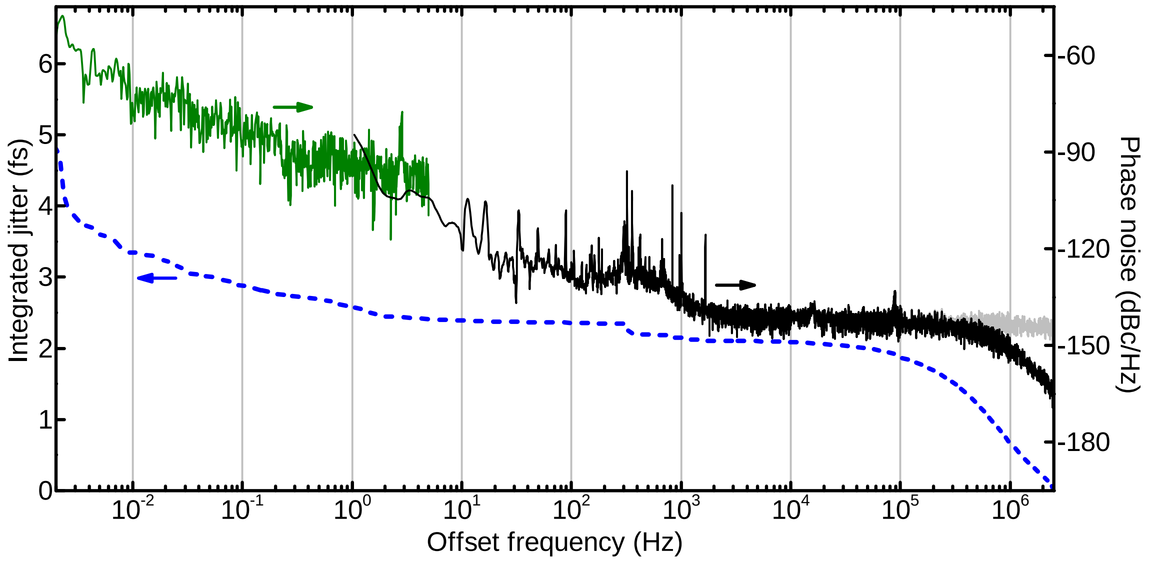

Figure 5.6.: Integrated jitter for the free running directly extracted microwave [90]. In black is the FLOM-PD measured high frequency phase noise of the free running microwave at 6.237 GHz relative to the laser, corrected for the transmission function of the microwave cavity. In grey is the uncorrected data. In green is the ToF spectrometer measured low frequency phase noise. In blue is the integrated jitter, showing from the Nyquist frequency of 2.5 MHz down to 2 mHz yields less than a 5 fs jitter.

by the contribution from the high-frequency noise floor. The phase noise in the region 2 kHz–1 MHz is at a level of -147 dBc/Hz, showing that the residual phase noise is indeed most likely limited by AM-to-PM conversion of the photodiode (see section 5.1). This result however, after taking into account the noise figure of the amplification chain, is still >20 dB better than the thermal noise limited floor achievable without the incorporation of the mode filter. Below 1 Hz, there are no noticeable spikes, but the overall phase noise increases, as a result of increasing laser RIN. Integration of Fig 5.6 from the Nyquist frequency down to 2 mHz (~8 minutes) yields a remarkable laser–microwave timing jitter of 4.8 fs (rms) [90]. However, the measured high-frequency phase noise of -147 dBc/Hz is very similar to the FLOM-PD error signal noise floor (Fig 3.6). Therefore, the corresponding contribution to overall jitter may well be an upper limit and the scheme could actually perform better. Nevertheless, this is a factor of 20 better than in state of the art ultrafast electron diffraction [29, 30]. We mainly attribute this pleasant result to the purely passive synchronisation scheme, with the microwave extracted

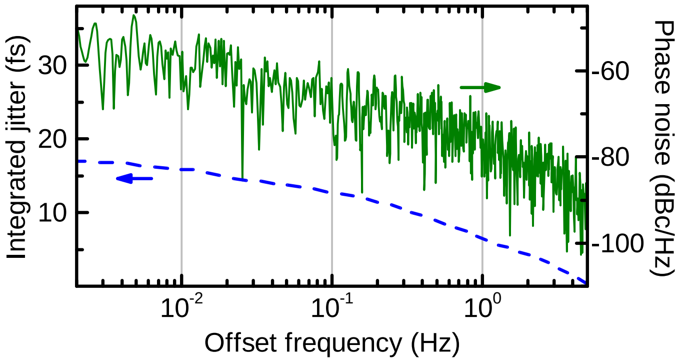

Figure 5.7.: Synchronisation with direct extraction implemented in a DLL. As the FLOM-PD was used for phase-error detection, only the ToF-detected low-frequency measurement was possible. By implementing the DLL, while there are no noticeable spikes, however, an increase of the phase noise of 5–10 dB is evident over the free running case (Fig 5.6). Similar to the PLL using the DRO, the performance here is limited by the noise floor of the FLOM-PD, and results in a 17 fs jitter, integrated from 2 mHz to 5 Hz.

directly from the Ti:sapphire oscillator via optical-repetition-rate multiplication, thus circumventing thermal noise problems while simultaneously maintaining low pulses energies to avoid saturation and consequently high AM-to-PM conversion in the photodiode.

We performed a further synchronisation attempt in the form of active stabilisation using the FLOM-PD in a delay-locked loop (DLL), the result of which is shown in Fig 5.7. With only one FLOM-PD, a complete out-of-loop characterisation was not possible, as with the locked DRO in section 4.3, and the measurement is only the low-frequency (below 5 Hz) phase noise achievable with the ToF spectrometer. By examining the figure, it is immediately evident that the DLL actually adds noise into the system (at least over the measureable range) and has a phase noise approximately 10 dB higher than the in the free-running case of Fig 5.6. An integrated jitter between 2 mHz and 5 Hz of 17 fs, greater than the free-running jitter integrated over the entire spectrum, further reinforces that a lock is hindered by the laser-RIN-limited FLOM-PD noise floor, as evidenced in section 4.3.

Suppression of the AM-to-PM conversion in the FLOM-PD, as described in section 3.5, could greatly improve these limitations and reduce the jitter toward the subfemtosecond regime. Reduction of the AM-to-PM conversion in the photodiode for a direct synchronisation scheme is another possibility for reducing the jitter without the DLL, however there is not such an advantage to be gained in this respect. The AM-to-PM limited residual phase noise is less than 10 dB above the thermal noise floor (above 2 kHz where the majority of the jitter arises) and further improvement beyond this would not lead to any further reduction in the jitter. The best possible jitter in this case would be on the order of 1 fs. Thermal noise in the FLOM-PD on the other hand is in fact lower than the shot-noise floor of -170 dBc/Hz (section 3.5). With active laser intensity control, a shot-noise-limited phase-noise floor of the FLOM-PD, and hence attosecond-level feedback, is in principle achievable [81, 85, 109] offering potential for yet another regime of jitter control.

5.4. Further considerations for electron compression

The few-femtosecond jitter demonstrated here is a factor of 20 better than in other UED systems [29, 30] and solves one of the key problems in producing few-femtosecond electron pulses by microwave compression. However, few-femtosecond laser–microwave synchronisation does not directly entail few-femtosecond electron pulses. This is outlined and discussed in the following.

It has been shown that by reversal and stretching of the linear energy chirp with microwave compression, an electron pulse duration at the target position (position of the diffraction sample) on an attosecond scale is achievable [22, 23]. With a 5 fs laser–microwave jitter this implies a synchronisation-limited achievable pulse duration of a few femtoseconds. However, when dealing with such short time scales, design of the electron beam line becomes a critical factor.

Distortions in magnetic lenses [55] have been shown to impart an axial “banana” shape on an electron pulse as, inside the lens, the electrons experience a longitudinal velocity which decreases in proportion to their distance from the axis. We modelled the effect of this for our beam line with particle tracing simulations [110] and Fig 5.8a shows the resulting electron pulse duration as a function of propagation distance. The simulation assumed ideal laser–microwave synchronisation (that is, 0 fs jitter) and was performed including all components in the experimental beam line. Electrons are generated at $x = 0$ m from a gold photocathode of work function ~4.2 eV [46] being illuminated by the 3rd harmonic of the Ti:sapphire oscillator (266 nm, 4.66 eV). The initial pulse duration of 30 fs is a result of the laser pulse duration. Note that all pulse durations stated here are rms durations. Heavy dispersion occurs over the region $x = 0 \rightarrow x = 0.003$ m, where static acceleration

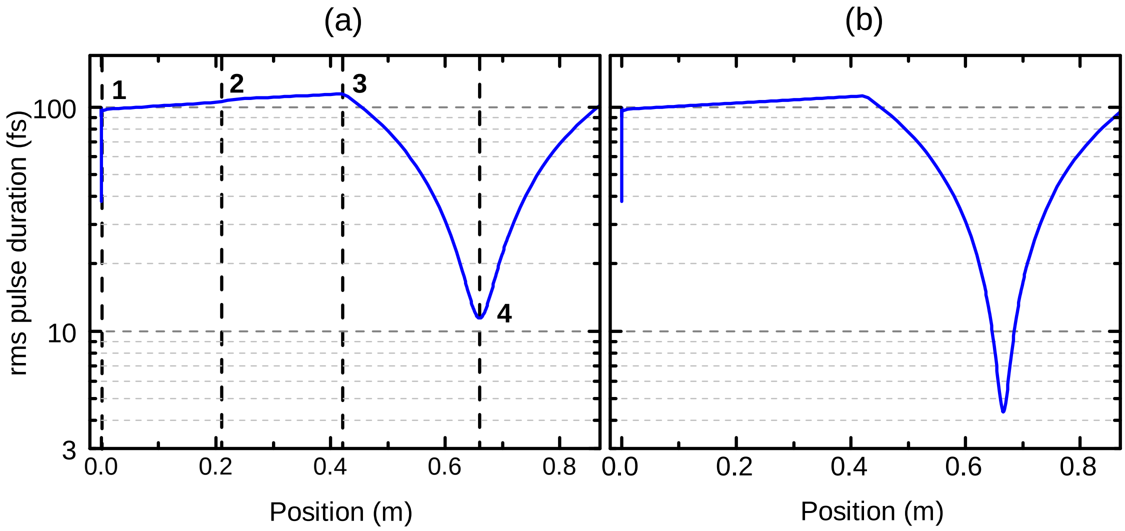

Figure 5.8.: GPT simulation of the electron pulse duration under the actual experimental conditions in the laboratory, assuming perfect synchronisation. (a) Shows the 1: static acceleration leads to pulse broadening from 50 fs to 100 fs. 2: Transverse focusing with a magnetic lens after 210 mm leads to temporal distortions of the electron beam [55]. 3: Propagation through the microwave cavity (using a field map from [42]) at 425 mm inverts the phase space of the pulse and leads to compression. 4: At a sample position of 660 mm, the electrons reach a minimum duration of 10.4 fs. (b) shows the pulse duration of the on-axis electrons under the same conditions as in (a). As these electrons all pass through the magnetic lens along the same trajectory, no distortions are seen and the pulse duration compresses to 4.4 fs at the sample position.

in a 8.33 MV/m field accelerates the electrons to 25 keV, yielding a 100 fs pulse duration. Further dispersion increases the pulse duration until $x = 0.425\,\mathrm{m}$ where the microwave cavity (using a field map from [42]) inverts the phase space of the pulse and compression begins. Note that at the magnetic lens position of $x = 0.21\,\mathrm{m}$ a very slight steepening of the dispersion can be discerned. The pulses compress until reaching the sample position at $x = 0.66\,\mathrm{m}$, reaching a minimum rms duration of 10.4 fs. This result is more than twice as long as the jitter in the synchronisation and shows that the jitter is likely contributing minimally to the overall electron pulse duration. Fig 5.8b shows the result of only the on-axis electrons which all experience the same field in the magnetic lens and hence are not influenced by lens induced distortions. These are capable of being compressed to 4.4 fs, which is very close to the limit of microwave compression with a strength $g_E = 33\,\mathrm{eV/ps}$

(Eq 2.1). In this case, the duration is on par with the laser–microwave jitter, and the pulse would broaden by only a factor of $\sqrt{2}$. This shows that the microwave has been synchronised with the laser to such a level that jitter is no longer the dominant factor for producing ultrashort electron pulses.

5.5. Compressed pulse duration

In this section, the compressed electron pulse duration with 5 fs laser–microwave synchronisation, measured with an optical field streaking technique [111] is presented [112]. In short, when an electron and an optical plane wave interact in free space without any external influences, the electron experiences oscillatory motion due to the optical field. Post interaction, a zero net change in the electron energy results due to the zero time integral of the electric field over the complete pulse. Optical field streaking on the other hand, is based on the rapid injection (or ejection) of electrons into (or out of) a controlled optical field, whence the electrons experience forces only from a part of the streaking pulse, resulting in a non-zero net transfer of energy between the field and the electrons [111, 113–116]. The experimental concept and implemented setup can be found in Appendix A.

The results of the streaking experiments are shown in Fig 5.9. Zero energy gain refers to the central electron energy of 25 keV and negative delay times indicate an early arrival time with respect to the streaking field. The counts are shown as either a loss or gain in electrons, with the measured data being subtracted from an unstreaked background, thus showing the energy redistribution as a result of the streaking. Progressively, from left to right, shows the effect of increasing the microwave compression strength g_{E}, achieved via increasing the microwave amplitude, controlling the location of the temporal focus as described by Eq 2.2. The slant of the regions of loss in electrons (shown in blue) reveals, and allows one to visualise, the chirp of the electron pulse at the foil, further emphasised by the white dashed lines. The central panel presents a minimum duration of the measured spectra when the compression strength was tuned to $g_{\mathrm{E}} = 20.1\,\mathrm{eV/ps}$, corresponding to an input microwave power of $P_{in} = 100\,\mathrm{mW}$ [112], such that the temporal focus coincided with the foil. The temporal width of the spectrogram is a convolution of the laser field with the electron pulse. However, as the electron pulse duration here is expected to be much shorter than the laser pulse envelope, the energy gain profile follows the envelope of the streaking pulse. Extracting the short electron pulse duration from this spectrogram was still achievable by analysis of only the electrons with maximal energy gain, resulting from only the

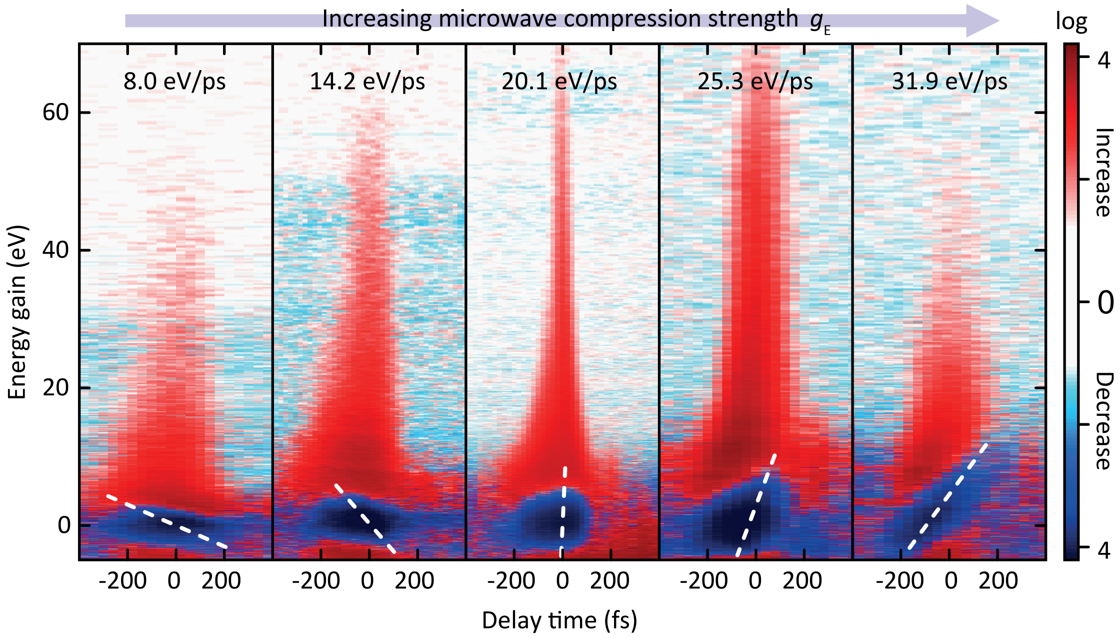

Figure 5.9.: Laser streaking of compressed electron pulses, figure from [112]. Negative delay times indicate an early arrival time at the location of the laser streaking foil. Electrons gain energy from interaction with the laser field. From left to right shows the result of increasing the microwave compression strength g_E, controlling the location of the temporal focus as described by Eq 2.2. The slant of the regions of loss in electrons (blue) reveals the chirp of the electron pulse at the foil, clarified by the white dashed lines. The central panel presents a minimum duration of the measured spectra when the compression strength is tuned, at $g_E = 20.1\,\text{eV/ps}$, such that the temporal focus coincides with the foil. The temporal width of the spectrogram is a convolution of the laser field with the electron pulse. A measure of the pulse duration is achievable by analysis of the region of maximal electron energy gain, which results from only the most intense part of the laser envelope [112], yielding an rms pulse duration of 12 ± 2 fs (28 ± 5 fs full width at half maximum) and shows good agreement with the simulated pulse duration (section 5.4 above) assuming perfect laser–microwave synchronisation. This measurement shows that contributions to the electron pulse duration from jitter in the laser–microwave synchronisation is minimal.

most intense portion of the 50 fs streaking pulse. Integration of the top 15 eV distinguishable from the figure resulted in an rms cross-correlation duration of (15 ± 1) fs [112]. Through simulations, the electron pulse duration was able to be deconvoluted from the cross-correlation yielding $\tau_{\text{final}} = (12 \pm 2)$ fs (rms) [20] and shows good agreement with the simulated pulse duration for our beam line (section 5.4 above). The measurement time for a streaking spectrogram is similar to the 8 minute time scale over which the jitter was measured (Fig 5.6 above) at 4.8 fs (rms). This measurement shows that, over the duration required for the measurement, the laser–microwave synchronisation is no longer a limiting factor for the achievable pulse duration of compressed electron pulses. In fact, even under the isochronic beam line conditions detailed in section 5.4, the jitter only broadens the phase-space limited pulse duration by a factor of $\sqrt{2}$. A single-electron UED scan, however, requires a significantly longer acquisition time for a complete 4D movie. Studies of the long term drift in the synchronisation as a result of temperature instability and laser repetition-rate drift are presented in the next chapter, along with a method for compensation of such drift resulting in a stability of 4.7 fs over many hours.

Chapter 6.

Long term stability

Despite the excellent stability of the microwave source from 2 mHz to the Nyquist frequency of 2.5 MHz, providing 12 fs electron pulses, the synchronisation was found to deteriorate on longer time scales (hours and above), which are required for UED experiments in the single-electron regime. This drift manifests through two main routes, namely the repetition rate drift of the Ti:sapphire oscillator and the temperature drift in the laboratory. Without active feedback, any drift arising in the components used for extraction of the microwave will directly effect the quality of the synchronisation. While the microwave frequency $f_{\text{microwave}}$ will always directly follow any drift in the laser repetition rate f_{rep}, the frequency-dependent phase response of the filter elements yields an indirect drift between the microwave phase inside the cavity and the laser. Temperature fluctuations lead to thermal expansion of components which can lead to a phase delay in the coaxial cabling [117] or shifts in filter resonance frequencies.

In the following chapter, the long-term drift resulting from these two factors have been analysed. With compensation of the drifts arising, a long term synchronisation of better than 5 fs is demonstrated [90].

6.1. Repetition rate induced synchronisation drift

As $f_{\text{microwave}}$ is a multiple of the repetition rate f_{rep}, the long-term repetition-rate drift $\triangle f_{\text{rep}}$, shown in Fig 6.1a, is reflected at $f_{\text{microwave}}$ with a magnitude

$$\triangle f_{\text{microwave}} = \frac{f_{\text{microwave}}}{f_{\text{rep}}} \triangle f_{\text{rep}}. \tag{6.1}$$

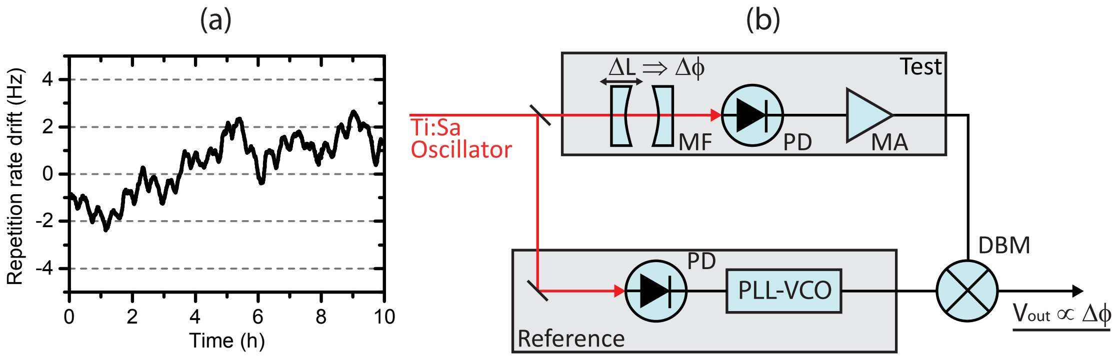

Figure 6.1.: (a) Repetition-rate drift of the Ti:sapphire oscillator. The ~1 Hz rms drift manifests as a much larger drift at GHz frequencies, data from [25]. (b) Filter phase response measurement technique. MF mode filter, PD photodiode, MA microwave amplifier, DBM Double balanced mixer. The filter element is placed in the test arm and supplied by an appropriate signal. The test signal is then mixed with a reference and the output yields the phase information as a DC voltage.

Consequently, the lower the repetition rate, the more severe the drift at $f_{\text{microwave}}$. This can become a problem when extracting GHz microwave signals from lasers with MHz repetition rates and below. Our 5 MHz repetition-rate Ti:sapphire oscillator exhibits a long-term repetition-rate drift $\triangle f_{\text{rep}} = 1\,\text{Hz}$ (rms). By Eq 6.1 this corresponds to $\triangle f_{\text{microwave}}$ drifting by approximately 1.2 kHz. In order to suppress the unwanted repetition-rate harmonics (i.e all the harmonics not at $f_{\text{microwave}}$), many microwave components were selected to have the highest quality factor and narrowest bandwidth. This has the trade off of rather sharp filter phase responses. A long term frequency instability of 10^{-6} (kHz drift in a GHz system) can already lead to fs-level drifts in the synchronisation via frequency-dependent phase shifts.

Measurement technique

Measurements of the phase response of the filter elements in the microwave generation scheme were performed to quantify the timing instabilities which arise as a result of long term drifts in the laser repetition rate. Figure 6.1b shows an example of the experimental setup for such a measurement, in this case for the optical-mode filter. The input frequency was deliberately scanned across the bandwidth of the filter. The signal output from the filter then contains the frequency-dependent phase response of the filter. In order to measure the phase, the signal was mixed in a double balanced mixer with a reference signal, containing the original unfiltered spectral components. The output of the mixer V_{out} is proportional to the product of the reference signal $A_1 \cos(2\pi f_{\text{microwave}} t)$ and the signal under test $A_2 \cos(2\pi f_{\text{microwave}} t + \triangle\phi)$, where $\triangle\phi$ is the phase difference upon traversing the filter. Note that the amplitudes A_1 and A_2 need to satisfy the appropriate input power specifications of the mixer. The output is then

$$\begin{aligned} V_{out} &\propto A_1 \cos(2\pi f_{\text{microwave}} t)\, A_2 \cos(2\pi f_{\text{microwave}} t + \triangle\phi) \\ &\propto \cos(\triangle\phi) + \cos(4\pi f_{\text{microwave}} t + \triangle\phi)\,. \end{aligned} \tag{6.2}$$

The output was low-pass filtered, leaving the DC element $\cos(\triangle\phi)$, dependent on the induced phase shift. For an accurate measure, calibration of the mixer was required. Note that Eq 6.2 only treats input signals of one spectral component. For inputs with multiple spectral components with output will be

$$V_{out} \propto \sum_{n=1}^{N} \cos(\triangle\phi_n)\,, \tag{6.3}$$

where N is the number of identical frequency components in the reference and test arms and $\triangle\phi_n$ are the phase differences of all such components. With no method to break down V_{out} and relate it to the individual $\triangle\phi_n$, it is important to provide a spectrally pure reference signal.

Phase measurements

The phase response of the first component in the microwave generation scheme, the optical mode filter (section 5.1), was measured with this setup (Fig 6.1b). Specifically, a portion of the Ti:sapphire oscillator was split into two beams and photodetected, one via the optical-mode filter. After photodetection, the test arm underwent amplification to achieve a signal strength required to drive the mixer in a linear fashion. As the photodetected pulse trains contain frequency components at all harmonics of the laser repetition rate, the reference arm was derived by using the second photodetected pulse train to drive a VCO, phase locked to $f_{\text{microwave}}$ with a PLL. To scan the resonance of the mode filter, the mirror distance was mechanically tuned (and hence the resonance frequency by Eq 5.2). The result of this is shown in Fig 6.2. The normalised transmission is shown in black and shows a resonance frequency of $f_{\text{microwave}} = 6.237\,\text{GHz}$, and a bandwidth of ~5 MHz. The

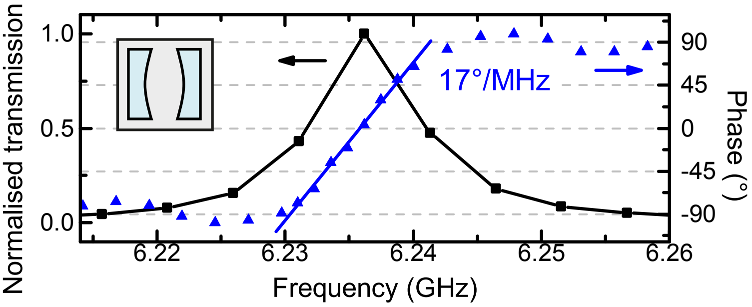

Figure 6.2.: Optical mode filter frequency response. The mode filter has a 3 dB bandwidth of ~9 MHz and a linear phase response. The phase slope amounts to 17 °/MHz around the resonance frequency.

measured phase response of the mode filter, in blue, in the region around the resonance frequency is linear with a slope of 24.1 °/MHz, amounting to a timing drift of 7.7 fs/kHz. With the long-term drifts resulting from the repetition-rate instability calculated at $\triangle f_{\mathrm{microwave}} = 1.2\,\mathrm{kHz}$, this results in a 9.2 fs (rms) drift arising as a result of the optical-mode filter, showing we can expect a long term drift in the synchronisation more than twice the magnitude of the drift which occurs on an 8 minute time scale (chapter 5), and this from just one component in the microwave generation scheme.

Measurements of the phase response of the microwave filters and microwave cavity were made under the same principle described above in Fig 6.1. The generation of the test and reference arms to drive the mixer was somewhat more straightforward in these cases. Here the output of an external microwave synthesiser was split and used to supply the component under test and as the reference. As the output power of the synthesiser (SMF100A, Rohde and Schwarz) can be selected from -20 to +20 dBm, no further amplification of either arms, for both the cavity and filters, was necessary. The microwave cavity is equipped with an antenna pickup to allow monitoring of the phase, and power, inside the cavity. The measurements across the bandwidth of the components were performed by sweeping the output frequency from the microwave synthesiser, with the results shown in Figs 6.3 and 6.4 for the filters and cavity, respectively. The colours in the figure represent the same as for Fig 6.2 (that is, transmission in black; phase response in blue). The microwave filters present a somewhat larger bandwidth than the optical-mode filter, however due to the high-order nature of the filters (note the steep roll off outside the passband), the filter has a 540° phase shift across its bandwidth. This amounts to a slope of 11 °/MHz, or 4.9 fs/kHz, showing the repetition-rate drift

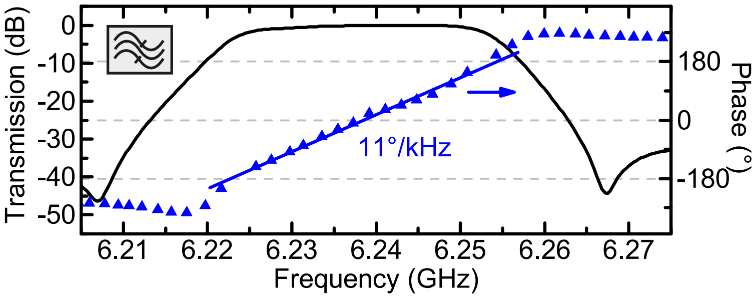

Figure 6.3.: Microwave filter frequency response. The filters have reasonably wide bandwidths, compared to the mode filter, of ~40 MHz, however they also posses an extreme roll off in transmission outside the bandwidth, reflecting their high order nature. The phase response over the filter bandwidth is approximately linear with a 540 ° phase shift and a slope of 11 °/MHz

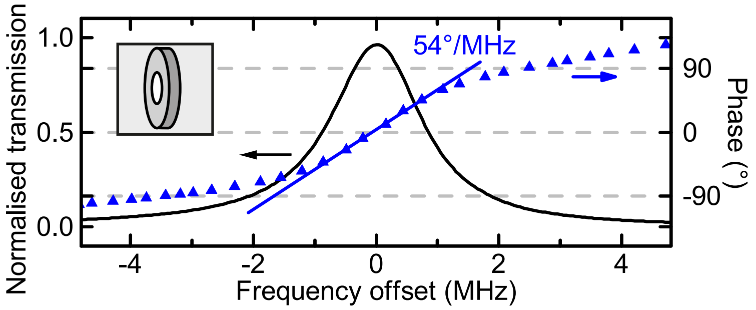

Figure 6.4.: Microwave cavity frequency response. The cavity presents a bandwidth of ~2 MHz, as per the design of maximum rejection of the neighbouring modes. The phase response over the bandwidth is linear with a slope of 54 °/MHz around the resonance frequency.

manifests a 5.8 fs (rms) drift in each of the two microwave filters. While less severe than the optical-mode filter, with two filters, this amounts to a total microwave filter induced drift of 11.6 fs (rms). The microwave cavity on the other hand has a much narrower bandwidth, as seen in Fig 6.4, of less than 2 MHz. Within the cavity bandwidth, the phase response amounts to 54 °/MHz (20 fs/kHz). Owing to this narrower bandwidth, the microwave cavity has the harshest phase response, yielding a drift of ~24 fs (rms) in response to the laser repetition rate drifts.

6.2. Temperature induced synchronisation drift

Before the laser is photodetected, temperature instabilities can cause a drift in the optical-mode filter. The mode filter resonance frequency, defined above in section 5.1, is directly related to optical-path length, and hence the mirror separation (Eq 5.2). Path-length instabilities lead to resonance-frequency instabilities due to thermal expansion of the steel mount. This can be used to estimate the required stability of the mirror separation to maintain few-femtosecond synchronisation. Consider a temperature change $\triangle T$ resulting in a change in the path length $\triangle L$, given by

$$\triangle L = \alpha L \triangle T, \tag{6.4}$$

where α is the linear coefficient of thermal expansion of the mode filter mount. This yields a resonance frequency of

$$f_{new} = \frac{c}{2\left(L + \triangle L\right)}, \tag{6.5}$$

or a shift in the resonance frequency of

$$\begin{aligned} \triangle f &= \frac{c}{2\left(L + \triangle L\right)} - \frac{c}{2L} = \frac{c}{2}\left(\frac{L - \left(L + \triangle L\right)}{L\left(L + \triangle L\right)}\right) \\ &= \frac{c}{2L}\left(\frac{\triangle L}{L + \triangle L}\right) \\ &\approx f\left(\frac{\triangle L}{L}\right), \end{aligned} \tag{6.6}$$

giving a temperature dependent resonance frequency shift

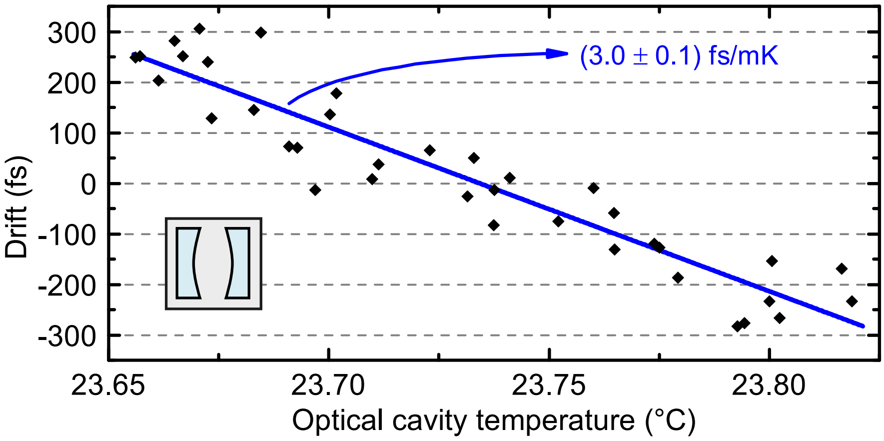

Figure 6.5.: Optical-mode filter temperature dependent phase drift. The slope presents a linear drift of 3.0 fs/mK. The point to point fluctuations arise from drift in other components in the generation scheme.

$$\frac{\triangle f}{\triangle T} \approx \alpha f. \tag{6.7}$$

In the case of our steel mounting block, where $\alpha = 12 \times 10^{-6}$, at a central frequency of $f = f_{\mathrm{micorwave}} = 6.237\,\mathrm{GHz}$, Eq 6.7 gives a magnitude of $\triangle f/\triangle T = 748\,\mathrm{kHz/K}$. Given that the phase response of the mode filter is approximately linear around the resonance frequency (see section 6.1 above) we can equate this to a temperature dependent timing drift of 5.7 fs/mK.

To verify this slope, a direct measurement of the effect of temperature fluctuations in the mode filter on the laser–microwave drift inside the microwave cavity was made. This measurement was possible by monitoring the central energy of the electron pulses with the ToF detector, described above in section 4.2. As this method requires a full power microwave source driving the cavity, it was not possible to entirely isolate the drift of the optical-mode filter. However, by controlled modulation of the mode-filter temperature, the drift resulting from the mode-filter could be distinguished, with the result shown in Fig 6.5. A clear linear drift is evident, and fitting reveals a slope of (3.0 ± 0.1) fs/mK. The point-to-point fluctuations of ~200 fs are believed to be a result of other components in the generation scheme. To reduce this temperature-induced drift, the mode filter was enclosed within an isolated housing, resulting in temperature fluctuations of 11 mK (rms), however this still amounts to a timing drift of (33 ± 1) fs (rms).

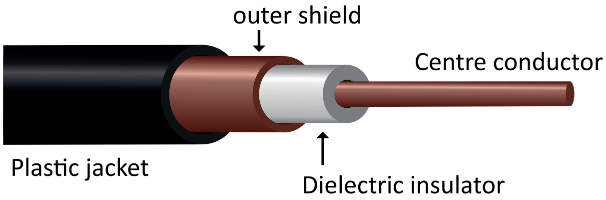

Figure 6.6.: A typical coaxial cable. The centre conductor and the outer shield are typically copper. They are separated by an insulating dielectric material, often polyethylene or polytetrafluoroethylene (PTFE), and surrounded by a plastic jacket. Cables consisting of a PTFE jacket can be remarkably temperature stable above 20 °C [117].

The next step in the microwave system that has the possibility to be effected by temperature is the coaxial cabling. A typical coaxial cable consists of a central copper conductor, and an outer grounded shield, insulated from each other by a dielectric and housed in a plastic jacket, see Fig. 6.6. An important measure of a coaxial cable is the electrical length L_e, defined as the number of wavelengths in the cable, and given by

$$L_e = \frac{f_{\text{microwave}} l \sqrt{\epsilon_r}}{c}, \tag{6.8}$$

where l is the cable length, ϵ_r is the relative permittivity of the dielectric and c the speed of light. In the case of a constant microwave frequency, the electrical length is dependent only on the physical length of the cable, and the velocity of propagation v_p inside the cable, where

$$v_p = \frac{c}{\sqrt{\epsilon_r}}. \tag{6.9}$$

Temperature instabilities in the cabling lead to thermal expansion of the central conductor and consequently the physical propagation distance, governed by the linear thermal expansion coefficient α of the conductor (for copper $\alpha = 16.6 \times 10^{-6}\text{m}/(\text{m}\cdot\text{K})$). Furthermore, temperature effects the relative permittivity of the dielectric [117], and therefore the propagation velocity. In order to evaluate the phase change due to temperature instabilities, both of these effects must be taken into account. Measurements on different commercial cables have been performed with interesting results [117]. These measurements showed that cables with the same insulator present drifts of varying magnitude, hence the phase dependence on temperature depends on numerous factors and is specific to particular cables. Of key importance however, is Polytetrafluoroethylene (PTFE), commonly known as

Teflon, a common dielectric found in coaxial cables. Teflon undergoes a molecular phase change around 20 °C [118] and causes a dramatic shift in the dielectric constant. When operating near to this temperature, cabling containing Teflon is very susceptible to temperature instabilities, however above this temperature, there exists cables where the change in the dielectric constant counteracts the expansion of the central conductor, yielding regions of superior stability. One such cable is the Phase Master 190 (Teledyne Storm Microwave) which presents an approximately constant phase stability of $\triangle\phi = 35\,\text{ppm}/^\circ\text{C}$ over the temperature range 20–40 °C. Note that calculating the timing drift arising from such an instability is possible by

$$\triangle t = \frac{L_e}{f_{\text{microwave}}} \triangle\phi. \tag{6.10}$$

For the Phase Master 190, this amounts to 140 fs/(m·K) (after normalising Eq 6.10 to one metre). This cable was installed everywhere in the experimental arrangement where any significant length (>0.1 m) of cable was required, yielding a total cable length of 2 m. All cables were insulated from the surroundings with an additional foam layer, reducing temperature fluctuations to <0.1 K (rms). With these stringent implementations, the temperature induced drift resulting from coaxial cabling still amounts to 28 fs (rms). Note that one of the cables presented in [117] has a phase stability an order of magnitude better than the Phase Master 190, however it also has a massive attenuation at 6 GHz, about 3 dB/m. This attenuation would lead to an increase in the high frequency jitter, as discussed in sections 5.1, and was considered an unfavourable trade off. Furthermore, bending in the cabling also leads to phase shifts and care was taken to ensure the cables were mounted rigidly everywhere.

The microwave amplifiers consist of active components which generate a considerable amount of heat. While typical amplifiers can maintain operation up to ~100 °C, any temperature dependent phase response could result in considerable degradation in the synchronisation if the amplifiers are left unstabilised. This was quantified by using the ToF detection method, and monitoring the amplifier temperature after power is initially applied. The result, in Fig 6.7, shows an 800 fs drift over less than 6 °C, or a linear temperature drift coefficient of (0.15 ± 0.01) fs/mK. Without temperature stabilisation, the amplifiers would need to be left to thermalise before the microwave could be used for electron compression. However, cooling the amplifiers removes the requirement of waiting until thermalisation (if cooled at room temperature) and also ensures safe operation. Therefore, the am-

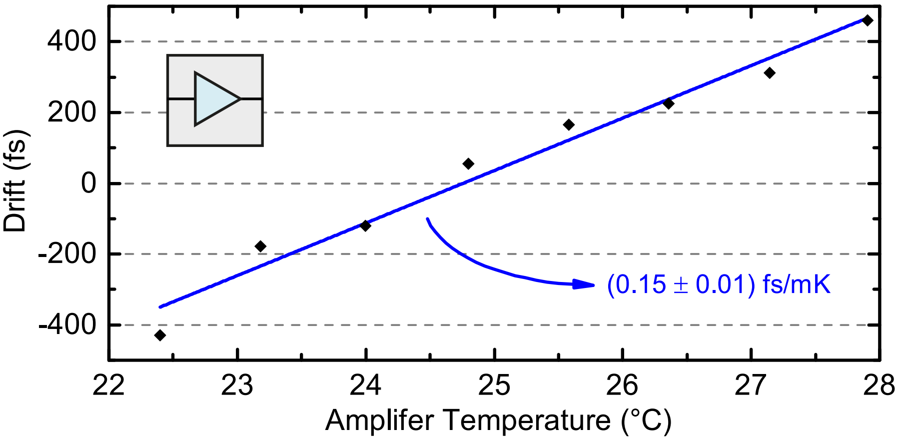

Figure 6.7.: Microwave amplifier temperature dependent phase drift. The slope presents a linear drift of 0.15 fs/mK. The measured data points present reduced noise compared with Fig 6.5 as the measurement time is greatly reduced, isolating the amplifier induced drift from other components.

plifier chain was cooled with a closed circuit at 25 °C, with a stability of 35 mK (rms), corresponding to a timing drift of (5.2 ± 0.3) fs (rms).

The last component requiring consideration with respect to temperature related effects was the microwave cavity itself. Here, the cavity is similar to the optical-mode filter in that thermal expansion results in a shift in the compression-cavity resonance frequency. This is in fact a necessity to enable optimum input coupling of the microwave source. With no other way to tune the resonance frequency, the cavity temperature must be tuned such that f_0 overlaps with $f_{\text{microwave}}$. This required active stabilisation of the cavity and with $f_0 = f_{\text{microwave}} = 6.237\,\text{GHz}$, necessitated a set temperature of 35 °C. Figure 6.8 shows the ToF-measured phase drift as a result of scanning the microwave cavity temperature. It presents a linear phase drift with a coefficient of (-1.10 ± 0.02) fs/mK. This implies a timing drift of (-38.5 ± 0.7) fs when the cavity is temperature stabilised at (35.0 ± 0.4) °C.

These results suggest the necessity of components being temperature stabilised to ~1 mK or better in order to achieve a few-femtosecond or below long-term drift in the synchronisation. This would require major planning and implementation however, with suitable laboratory conditions (isolated air conditioning system) and the best temperature stabilisation units, it could be possible. However, an alternative approach was devised and implemented here and is described below.

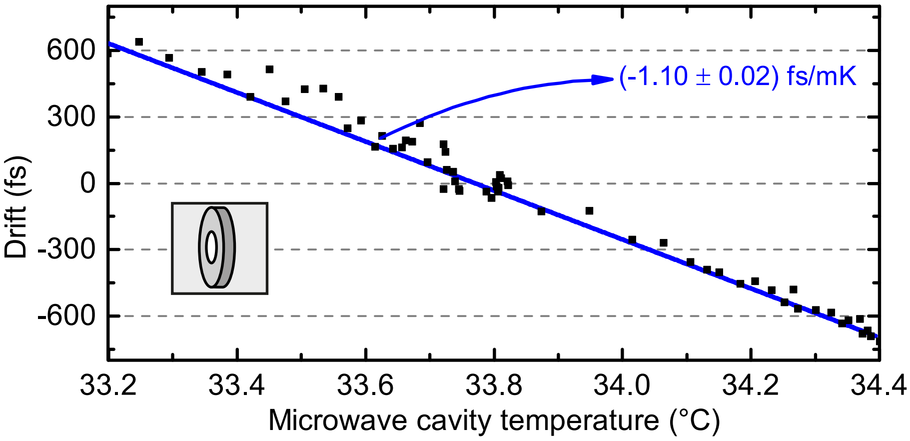

Figure 6.8.: Microwave cavity temperature dependent phase drift. The slope presents a linear drift of -1.1 fs/mK. Similar to Fig 6.7, a short measurement time isolates the amplifier induced drift.

6.3. Drift compensation

Precise temperature stabilisation of the critical components involved in microwave generation and electron compression on a 1 mK scale poses a major technical challenge. Here, to avoid the need for intricate temperature control, we present in-situ timing-drift compensation which is capable of removing timing drift from the measurement system via either a slow feedback loop or time stamping and post processing of the acquired data. The upper panel of Fig 6.9 shows typical long-term laser–microwave timing drift due to the combined effect of temperature fluctuations and repetition-rate drift, which we recorded with the ToF phase detector under similar conditions as described for the out-of-loop synchronisation measurements in chapters 4 and 5. A strong influence on the timing stability appears to be temperature oscillations with a period of about half an hour, caused by the laboratory air conditioning system, which induce laser–microwave timing drift of about 200 fs (peak-to-peak). Additionally, in order to verify the timing drift measured by the ToF phase detector, a cross-correlation between the laser pulses and the electron pulses passing through the compression cavity was recorded repeatedly every ~8 minutes via laser field streaking; as described above in section 5.5. This cross-correlation contains not only information about the electron pulse duration [112] (cross-correlation width) but also the time-zero between laser and electron pulse directly at the position of the diffraction sample, given by the temporal position of the cross-correlation signal. Any timing drift due to drift of the microwave phase

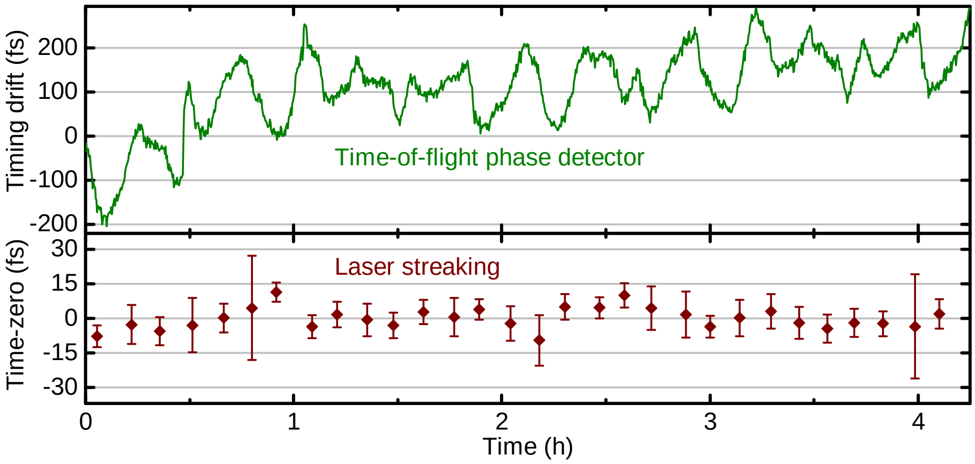

Figure 6.9.: Long term drift correction [90]. Above: the uncompensated drift between microwave phase and electron arrival inside the cavity, showing a peak-to-peak drift of >400 fs. The oscillations on a ~30 min timescale reflect the laboratory temperature fluctuations. Below: The drift after cross-correlated compensation, showing a peak-to-peak drift of less than 15 fs.

is revealed by the laser–electron cross-correlation, which is correlating the electron pulses after the interaction with the microwave inside the compression cavity again with the main clock of the experiment (that is, the laser pulses). Thus, the cross-correlation measurement qualifies as an out-of-loop verification of the timing drift measured by the ToF phase detector. Note that both the timing drift (phase detector) and the cross-correlation (streaking) are recorded by the same ToF energy analyser; hence, a shutter was positioned within the streaking laser beam path in order to interleave both measurements on a few-second time scale.

The ToF-measured timing drift shown in the upper panel of Fig 6.9 was then applied to correct the laser–electron delay of the corresponding streaking spectra over the entire measurement period. Each data point was therefore assigned a measured drift delay. This reduces the drift to the accuracy of the characterisation method, of a few-femtoseconds in this case (see section 4.2). The result, the evaluated time-zero from the corrected cross-correlation measurements, is depicted in the lower panel of Fig 6.9. After drift correction, the remaining time-zero fluctuations amount to 4.7 fs (rms) over a duration of more than 4 hours [90]. This is only limited by the error margins of the time-zero evaluation, suggesting an even better drift compensation. In conclusion, the in-situ time stamping method presented here is capable of reducing the long-term laser–microwave timing drift from hundreds of femtoseconds to below 5 fs (rms), eliminating the need for elaborate temperature control in the ~mK range and below, as required for an approach without drift compensation. Furthermore, this result is a factor of 6 better than the long-term drift achieved through time-stamping for other UED systems [30]. Implementation of this compensation technique, together with the synchronisation scheme present in chapter 5 and an optimised electron beam line, will allow the possibility for studying the fastest electronic and atomic dynamics.

Chapter 7.

Outlook

This work has demonstrated a technique for synchronisation of a few-GHz microwave with a 5 MHz Ti:sapphire laser oscillator with hitherto unprecedented few-femtosecond precision on both short term (chapter 5) and long term (chapter 6) time scales. Characterisation with the FLOM-PD (chapter 3) at high frequencies, together with ToF phase detection (chapter 4) at low frequencies has shown that by using direct extraction of the microwave from the Ti:sapphire oscillator (chapter 5), the jitter was suppressed to 4.8 fs from 2 mHz to 2.5 MHz, allowing for the compression of electrons down to 12 fs (rms) (chapter 5).

The feasibility of our compressed single-electron pulses for probing atomic-scale material dynamics has been demonstrated with static diffraction from an organic crystal [20] and pump–probe diffraction from graphite [119]. However, some further steps are necessary to perform time-resolved diffraction experiments with compressed electron pulses. The capability for simultaneous energy analysis with the ToF spectrometer (for drift compensation), and diffraction image capture with the camera, are as yet not available in the existing UED beamline. So far, interchanging between the two measurement systems requires a few minutes.

One concept for diffraction with online drift compensation is depicted in Fig 7.1. Drift measurement is implemented on the undiffracted electrons arriving at the center of the camera through a hole drilled in the centre of the camera. This allows these electrons (of minimal value for the diffraction image) to pass towards the ToF spectrometer and compensation of the drift is achieved through adjustment of the delay of the excitation pulses in real time. An alternative concept is the use of magnetic deflection coils to quickly exchange between the two measurement systems, effectively at the flick of a switch (μs–ms time scale). This would involve designing the beam line with the ToF spectrometer spatially offset from the camera, hence not requiring modification of the camera in any way.

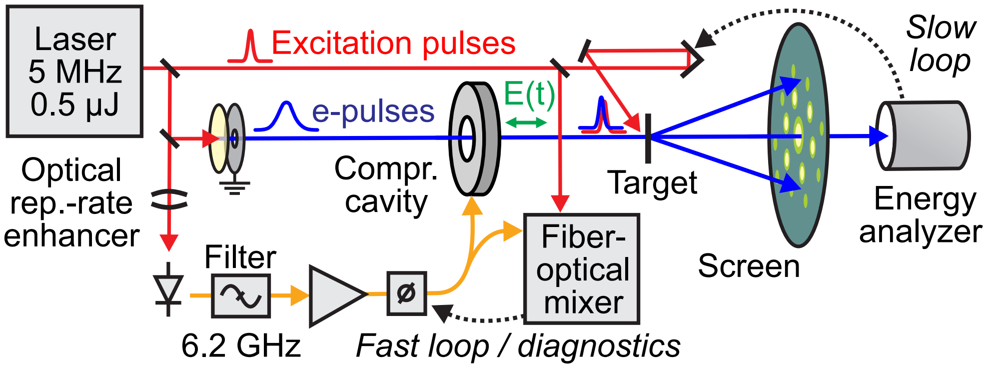

Figure 7.1.: Concept for electron diffraction measurement with laser–electron drift compensation [90]. The noticeable addition is the "slow loop". In this example, a hole is drilled in the centre of the camera used for diffraction image captures, allowing a portion of the undiffracted electrons to be used for drift measurement and subsequent compensation with the slow loop.

Implementation of one of these concepts will allow the probing of atomic scale light–driven matter transformations with few-femtosecond resolution in time and atomic resolution in space. Eventually, this may also allow the visualisation of pure charge-density motion induced by optical fields [120], the primary step of any light–matter interaction, demonstrating ultrafast electron diffraction's exciting prospects for the future.

Appendix A.

Laser streaking of compressed electron pulses

The setup for the streaking measurement is shown in Fig A.1. Central to this technique is the use of a free-standing 50 nm aluminum foil which acts as a mirror for the laser pulses while electrons are transmitted, albeit only with an efficiency of 3.5%. The foil is placed at the location of the diffraction sample to enable streaking of compressed electron pulses. Upon propagation through the Al foil, the 25 keV electrons experience an abrupt transition from a region of high field, to the field-free region behind the foil. This transition, approximately 84 as based on the 7.6 nm penetration depth of 800 nm light in aluminium [121], is much shorter than an optical cycle and allows a net transfer of energy to the electrons. Phase matching between the electrons and the laser is achieved through a noncollinear geometry with angles of incidence of 17° and 77° to the surface normal for the electron beam and the laser beam, respectively [122]. To maximise the electric field in the electron propagation direction, and hence the transfer of energy, the laser is polarised parallel to the plane of incidence. After the foil, the electron energy is measured with the ToF spectrometer (see section 4.2). Recording the electron energy as a function of the laser–electron delay yields a spectrogram containing a cross-correlation between the laser streaking pulse and the compressed electron pulse.

The carrier-envelope phase of the laser pulses used in this work was not stabilised and hence random for every laser shot. Therefore, the streaking spectrogram reflects the envelope of the streaking field. With an optical streaking pulse of wavelength λ and a peak electric field of E_{max}, the maximum energy transferred to the electrons, at a central energy U_0, due to a longitudinal interaction with the streaking field is given by [49, 122]:

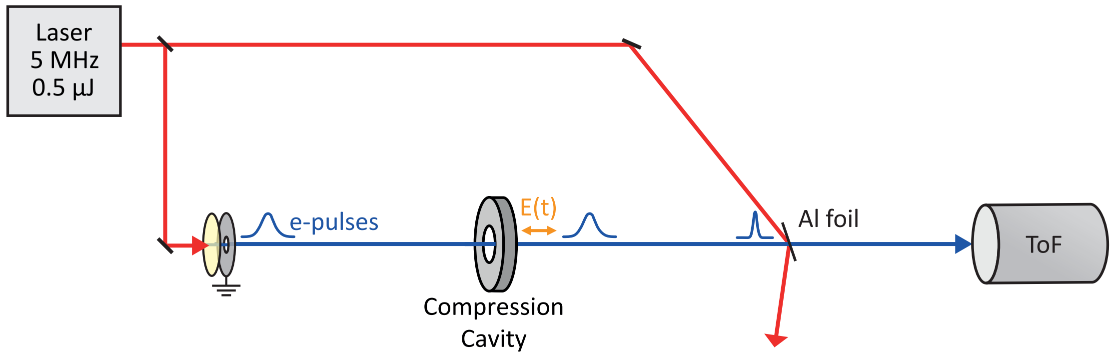

Figure A.1.: Setup for laser streaking of compressed electron pulses. A 50 nm free-standing aluminium foil is placed at the location of the diffraction sample, reflecting the incident laser pulses while transmitting the compressed electrons. Propagation through the foil from a high field into a low field allows a net transfer of energy to the electrons. This energy transfer is maximised by maintaining the polarisation of the laser parallel to the plane consisting of both electron and laser pulses. Phase matching is achieved through a noncollinear geometry. Recording the electron energies over a delay scan with the ToF spectrometer results in a spectrogram containing a cross-correlation of the laser pulses and the compressed electron pulses.

$$\triangle U_{max} = \frac{e\lambda}{\sqrt{2m_e}\pi c}\sqrt{U_0}E_{max}, \tag{A.1}$$

where e is the electronic charge and m_e is the electron mass. It should be noted that E_{max} is the amplitude resulting from the streaking field in the direction of electron propagation and is a superposition of both the incident and reflected beams. The beam diameter at the foil was 56 μm × 86 μm FWHM, projected onto the electron beam axis, and the maximum field amplitude was $E_{max} = 1.9\,\text{GV/m}$ [112]. From Eq A.1, this equates to a maximum energy gain of approximately$E_{max} = 77.4\,\text{eV}$, with electrons of energy $U_0 = 25\,\text{keV}$. In order to avoid thermal damage of the streaking foil, the repetition rate of the laser system is reduced to the 100 kHz range via a pulse picker. For a full description of the streaking experiment, see [20].

Appendix B.

High-resolution time-of-flight detector

The setup for the high-resolution ToF detector is shown in B.1. Electron pulses of multi-keV average energy travelling at non-relativistic speeds are incident on a micro-channel plate (MCP) detector (MCP 3636, Surface Concept GmbH) with single-shot capability. While not relativistic, the propagation speed is nevertheless high and electrons at a central energy of 25 keV, with less than a few eV energy bandwidth disperse by only about 200 fs/(eV·m), far below the MCP impulse response of ~200 ps. To achieve a suitable resolution, a drift tube is inserted into the electron beam path. This consists of a central copper conductor, charged to a few volts below the initial acceleration voltage, and a grounded aluminium casing [48]. Upon entry, the electrons experience deceleration and propagate through the tube with minimal velocity and the electrons of only slightly differing energies experience heavy temporal dispersion. At the exit of the tube, the electrons are accelerated back to their initial velocity and arrive at the MCP detector. The MCP, triggered by the laser pulses, maps the electron arrival time to its respective energy. Careful design of the physical dimensions of the drift tube is essential to minimise electrostatic lensing, and hence transverse divergence; a detailed description of the design process can be found in [20]. The drift tube construction of length 200 mm and radius 20 mm, allows an MCP resolution of better than 1 eV (FWHM) over a range of ~10 eV, designed for 25 keV of central energy, for realistic electron beam parameters (1 mm radius, 2.4 mrad divergence).

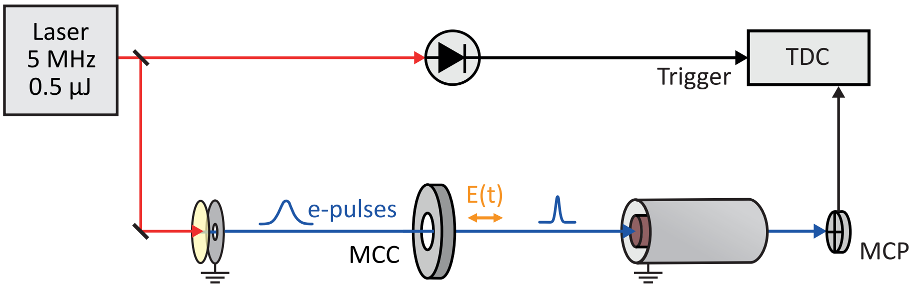

Figure B.1.: Time-of-flight spectrometer concept. Electron pulses of multi-keV average energy, in this case 25 keV, travelling at ~0.3c are incident on a micro-channel plate (MCP) detector. Electrons with slightly higher energy arrive earlier than those of lower energy, however at 25 keV, this difference is well below the resolution of the MCP impulse response of ~200 ps. To increase the resolution, a drift tube is inserted into the electron beam path. This consists of a central copper conductor, charged to a few volts below the initial acceleration voltage, and a grounded aluminium casing [48]. Upon entry, the electrons experience deceleration and propagate through the tube with minimal velocity and the electrons of only slightly differing energies experience heavy temporal dispersion. At the exit, the electrons are accelerated back to their initial velocity and arrive at the MCP detector. The MCP, triggered by the laser pulses, maps the electron arrival time to its respective energy.

Bibliography

[1] A. H. Zewail. Femtochemistry: Atomic-scale dynamics of the chemical bond using ultrafast lasers - (Nobel lecture). *Angewandte Chemie-international Edition*, 39(15):2587–2631, 2000.

[2] W. E. King, G. H. Campbell, A. Frank, B. Reed, J. F. Schmerge, B. J. Siwick, B. C. Stuart, and P. M. Weber. Ultrafast electron microscopy in materials science, biology, and chemistry. *Journal of Applied Physics*, 97(11):111101, June 2005.

[3] D. Shorokhov and A. H. Zewail. 4D electron imaging: principles and perspectives. *Physical Chemistry Chemical Physics*, 10(20):2879–2893, 2008.

[4] M. Chergui and A. H. Zewail. Electron and x-ray methods of ultrafast structural dynamics: Advances and applications. *Chemphyschem*, 10(1):28–43, January 2009.

[5] A. H. Zewail. Four-dimensional electron microscopy. *Science*, 328(5975):187–193, April 2010.

[6] R. J. D. Miller. Femtosecond crystallography with ultrabright electrons and x-rays: Capturing chemistry in action. *Science*, 343(6175):1108–1116, 2014.

[7] R. Srinivasan, V. A. Lobastov, C. Y. Ruan, and A. H. Zewail. Ultrafast electron diffraction (UED) - a new development for the 4D determination of transient molecular structures. *Helvetica Chimica Acta*, 86(6):1763–1838, 2003.

[8] A. H. Zewail. 4D ultrafast electron diffraction, crystallography, and microscopy. *Annual Review of Physical Chemistry*, 57:65–103, 2006.

[9] B. J. Siwick, J. R. Dwyer, R. E. Jordan, and R. J. D. Miller. An atomic-level view of melting using femtosecond electron diffraction. *Science*, 302(5649):1382–1385, November 2003.

[10] R. Ernstorfer, M. Harb, C. T. Hebeisen, G. Sciaini, T. Dartigalongue, and R. J. D. Miller. The formation of warm dense matter: Experimental evidence for electronic bond hardening in gold. *Science*, 323(5917):1033–1037, February 2009.

[11] G. Sciaini, M. Harb, S. G. Kruglik, T. Payer, C. T. Hebeisen, F. J. M. Zu Heringdorf, M. Yamaguchi, M. H. Hoegen, R. Ernstorfer, and R. J. D. Miller. Electronic acceleration of atomic motions and disordering in bismuth. *Nature*, 458(7234):56–U2, March 2009.

[12] P. Zhou, C. Streubuhr, M. Ligges, T. Brazda, T. Payer, F. M. Z. Heringdorf, M. Horn-von Hoegen, and D. von der Linde. Transient anisotropy in the electron diffraction of femtosecond laser-excited bismuth. *New Journal of Physics*, 14:103031, October 2012.

[13] P. Baum, D. S. Yang, and A. H. Zewail. 4D visualization of transitional structures in phase transformations by electron diffraction. *Science*, 318(5851):788–792, November 2007.

[14] M. Eichberger, H. Schafer, M. Krumova, M. Beyer, J. Demsar, H. Berger, G. Moriena, G. Sciaini, and R. J. D. Miller. Snapshots of cooperative atomic motions in the optical suppression of charge density waves. *Nature*, 468(7325):799–802, December 2010.

[15] S. Wall, B. Krenzer, S. Wippermann, S. Sanna, F. Klasing, A. Hanisch-Blicharski, M. Kammler, W. G. Schmidt, and M. Horn-von Hoegen. Atomistic picture of charge density wave formation at surfaces. *Physical Review Letters*, 109(18):186101, November 2012.

[16] H. Liu, O. H. Kwon, J. Tang, and A. H. Zewail. 4D imaging and diffraction dynamics of single-particle phase transition in heterogeneous ensembles. *Nano Letters*, 14(2):946–954, 2014.

[17] H. Ihee, V. A. Lobastov, U. M. Gomez, B. M. Goodson, R. Srinivasan, C. Y. Ruan, and A. H. Zewail. Direct imaging of transient molecular structures with ultrafast diffraction. *Science*, 291(5503):458–462, January 2001.

[18] R. Srinivasan, J. S. Feenstra, S. T. Park, S. J. Xu, and A. H. Zewail. Dark structures in molecular radiationless transitions determined by ultrafast diffraction. *Science*, 307(5709):558–563, January 2005.

[19] M. Gao, C. Lu, H. Jean-Ruel, L. C. Liu, A. Marx, K. Onda, S. Y. Koshihara, Y. Nakano, X. Shao, T. Hiramatsu, G. Saito, H. Yamochi, R. R. Cooney, G. Moriena, G. Sciaini, and R. J. D. Miller. Mapping molecular motions leading to charge delocalization with ultrabright electrons. *Nature*, 496(7445):343–346, April 2013.

[20] A. Gliserin. *Towards attosecond 4D imaging of atomic-scale dynamics by single-electron diffraction.* PhD thesis, Ludwig-Maximilians Universität München, 2014.

[21] P. Baum. On the physics of ultrashort single-electron pulses for time-resolved microscopy and diffraction. *Chemical Physics*, 423:55–61, September 2013.

[22] E. Fill, L. Veisz, A. Apolonski, and F. Krausz. Sub-fs electron pulses for ultrafast electron diffraction. *New Journal of Physics*, 8:272, November 2006.

[23] L. Veisz, G. Kurkin, K. Chernov, V. Tarnetsky, A. Apolonski, F. Krausz, and E. Fill. Hybrid DC-AC electron gun for fs-electron pulse generation. *New Journal of Physics*, 9:451, December 2007.

[24] T. van Oudheusden, P. L. E. M. Pasmans, S. B. van der Geer, M. J. de Loos, M. J. van der Wiel, and O. J. Luiten. Compression of subrelativistic space-charge-dominated electron bunches for single-shot femtosecond electron diffraction. *Physical Review Letters*, 105(26):264801, December 2010.

[25] A. Gliserin, A. Apolonski, F. Krausz, and P. Baum. Compression of single-electron pulses with a microwave cavity. *New Journal of Physics*, 14:073055, July 2012.

[26] M. Gao, H. Jean-Ruel, R. R. Cooney, J. Stampe, M. de Jong, M. Harb, G. Sciaini, G. Moriena, and R. J. D. Miller. Full characterization of RF compressed femtosecond electron pulses using ponderomotive scattering. *Optics Express*, 20(11):12048–12058, May 2012.

[27] G. F. Mancini, B. Mansart, S. Pagano, B. van der Geer, M. de Loos, and F. Carbone. Design and implementation of a flexible beamline for fs electron diffraction experiments. *Nuclear Instruments & Methods In Physics Research Section A-accelerators Spectrometers Detectors and Associated Equipment*, 691:113–122, November 2012.

[28] R. P. Chatelain, V. R. Morrison, C. Godbout, and B. J. Siwick. Ultrafast electron diffraction with radio-frequency compressed electron pulses. *Applied Physics Letters*, 101(8):081901, August 2012.

[29] G. J. H. Brussaard, A. Lassise, P. L. E. M. Pasmans, P. H. A. Mutsaers, M. J. van der Wiel, and O. J. Luiten. Direct measurement of synchronization between femtosecond laser pulses and a 3 GHz radio frequency electric field inside a resonant cavity. *Applied Physics Letters*, 103(14):141105, September 2013.

[30] M. Gao, Y. Jiang, G. H. Kassier, and R. J. D. Miller. Single shot time stamping of ultrabright radio frequency compressed electron pulses. *Applied Physics Letters*, 103(3):033503, July 2013.

[31] J. C. Ashley, C. J. Tung, and R. H. Ritchie. Electron inelastic mean free paths and energy-losses in solids: I. Aluminum metal. *Surface Science*, 81(2):409–426, 1979.

[32] D. Kreier and P. Baum. Avoiding temporal distortions in tilted pulses. *Optics Letters*, 37(12):2373–2375, June 2012.

[33] B. J. Siwick, J. R. Dwyer, R. E. Jordan, and R. J. D. Miller. Ultrafast electron optics: Propagation dynamics of femtosecond electron packets. *Journal of Applied Physics*, 92(3):1643–1648, August 2002.

[34] S. B. van der Geer, M. J. de Loos, E. J. D. Vredenbregt, and O. J. Luiten. Ultracold electron source for single-shot, ultrafast electron diffraction. *Microscopy and Microanalysis*, 15(4):282–289, August 2009.

[35] P. Baum. Towards ultimate temporal and spatial resolutions with ultrafast single-electron diffraction. *Journal of Physics B-atomic Molecular and Optical Physics*, 47(12):124005, June 2014.

[36] S. Tokita, S. Inoue, S. Masuno, M. Hashida, and S. Sakabe. Single-shot ultrafast electron diffraction with a laser-accelerated sub-MeV electron pulse. *Applied Physics Letters*, 95(11):111911, September 2009.

[37] P. Musumeci, J. T. Moody, C. M. Scoby, M. S. Gutierrez, and M. Westfall. Laser-induced melting of a single crystal gold sample by time-resolved ultrafast relativistic electron diffraction. *Applied Physics Letters*, 97(6):063502, August 2010.

[38] Y. Murooka, N. Naruse, S. Sakakihara, M. Ishimaru, J. Yang, and K. Tanimura. Transmission-electron diffraction by MeV electron pulses. *Applied Physics Letters*, 98(25):251903, June 2011.

[39] V. A. Lobastov, R. Srinivasan, and A. H. Zewail. Four-dimensional ultrafast electron microscopy. *Proceedings of the National Academy of Sciences of the United States of America*, 102(20):7069–7073, May 2005.

[40] S. Lahme, C. Kealhofer, F. Krausz, and P. Baum. Femtosecond single-electron diffraction. *Structural Dynamics*, 1(3):034303, 2014.

[41] M. Aidelsburger, F. O. Kirchner, F. Krausz, and P. Baum. Single-electron pulses for ultrafast diffraction. *Proceedings of the National Academy of Sciences of the United States of America*, 107(46):19714–19719, November 2010.

[42] T. van Oudheusden, E. F. de Jong, S. B. van der Geer, W. P. E. M. Op 't Root, O. J. Luiten, and B. J. Siwick. Electron source concept for single-shot sub-100 fs electron diffraction in the 100 keV range. *Journal of Applied Physics*, 102(9):093501, November 2007.

[43] F. O. Kirchner, S. Lahme, F. Krausz, and P. Baum. Coherence of femtosecond single electrons exceeds biomolecular dimensions. *New Journal of Physics*, 15(6):063021, 2013.

[44] W. E. Spicer. Optical transitions in which crystal momentum is not conserved. *Physical Review Letters*, 11(6):243–&, 1963.

[45] L. Kasmi, D. Kreier, M. Bradler, E. Riedle, and P. Baum. Femtosecond single-electron pulses generated by two-photon photoemission close to the work function. *New Journal of Physics*, 17(3):033008, 2015.

[46] X. R. Jiang, C. N. Berglund, A. E. Bell, and W. A. Mackie. Photoemission from gold thin films for application in multiphotocathode arrays for electron beam lithography. *Journal of Vacuum Science & Technology B*, 16(6):3374–3379, November 1998.

[47] J. Kim, F. X. Kärtner, and F. Ludwig. Balanced optical-microwave phase detectors for optoelectronic phase-locked loops. *Optics Letters*, 31(24):3659–3661, December 2006.

[48] A. Gliserin, M. Walbran, and P Baum. A high-resolution time-of-flight spectrometer for sub-relativistic electron pulses. in submission, 2015.

[49] F. O. Kirchner, A. Gliserin, F. Krausz, and P. Baum. Laser streaking of free electrons at 25 keV. *Nat Photon*, 8(1):52–57, January 2014.

[50] G. H. Kassier, K. Haupt, N. Erasmus, E. G. Rohwer, and H. Schwoerer. Achromatic reflectron compressor design for bright pulses in femtosecond electron diffraction. *Journal of Applied Physics*, 105(11):113111, June 2009.

[51] Y. Wang and N. Gedik. Electron pulse compression with a practical reflectron design for ultrafast electron diffraction. *IEEE Journal of Selected Topics In Quantum Electronics*, 18(1):140–147, January 2012.

[52] P. Baum and A. H. Zewail. Attosecond electron pulses for 4D diffraction and microscopy. *Proceedings of the National Academy of Sciences of the United States of America*, 104(47):18409–18414, November 2007.

[53] S. A. Hilbert, C. Uiterwaal, B. Barwick, H. Batelaan, and A. H. Zewail. Temporal lenses for attosecond and femtosecond electron pulses. *Proceedings of the National Academy of Sciences of the United States of America*, 106(26):10558–10563, June 2009.

[54] L. J. Wong, B. Freelon, T. Rohwer, N. Gedik, and S. G. Johnson. All-optical three-dimensional electron pulse compression. *New Journal of Physics*, 17(1):013051, 2015.

[55] C. Weninger and P. Baum. Temporal distortions in magnetic lenses. *Ultramicroscopy*, 113:145–151, February 2012.

[56] IEEE standard definitions of physical quantities for fundamental frequency and time metrology - random instabilities. *IEEE Std 1139-1999*, 1999.

[57] I. Zamek and S. Zamek. Definitions of jitter measurement terms and relationships. In *Test Conference, 2005. Proceedings. ITC 2005. IEEE International*, pages 10 pp.–34, 2005.

[58] R. B. Neal. *The Stanford Two-mile Accelerator*. W. A. Benjamin, 1968.

[59] C. J. Bocchetta, D. Bulfone, F. Cargnello, M. Danailov, G. D'Auria, B. Diviacco, M. Ferianis, A. Gambitta, E. Karantzoulis, G. Loda, M. Lonza,

F. Mazzolini, D. Morelli, G. Pangon, V. Smaluk, M. Stefanutti, M. Svandrlik, L. Tosi, G. Tromba, A. Vascotto, R. Visintini, R. Bakker, W. A. Barletta, W. M. Fawley, R. Bonifacio, S. G. Biedron, M. D. Borland, S. V. Milton, S. De Silvestri, R. P. Walker, J. H. Wu, and L. H. Yu. Overview of FERMI@ELETTRA: a proposed ultra-bright coherent X-ray source in Italy. *Nuclear Instruments & Methods In Physics Research Section A-accelerators Spectrometers Detectors and Associated Equipment*, 507(1-2):484–488, July 2003.

[60] M. Altarelli. The European X-ray free-electron laser facility in Hamburg. *Nuclear Instruments & Methods In Physics Research Section B-beam Interactions With Materials and Atoms*, 269(24), December 2011.

[61] F. B. Kiewiet, A. H. Kemper, O. J. Luiten, G. J. H. Brussaard, and M. J. van der Wiel. Femtosecond synchronization of a 3 GHz RF oscillator to a mode-locked Ti:sapphire laser. *Nuclear Instruments & Methods In Physics Research Section A-accelerators Spectrometers Detectors and Associated Equipment*, 484(1-3):619–624, May 2002.

[62] J. F. Cliche and B. Shillue. Precision timing control for radioastronomy - maintaining femtosecond synchronization in the atacama large millimeter array. *IEEE Control Systems Magazine*, 26(1):19–26, February 2006.

[63] P. Ghelfi, F. Laghezza, F. Scotti, G. Serafino, A. Capria, S. Pinna, D. Onori, C. Porzi, M. Scaffardi, A. Malacarne, V. Vercesi, E. Lazzeri, F. Berizzi, and A. Bogoni. A fully photonics-based coherent radar system. *Nature*, 507(7492):341–345, March 2014.

[64] S. A. Diddams, T. Udem, J. C. Bergquist, E. A. Curtis, R. E. Drullinger, L. Hollberg, W. M. Itano, W. D. Lee, C. W. Oates, K. R. Vogel, and D. J. Wineland. An optical clock based on a single trapped $^{199}\mathrm{Hg}^{+}$ ion. *Science*, 293(5531):825–828, August 2001.

[65] T. M. Fortier, M. S. Kirchner, F. Quinlan, J. Taylor, J. C. Bergquist, T. Rosenband, N. Lemke, A. Ludlow, Y. Jiang, C. W. Oates, and S. A. Diddams. Generation of ultrastable microwaves via optical frequency division. *Nature Photonics*, 5(7):425–429, July 2011.

[66] W. Zhang, Z. Xu, M. Lours, R. Boudot, Y. Kersale, G. Santarelli, and Y. Le Coq. Sub-100 attoseconds stability optics-to-microwave synchronization. *Applied Physics Letters*, 96(21):211105, May 2010.

[67] J. Taylor, S. Datta, A. Hati, C. Nelson, F. Quinlan, A. Joshi, and S. Diddams. Characterization of power-to-phase conversion in high-speed p-i-n photodiodes. *Photonics Journal, IEEE*, 3(1):140–151, 2011.

[68] J. Kim, J. A. Cox, J. Chen, and F. X. Kärtner. Drift-free femtosecond timing synchronization of remote optical and microwave sources. *Nature Photonics*, 2(12):733–736, December 2008.

[69] G. Marra, R. Slavik, H. S. Margolis, S. N. Lea, P. Petropoulos, D. J. Richardson, and P. Gill. High-resolution microwave frequency transfer over an 86-km-long optical fiber network using a mode-locked laser. *Optics Letters*, 36(4):511–513, February 2011.

[70] B. Wang, C. Gao, W. L. Chen, J. Miao, X. Zhu, Y. Bai, J. W. Zhang, Y. Y. Feng, T. C. Li, and L. J. Wang. Precise and continuous time and frequency synchronisation at the 5×10^{-19} accuracy level. *Scientific Reports*, 2:556, August 2012.

[71] J. Kim. *High-Precision Optical and Microwave Signal Synthesis and Distribution.* PhD thesis, Massachusetts Institute of Technology, 2007.

[72] K. Jung, J. Shin, J. Kang, S. Hunziker, CK. Min, and J. Kim. Frequency comb-based microwave transfer over fiber with 7×10^{-19} instability using fiber-loop optical-microwave phase detectors. *Optics Letters*, 39(6):1577–1580, March 2014.

[73] M. Xin, K. Safak, M. Y. Peng, P. T. Callahan, and F. X. Kärtner. One-femtosecond, long-term stable remote laser synchronization over a 3.5-km fiber link. *Optics Express*, 22(12):14904–14912, June 2014.

[74] X. Chen, J. Zhang, J. Lu, X. Lu, X. Tian, B. Liu, H. Wu, T. Tang, K. Shi, and Z. Zhang. Feed-forward digital phase compensation for long-distance precise frequency dissemination via fiber network. *Opt. Lett.*, 40(3):371–374, 2015.

[75] W. Schottky. Regarding spontaneous current fluctuation in different electricity conductors. *Annalen Der Physik*, 57(23):541–567, December 1918.

[76] J. B. Johnson. Thermal agitation of electricity in conductors. *Physical Review*, 32(1):97–109, July 1928.

[77] H. Nyquist. Thermal agitation of electric charge in conductors. *Physical Review*, 32(1):110–113, July 1928.

[78] R. W. Boyd. *Radiometry and the Detection of Optical Radiation.* Wiley, 1983.

[79] A. Haboucha, W. Zhang, T. Li, M. Lours, A. N. Luiten, Y. Le Coq, and G. Santarelli. Optical-fiber pulse rate multiplier for ultralow phase-noise signal generation. *Optics Letters*, 36(18):3654–3656, September 2011.

[80] J. Kim and F. X. Kärtner. Microwave signal extraction from femtosecond mode-locked lasers with attosecond relative timing drift. *Optics Letters*, 35(12):2022–2024, June 2010.

[81] M. Y. Peng, A. Kalaydzhyan, and F. X. Kärtner. Balanced optical-microwave phase detector for sub-femtosecond optical–RF synchronization. *Opt. Express*, 22(22):27102–27111, 2014.

[82] Y. L. Huang and C. K. Sun. Nonlinear saturation behaviors of high-speed p-i-n photodetectors. *Journal of Lightwave Technology*, 18(2):203–212, February 2000.

[83] A. Bartels, S. A. Diddams, C. W. Oates, G. Wilpers, J. C. Bergquist, W. H. Oskay, and L. Hollberg. Femtosecond-laser-based synthesis of ultrastable microwave signals from optical frequency references. *Optics Letters*, 30(6):667–669, March 2005.

[84] J. Capmany and D. Novak. Microwave photonics combines two worlds. *Nature Photonics*, 1(6):319–330, June 2007.

[85] K. Jung and J. Kim. Subfemtosecond synchronization of microwave oscillators with mode-locked Er-fiber lasers. *Optics Letters*, 37(14):2958–2960, July 2012.

[86] G. P. Agrawal. *Nonlinear Fiber Optics.* Academic Press, 2006.

[87] N. J. Doran and D. Wood. Nonlinear-optical loop mirror. *Optics Letters*, 13(1):56–58, January 1988.

[88] R. P. Scott, T. D. Mulder, K. A. Baker, and B. H. Kolner. Amplitude and phase noise sensitivity of modelocked Ti:sapphire lasers in terms of a complex noise transfer function. *Optics Express*, 15(14):9090–9095, July 2007.

[89] M. Lessing, H. S. Margolis, C. T. A. Brown, P. Gill, and G. Marra. Suppression of amplitude-to-phase noise conversion in balanced optical-microwave phase detectors. *Optics Express*, 21(22):27057–27062, November 2013.

[90] M. Walbran, A. Gliserin, K. Jung, J. Kim, and P Baum. 5-fs laser-electron synchronization for pump-probe crystallography and diffraction. in submission, 2015.

[91] A. Gliserin, M. Walbran, and P. Baum. Passive optical enhancement of laser-microwave synchronization. *Applied Physics Letters*, 103(3):031113, July 2013.

[92] R. Sabella and S. Merli. Analysis of InGaAs p-i-n photodiode frequency response. *Quantum Electronics, IEEE Journal of*, 29(3):906–916, 1993.

[93] N. Li, X. W. Li, S. Demiguel, X. G. Zheng, J. C. Campbell, D. A. Tulchinsky, K. J. Williams, T. D. Isshiki, G. S. Kinsey, and R. Sudharsansan. High-saturation-current charge-compensated InGaAs-InP uni-traveling-carrier photodiode. *IEEE Photonics Technology Letters*, 16(3):864–866, March 2004.

[94] F. Quinlan, T. M. Fortier, H. Jiang, A. Hati, C. Nelson, Y. Fu, J. C. Campbell, and Diddams S. A. Exploiting shot noise correlations in the photodetection of ultrashort optical pulse trains. *Nat Photon*, 7(4):290–293, April 2013.

[95] K. J. Williams, R. D. Esman, and M. Dagenais. Effects of high space-charge fields on the response of microwave photodetectors. *Photonics Technology Letters, IEEE*, 6(5):639–641, May 1994.

[96] S. A. Diddams, M. Kirchner, T. Fortier, D. Braje, A. M. Weiner, and L. Hollberg. Improved signal-to-noise ratio of 10 GHz microwave signals generated with a mode-filtered femtosecond laser frequency comb. *Opt. Express*, 17(5):3331–3340, Mar 2009.

[97] D. Kuhl, F. Hieronymi, E. H. Bottcher, T. Wolf, D. Bimberg, J. Kuhl, and M. Klingenstein. Influence of space charges on the impulse-response

of InGaAs metal-semiconductor-metal photodetectors. *Journal of Lightwave Technology*, 10(6):753–759, June 1992.

[98] T. Ishibashi, T. Furuta, H. Fushimi, S. Kodama, H. Ito, T. Nagatsuma, N. Shimizu, and Y. Miyamoto. InP/InGaAs uni-traveling-carrier photodiodes. *IEEE Transactions On Electronics*, E83C(6):938–949, June 2000.

[99] Z. Li, H. Pan, H. Chen, A. Beling, and J. C. Campbell. High-saturation-current modified uni-traveling-carrier photodiode with cliff layer. *Quantum Electronics, IEEE Journal of*, 46(5):626–632, 2010.

[100] Z. Li, Y. Fu, M. Piels, H. Pan, A. Beling, J. E. Bowers, and J. C. Campbell. High-power high-linearity flip-chip bonded modified uni-traveling carrier photodiode. *Optics Express*, 19(26):385–390, December 2011.

[101] J. Chen, J. W. Sickler, P. Fendel, E. P. Ippen, F. X. Kärtner, T. Wilken, R. Holzwarth, and T. W. Hänsch. Generation of low-timing-jitter femtosecond pulse trains with 2 GHz repetition rate via external repetition rate multiplication. *Opt. Lett.*, 33(9):959–961, 2008.

[102] H. Jiang, J. Taylor, F. Quinlan, T. Fortier, and S.A. Diddams. Noise floor reduction of an Er:fiber laser-based photonic microwave generator. *Photonics Journal, IEEE*, 3(6):1004–1012, 2011.

[103] M. Y. Sander, S. Frolov, J. Shmulovich, E. P. Ippen, and F. X. Kärtner. 10 GHz femtosecond pulse interleaver in planar waveguide technology. *Optics Express*, 20(4):4102–4113, February 2012.

[104] D. A. Tulchinsky and K. J. Williams. Excess amplitude and excess phase noise of RF photodiodes operated in compression. *Photonics Technology Letters, IEEE*, 17(3):654–656, March 2005.

[105] W. Zhang, T. Li, M. Lours, S. Seidelin, G. Santarelli, and Y. Le Coq. Amplitude to phase conversion of InGaAs pin photo-diodes for femtosecond lasers microwave signal generation. *Applied Physics B-lasers and Optics*, 106(2):301–308, February 2012.

[106] W. Zhang, S. Seidelin, A. Joshi, S. Datta, G. Santarelli, and Y. Le Coq. Dual photo-detector system for low phase noise microwave generation with femtosecond lasers. *Optics Letters*, 39(5):1204–1207, March 2014.

[107] H. T. Friis. Noise figures of radio receivers. *Proceedings of the IRE*, 32(7):419–422, 1944.

[108] H. Wallman, A. B. Macnee, and C. P. Gadsden. A low-noise amplifier. *Proceedings of the Institute of Radio Engineers*, 36(6):700–708, 1948.

[109] K. Jung, J. Shin, and J. Kim. Ultralow phase noise microwave generation from mode-locked Er-fiber lasers with subfemtosecond integrated timing jitter. *Photonics Journal, IEEE*, 5(3):5500906–5500906, June 2013.

[110] http://www.pulsar.nl/gpt/.

[111] M. Hentschel, R. Kienberger, C. Spielmann, G. A. Reider, N. Milosevic, T. Brabec, P. Corkum, U. Heinzmann, M. Drescher, and F. Krausz. Attosecond metrology. *Nature*, 414(6863):509–513, November 2001.

[112] A. Gliserin, M. Walbran, F. Krausz, and P. Baum. 28-fs electron pulses for atomic-scale diffraction. in submission, 2015.

[113] M. Drescher, M. Hentschel, R. Kienberger, G. Tempea, C. Spielmann, G. A. Reider, P. B. Corkum, and F. Krausz. X-ray pulses approaching the attosecond frontier. *Science*, 291(5510):1923–1927, March 2001.

[114] R. Kienberger, M. Hentschel, M. Uiberacker, C. Spielmann, M. Kitzler, A. Scrinzi, M. Wieland, T. Westerwalbesloh, U. Kleineberg, U. Heinzmann, M. Drescher, and F. Krausz. Steering attosecond electron wave packets with light. *Science*, 297(5584):1144–1148, August 2002.

[115] M. Drescher, M. Hentschel, R. Kienberger, M. Uiberacker, V. Yakovlev, A. Scrinzi, T. Westerwalbesloh, U. Kleineberg, U. Heinzmann, and F. Krausz. Time-resolved atomic inner-shell spectroscopy. *Nature*, 419(6909):803–807, October 2002.

[116] R. Kienberger, E. Goulielmakis, M. Uiberacker, A. Baltuska, V. Yakovlev, F. Bammer, A. Scrinzi, T. Westerwalbesloh, U. Kleineberg, U. Heinzmann, M. Drescher, and F. Krausz. Atomic transient recorder. *Nature*, 427(6977):817–821, February 2004.

[117] K. Czuba and D. Sikora. Temperature stability of coaxial cables. *Acta Phsyica Polonica A*, 119:553–557, 2011.

[118] R. K. Kirby. Thermal expansion of polytetrafluoroethylene (Teflon) from −190° to +300° C. *Journal of Research of the National Bureau of Standards*, 57(2):91–94, 1956.

[119] S. Lahme. *Femtosecond single-electron diffraction*. PhD thesis, Ludwig Maximilians Universität, 2014.

[120] P. Baum and A. H. Zewail. 4D attosecond imaging with free electrons: Diffraction methods and potential applications. *Chemical Physics*, 366(1-3):2–8, December 2009.

[121] A. D. Rakic. Algorithm for the determination of intrinsic optical-constants of metal-films - application to aluminum. *Applied Optics*, 34(22):4755–4767, August 1995.

[122] F. O. Kirchner. *Ultrashort and coherent single-electron pulses for diffraction at ultimate resolutions*. PhD thesis, Ludwig-Maximilians Universität, 2013.

Data archiving

The experimental raw data, evaluation files, and original figures can be found on the Data Archive Server of the Laboratory for Attosecond Physics at the Max Planck Institute of Quantum Optics: `/afs/rzg/mpq/lap/publication_archive`.

The source data of all figures is organised relative to the root folder of the data archive for the thesis within subfolders inside the `/figures` directory, using the same figure numbers as in the thesis. A text file within each folder named `fig_X.X.txt` (`X.X` being the figure number) gives detailed information about the organisation and format of the raw data, as well as the processing performed in order to obtain the final figure. Further experimental and simulation details are given where applicable, in addition to the main text.

List of publications

Publications in refereed journals

A. Gliserin, **M. Walbran**, F. Krausz and P. Baum. *28-fs electron pulses for atomic-scale diffraction.* Accepted, Nature Communications (2015).

M. Walbran, A. Gliserin, K. Jung, J. Kim and P. Baum. *5-fs laser-electron synchronization for pump–probe crystallography and diffraction.* Accepted, Physical Review Applied (2015)

A. Gliserin, **M. Walbran** and P. Baum. *A high-resolution time-of-flight spectrometer for sub-relativistic electron pulses.* In preparation (2015).

A. Gliserin, **M. Walbran** and P. Baum. *Passive optical enhancement of laser-microwave synchronization.* Applied Physics Letters 103, 031113 (2013).

Proceedings of refereed conferences

A. Gliserin, S. Lame, **M.Walbran**, F. Krausz and P. Baum. *Ultrafast Single-Electron Diffraction.* In Ultrafast Phenomena XIX. Vol. 162, 295{298 (2015).

A. Gliserin, F. O. Kirchner, **M. Walbran**, F. Krausz and P. Baum. *Laser Streaking of Free-Electron Pulses at 25 keV.* In Ultrafast Phenomena XIX. Vol. 162, 291{294 (2015).

P. Metha, **M. Walbran,** J. K. Jang and S. G. Murdoch. *An all-fiber source for multiplex coherent anti-Stokes Raman scattering.* In Conference On Lasers and Electro-optics (2010).

Acknowledgements

Firstly, my thanks go to Prof. Ferenc Krausz for providing me with the opportunity to take up my PhD studies in his renowned group. It was certainly an experience to work in such a resourceful team where people are always happy to help. I would like to thank Prof. Jom Luiten for agreeing to review my thesis. Thanks to Peter Baum for his motivation and providing ideas to move the research forward. When times got difficult he always maintained a positive attitude and looked to help in any way possible. He also provided me with valuable feedback for improving my thesis at top speed when I was under a lot of pressure to finish writing.

I owe a big thank you to Alex Gliserin. Upon first arriving here, his direction meant I was always busy and felt like a big head start. It was great to always have someone to ask with seemingly endless patience, coming only at the cost of ever so slightly patronising teachings. The döners are coming! Luckily, Jungwon Kim saw potential in our group and chose to spend his sabbatical here. I am sure his knowledge and experience shortened my PhD by a few times the length of time he spent here. Also, thanks to Kwangyun Jung for taking the time to visit; I took a lot away in the two days he spent with our group. Mr Öhm and the rest of the workshop put up with my laughable attempts at German. On only two occasions do I remember Mr Öhm ordering me to “get Gliserin” because things got too difficult — all the other times we were able to come to an agreement on any problem.

Thanks also to the rest of the UED group for providing a great working environment. I can’t imagine looking after my own child better than the care with which Stefan Lahme and Friedrich Kirchner showed our laser. When the laser became my responsibility I definitely realised the effort required to keep it operating nicely! The rest of the second floor were always willing to lend equipment, bring cake on a seemingly endless supply of birthdays, and wind down at the end of the week with a beer. The floor also organised a great birthday present after my office mate Andrey took my ignoring of his question about bungy jumping as a “sure, bungy jumping has long been my greatest desire”. While I didn’t look pleased at all upon receiving the gift (I wasn’t), I was happy enough afterwards to try again!

The start and the end — thanks to Amy for encouraging me to take up this challenge. Without her advice, I would not have even thought about leaving NZ. Thanks to Kyle for proofreading my thesis like a champ on somewhat short notice. After three and a half years here it definitely seems like my English has degraded far more than my German has improved. If nothing else, I can now say I know where to use my en dashes. Also, Henning came to my rescue when I was trying to write my Zussamenfassung. It was a much better idea to write it over a beer with a native speaker.

It was great to have Jennie and Bonesaw living in Garching for two years. These two were slightly under appreciated at times but it made a huge difference to have family close by, which I didn't really realise until they had left. I'm also grateful to have gotten to know the two musketeers Kellie and Lena, who were always ready for action. Very rarely have I had a dull moment in the last few years and it was good to have a touch of almost home and a seemingly infinite source of energy.

Lastly, I would like to thank my parents. They eventually realised the futility in asking when I'll be moving back home, but they never stopped calling at random times just to say hi. They decided to expand their business in 2012 and since then have become even busier than before (when it should be going the other way!) but it didn't stop them coming over to visit me, even when I told them not to. I saw straight through their poor excuse of "We'll be in Europe anyway for our 40th wedding anniversary". Thank you both for making me feel loved and for liking me better than you like my brothers.